

Effect of Heat Current on Magnetization Dynamics in Magnetic Insulators and Nanostructures

THÈSE N° 6657 (2015)

PRÉSENTÉE LE 17 JUILLET 2015

À LA FACULTÉ DES SCIENCES DE BASE
LABORATOIRE DE PHYSIQUE DES MATÉRIAUX NANOSTRUCTURÉS
PROGRAMME DOCTORAL EN PHYSIQUE

ÉCOLE POLYTECHNIQUE FÉDÉRALE DE LAUSANNE

POUR L'OBTENTION DU GRADE DE DOCTEUR ÈS SCIENCES

PAR

Francesco Antonio VETRÒ

acceptée sur proposition du jury:

Prof. V. Savona, président du jury
Prof. J.-Ph. Ansermet, directeur de thèse
Prof. J. Dubowik, rapporteur
Prof. H. Yu, rapporteur
Dr G. Boero, rapporteur



ÉCOLE POLYTECHNIQUE
FÉDÉRALE DE LAUSANNE

Suisse
2015

"Experience is what you get when you didn't get what you wanted.
And experience is often the most valuable thing you have to offer"
— Randy Pausch, *The Last Lecture*

To my mother, my sister and my brother...

Acknowledgements

There are many people I am very grateful to for their support during my PhD. It is especially thanks to them that I will remember these years at EPFL as a wonderful and memorable period of my life.

First of all, I would like to express my gratitude to my thesis advisor Jean-Philippe Ansermet for giving me the opportunity to join his group and for the guidance he has provided me during my PhD. He supported me constantly with passion and enthusiasm. I really enjoyed when, visiting the lab, he would help in setting up new experiments. I will never forget those moments. Thank you!

I would also like to acknowledge Dr. Giovanni Boero, Prof. Haiming Yu and Prof. Janusz Dubowik for having accepted to be part of my exam committee and Prof. Vincenzo Savona for having presided it. Their comments and feedback were very precious for the improvement of this thesis. Thanks in particular to Haiming for the interesting experiments carried out together, and for the stimulating discussions at the cafeteria during coffee time.

I am very grateful to my colleagues Alex, Christian, Murari and Yoon for creating both a stimulating and pleasant working environment. Thanks also to Sylvain for his precious help on theoretical aspects, and Lucas for the great job on nanowires. My gratitude goes also to the other and former members of the group Pedro, Mohamed, He Li, Daljit, Janeki, Nicolas and Varun. It was a pleasure to meet all of them.

A special thanks goes to my former colleagues and great friends Elisa, Francesco and Arndt. The time we spent together was incredibly amazing. Thanks for your support and help during the most difficult and happy moments. This time here would have not been the same without you. Grazie di tutto! Vielen Dank!

I would also like to extend my gratitude to all other members of the ICMP institute I had the opportunity to meet. Particular thanks goes to Wolfgang, Andreas and my special Chinese friend Chongqi: it was a pleasure working with you during the teaching duties.

I am very thankful to all the members of the technical staff for their invaluable help, in particular to Gilles, José, Philippe, Claude, Michel, Primo and Martial, and to the secretaries of the

Acknowledgements

institute Florence, Nadja and Chantal for their endless patience and kindness. Merci beaucoup.

Un grazie di cuore agli amici di casa *Les Amis* Lucian, Diego e Matteo con i quali ho iniziato questa splendida esperienza, e grazie anche a Pietro che si è aggiunto successivamente. Nessuno quanto voi ha condiviso con me gioie e dolori di questi anni. Lo stesso vale anche per Giovanna, Sergio, Ombretta, Mariana, Bea, e nonostante la lontananza, anche Mario ed Ale. Grazie per essere stati sempre presenti nei momenti importanti e per avermi fatto sentire come se avessi una seconda famiglia. Non dimenticherò mai lo storico compleanno al lago. Grazie anche a tutti coloro i quali non ho citato qui di seguito, ma con cui ho passato momenti veramente indimenticabili.

Vorrei ringraziare calorosamente mia sorella Gessica e mio fratello Giuseppe. Con il vostro affetto ed il vostro amore avete eliminato i 1500 km di distanza che ci separano. Grazie soprattutto a te Mamma. Se oggi sono arrivato fin qui, è anche merito tuo. Tu, che solo con il tuo esempio hai saputo darmi la forza nei momenti di maggior sconforto e sei stata fonte di ispirazione per le scelte più importanti della mia vita.

La mia più grande gratitudine va a infine a te Patrizia, per il tuo supporto, fondamentale durante la stesura della tesi, per la tua pazienza, la tua comprensione, il tuo affetto, e soprattutto per aver condiviso con me i momenti più belli e più importanti di questi ultimi anni.

Lausanne, 03 July 2015

F. Antonio Vetrò

Abstract

The term "spin caloritronics" defines a novel branch of spintronics that focuses on the interplay between electron spins with heat currents. In the frame of this research area, this thesis is aimed at investigating the effect of a heat current on magnetization dynamics in two different typologies of systems and materials: magnetic insulators and metallic nanostructures.

In the first case we conduct studies on yttrium iron garnet (YIG) samples subjected to a temperature gradient. The irreversible thermodynamics of a continuous medium with magnetic dipoles predicts that a thermal gradient across a YIG slab, in the presence of magnetization waves, produces a magnetic field that is the magnetic analog of the well known Seebeck effect. This thermally induced field can influence the time evolution of the magnetization, in such a way that it is possible to modulate the relaxation of the precession when applying a heat current. We found evidence for such a magnetic Seebeck effect (MSE) by conducting transmission measurements in a thin slab of YIG subjected to an in-plane temperature gradient. We showed how the MSE can modulate the magnetic damping depending on the direction of the propagating magnetostatic modes with respect to the orientation of the temperature gradient.

In the second part of the thesis we focus our investigation on metallic nanostructures subjected to a heat current. In a metal, the three-current model (current of entropy, of spin up and spin down electrons) predicts that a heat current induces a spin current which will then influence the magnetization dynamics like a charge-driven spin current would. Hence, we explore what has been called Thermal Spin Torque in electrodeposited Co / Cu / Co asymmetric spin valves placed in the middle of copper nanowires. These samples are fabricated by conventional electrodeposition technique in porous polycarbonate membranes using an original method that allows high frequency electrical measurements. We used a modulated laser to investigate the effect of a temperature gradient. We observed a heat-driven spin torque by measuring electrically the quasi-static magnetic response of a spin valve when subjected to the heat current, generated by two laser diodes heating the electrical contact at one end or the other of the nanowire. Analyzing the variation in the resistance induced by a heat-driven spin torque, represented by peaks occurring in correspondence with the GMR transition, we found that a temperature difference of the order of 5 K is sufficient to produce sizeable torque in spin valves.

Keywords: spintronics, spin caloritronics, ferromagnetic resonance, thermal spin transfer torque, thermomagnetism, YIG, nanowires, spin valve.

Résumé

Le terme "spin caloritronique" définit un nouveau domaine de la spintronique qui étudie les interactions entre les spins des électrons et des courants de chaleur. Dans le cadre de ce domaine de recherche, cette thèse vise à étudier l'effet d'un courant de chaleur sur la dynamique de l'aimantation pour deux différents types de systèmes et de matériaux : des isolants magnétiques et des nanostructures métalliques. Dans le premier cas, nous menons des études sur des échantillons de grenat d'yttrium de fer (YIG) soumis à un gradient de température. La thermodynamique irréversible des milieux continus avec dipôles magnétiques prédit qu'un gradient thermique à travers une plaque de YIG, en présence d'ondes de magnétisation, produit un champ magnétique qui est l'analogie magnétique de l'effet Seebeck bien connu. Ce champ thermiquement induit peut influencer l'évolution temporelle de l'aimantation de telle sorte qu'il est possible de moduler la relaxation de la précession quand un courant de chaleur est appliqué. Nous avons prouvé l'existence d'un effet Seebeck magnétique (MSE) en effectuant des mesures de transmissions sur un échantillon de YIG soumis à un gradient de température parallèle à son plan. Nous avons montré comment le MSE peut moduler l'amortissement magnétique en fonction de la direction relative des modes magnétostatiques par rapport à l'orientation du gradient de température. Dans la deuxième partie de la thèse, nous menons nos recherches sur des nanostructures métalliques soumises à un courant de chaleur. Dans un métal, le modèle des trois courants (i.e entropie, spin up et spin down) prédit qu'un courant de chaleur induit un courant de spin qui peut à son tour influencer la dynamique d'aimantation de même façon qu'un courant électrique le ferait. Par conséquent, nous explorons ce qui a été appelé moment de force de spin thermique dans des vanes de spin asymétriques constituées de Co / Cu / Co et placées au milieu de nanofils de cuivre. Ces échantillons sont fabriqués avec la technique d'électrodéposition dans des membranes de polycarbonate poreux en utilisant une méthode originale qui permet des mesures électriques à haute fréquence. Nous avons utilisé un laser modulé pour étudier l'effet d'un gradient de température. Nous avons observé un moment de force de spin thermique en mesurant électriquement la réponse magnétique quasi-statique d'une vanne de spin, soumise à un courant de chaleur, produit par deux diodes laser chauffant le contact électrique d'une extrémité ou de l'autre du nanofil. En analysant la variation de la résistance induite par un moment de force de spin thermique, représentée par des pics correspondant à des transitions de GMR, nous avons trouvé que la différence de température de l'ordre de 5 K est suffisante pour produire dans la vanne de spin un moment de force non négligeable.

Acknowledgements

Mots clefs : spintronique, spin caloritronique, résonance ferromagnétique, moment de force de spin thermique, thermomagnétisme, YIG, nanofils .

Contents

Acknowledgements	i
Abstract (English/Français)	iii
List of figures	ix
1 Introduction	1
1.1 Spin Caloritronics	2
1.1.1 Charge and spin-dependent thermoelectric effects	2
1.1.2 The spin Seebeck effect	3
1.1.3 Effect of heat current on magnon dynamics	6
1.1.4 Yttrium Iron Garnet and magnon spintronics	9
1.2 Theory of spin waves and ferromagnetic resonance	10
1.2.1 Spin precession and equation of motion	10
1.2.2 Uniform excitation	11
1.2.3 Non-uniform excitation and spin waves	14
1.3 Thesis organization	17
2 Experimental setups and techniques	19
2.1 Continuous wave ferromagnetic resonance	19
2.2 Time resolved and pulsed technique	21
2.2.1 Temperature gradient generation and imaging	23
3 The magnetic Seebeck effect	27
3.1 Thermodynamic formalism for a magnetic insulator subjected to a thermal gradient	27
3.1.1 Linear response of the magnetization to a small excitation	29
3.1.2 Theoretical prediction	30
3.2 Experimental setup	31
3.3 Experimental results and discussion	32
3.4 Conclusion	37
4 Magnetization dynamics of ferromagnetic insulators subjected to a temperature gradient	39
4.1 YIG disks subjected to a temperature gradient	39

Contents

4.1.1	Resonant cavity experiment	39
4.1.2	WR-90 resonator	40
4.2	Thermally induced self-oscillation	43
4.3	Conclusions	44
5	Spin Dynamics in Magnetic Nanostructures	45
5.1	Spin-dependent transport and dynamics	45
5.1.1	Giant Magneto Resistance	45
5.1.2	Spin Transfer Torque	47
5.1.3	Thermal spin-transfer torque	50
5.2	Samples preparation, fabrication and characterization	50
5.2.1	Electrochemical growth of metallic nanowires	52
5.2.2	Electrical contact and characterization	53
5.3	Experimental setup for current induced STT-FMR	54
5.3.1	Temperature gradient	55
5.3.2	Laser modulated STT-FMR	57
5.4	Experimental results	57
5.4.1	Peak shape	60
5.4.2	Dispersion diagram and interpretation of dynamical modes	60
5.4.3	Effects of laser heating on STT-FMR	61
5.5	Conclusions	63
6	Linear Response to a heat-driven Spin Torque	67
6.1	Experimental methods	67
6.1.1	Sample fabrication	67
6.1.2	Measurement setup	68
6.2	Results and discussion	70
6.3	Conclusions	73
7	Summary and conclusions	75
	Bibliography	77
	List of abbreviations	84
	Curriculum Vitae	87

List of Figures

1.1	Typical diagram of a thermocouple circuit.	3
1.2	Schematic illustration of the spin-dependent thermoelectric phenomena. . . .	4
1.3	Schematic illustration of the spin Seebeck effect.	5
1.4	Brillouin light scattering measurements of propagating dipolar spin waves in presence of a temperature gradient.	7
1.5	Local FMR spectra of a single crystal YIG sample subjected to a temperature gradient $\nabla T \parallel \mathbf{H}$	8
1.6	Time resolved measurements of a YIG slab and a YIG/Pt structure subjected to a temperature gradient.	9
1.7	Illustration of the magnetization precession in a static magnetic field.	11
1.8	Real and immagirary parts of the magnetic susceptibility χ	13
1.9	Schematic illustration of one dimensional chain of spins.	14
1.10	Typology of magnetostatic spin wave modes as a function of the direction of the internal effective field \mathbf{H}_0	15
2.1	Schematics of the experimental setup for lock-in FMR detection with field modulation technique.	20
2.2	FMR spectrum of a single crystal YIG slab measured with field modulation technique.	21
2.3	Schematics of the experimental setup fot time resolved measurements.	22
2.4	Time resolved measurement of a single crystal slab of YIG.	23
2.5	Illustrations of the setups for the temperature gradient generation.	24
2.6	Infrared image example of single crystal slab of YIG subjected to a temperature gradient.	24
3.1	Illustration of the theoretical prediction for the magnetic Seebeck effect.	31
3.2	Time-resolved transmission measurements setup.	33
3.3	Time-resolved transmitted signal for a slab of YIG subjected to a temperature gradient.	34
3.4	Transmitted signal as a function of time, averaged over the applied magnetic field.	36
3.5	FMR spectra of a 15 ns pulsed excitation detected after 70 ns.	36
4.1	FMR spectra of a normally magnetized 120 μm thick disk of YIG as a function of the magnetic field.	40

List of Figures

4.2	FMR spectra of a normally magnetized 130 μm thick disk of YIG as a function of the magnetic field.	41
4.3	Electromagnetic simulations of the WR-90 waveguide resonator.	42
4.4	FMR spectra of a normally magnetized 500 μm thick disk of YIG as a function of the magnetic field.	44
5.1	Illustration of the Giant Magnetoresistance effect.	46
5.2	Illustration of the spin transfer torque effect.	48
5.3	Nanowires fabrication process.	51
5.4	Typical deposition curve of a single Co 30nm / Cu 10nm / Co 10nm asymmetric spin valve embedded in Cu nanowire.	53
5.5	Illustration details of the sample contacting method.	54
5.6	Giant magneto resistance of a Cu nanowire containing a Co 30nm / Cu 10nm / Co 10nm asymmetric spin valve.	55
5.7	STT-FMR experimental setup with field and laser modulation	56
5.8	STT-FMR spectra of single Co 5 nm / Cu 7 nm / Co 25 nm asymmetric spin valve for $H_{ext} < H_{SW}$	58
5.9	STT-FMR spectra of single Co 5 nm / Cu 7 nm / Co 25 nm asymmetric spin valve for $H_{ext} > H_{SW}$	59
5.10	Field dependence of the modes in the FMR spectra.	61
5.11	Dispersion diagrams of magnetic nanostructures.	62
5.12	Comparison of STT-FMR spectra masured with field and laser modulation techniques.	64
6.1	Sample preparation procedure for quasi-static electrical measurements.	68
6.2	Sample holder with double laser heating system.	69
6.3	GMR and heat induced lockin voltage of a Co/Cu/Co spin valve.	71
6.4	Data and simulation of the GMR and heat induced lockin voltage of a Co/Cu/Co spin valve.	71

1 Introduction

The discovery of the Spin Transfer Torque (STT) effect, theoretically predicted in 1996 by Slonczewski [1] and Berger [2], represented a milestone for Spintronics as it paved the way for several potential applications in the field of current-driven microwave oscillators and of data storage technologies. It was in particular in the latter that the STT implementation is most promising, allowing the development of a novel fast and high-density magnetic random access memory. However, the high densities of current and voltages required for such devices, cause heating effects that can influence thermal stability and can complicate the modeling. Nowadays an interest for heat management at nanoscale is continuously growing not only for the need to solve thermal stability problems, but also because controlling heating can be exploited for other purposes. For instance, thermally assisted reversal of magnetization via laser pulses and Joule heating of high resistive layers have been proposed as recording methods in magnetic memories.

The term “Spin Caloritronics” has been recently introduced to define a new emerging research field that combines spin-related phenomena with thermoelectric effects [3, 4]. The first studies that include charge, spin and heat transport were carried out by Johnson and Silsbee on metallic heterostructures [5]. This field has been recently invigorated by the discovery of the spin Seebeck effect [6], and in particular by the possibility to observe the presence of a spin current at distances that are orders of magnitude larger than the spin diffusion length [7].

The aim of this introductory chapter is to provide the basic theoretical background essential for a full understanding of this thesis. In the first section we introduce the spin caloritronics field reporting the fundamental concepts and presenting the most significant developments carried out in the recent years. The second part addresses instead the theory of ferromagnetic resonance and spin waves dynamics. Finally, we conclude giving information about the organization of this thesis.

1.1 Spin Caloritronics

In this section we provide a brief introduction to the field of spin caloritronics addressing the state-of-the-art and the most relevant contributions on this topic. Starting with the spin-dependent thermoelectric phenomena, we deal with the spin Seebeck effect and we report the recent developments on the effects of heat current on the spin waves relaxation. Apart from the thermal spin transfer torque that will be introduced in Chapter 5, we omit other phenomena related to this field as they are not relevant for this thesis. Nevertheless a more extensive and detailed review on spin caloritronics can be found in references [4, 8].

1.1.1 Charge and spin-dependent thermoelectric effects

A temperature gradient applied to an electrical conductor is known, from basic of solid state physics, to induce an internal electric field [9, 10]. A very simple explanation of this phenomenon is given by the difference of thermal energy between the charges at the hot and the cold end. The carriers, diffusing towards the cold side, generate an electric field that compensates the effect of the temperature gradient. In a steady state with no charge current ($\mathbf{J} = 0$), the electric field is expressed as $\mathbf{E} = -\nabla V = S\nabla T$, where S is the Seebeck coefficient (known also as thermopower), and ∇T the temperature gradient. According to the Mott relation [11], the Seebeck coefficient can be expressed as a function of the energy derivative of the conductivity, i.e.

$$S = -\frac{\pi^2 k_B^2 T}{3e} \frac{\partial}{\partial E} \ln \sigma \Big|_{E_F} = -\frac{\pi^2 k_B^2 T}{3e} \frac{\sigma'}{\sigma} \ln \sigma \Big|_{E_F}, \quad (1.1)$$

where E_F is the Fermi energy, and k_B the Boltzmann constant. This effect is well exploited to carry out temperature measurement by using the junction of two metals with different Seebeck coefficient $S_A \neq S_B$. This system is known as *thermocouple* and the circuit diagram is reported in Figure 1.1. When the metal junction is at temperature $T_1 \neq T_0$, with T_0 being the reference temperature, the voltage across the two metals is given by

$$V = -\int_{T_0}^{T_1} (S_A - S_B) dT. \quad (1.2)$$

The relation between charge (\mathbf{j}) and heat (\mathbf{q}) current densities with the respective driving forces, electric field and temperature gradient, can be expressed as:

$$\begin{pmatrix} \mathbf{j} \\ \mathbf{q} \end{pmatrix} = -\begin{pmatrix} \sigma & \sigma S \\ \sigma \Pi & \kappa \end{pmatrix} \begin{pmatrix} \nabla V \\ \nabla T \end{pmatrix} \quad (1.3)$$

where σ and κ are the electrical and thermal conductivity respectively. S and Π are the Seebeck and Peltier coefficients and they are linked by the Thomson-Osanger relation $\Pi = ST$ [12].

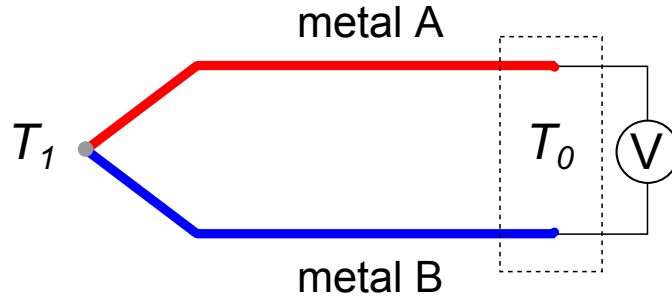


Figure 1.1: Typical diagram of a thermocouple circuit. A Seebeck voltage is generated by the difference between the temperature at the metal junction T_1 and the reference T_0 .

The spin-polarized electron transport can be described in terms of the two channel model with an electric current density $\mathbf{j} = \mathbf{j}^\uparrow + \mathbf{j}^\downarrow$, and a spin current density $\mathbf{j}_S = \mathbf{j}^\uparrow - \mathbf{j}^\downarrow$. In the same manner, we have an effective electric conductivity $\sigma = \sigma^\uparrow + \sigma^\downarrow$, and a spin-dependent polarization conductivity $\sigma_S = \sigma^\uparrow - \sigma^\downarrow$. In a metallic ferromagnet with a spin population imbalance at the Fermi energy, the thermoelectric relation of Equation (1.3) can be generalized to a thermodynamic three-current model. This has been described by Brechet and Ansermet in ref. [13], and is expressed as:

$$\begin{pmatrix} \mathbf{q} \\ \mathbf{j} \\ \mathbf{j}_S \end{pmatrix} = - \begin{pmatrix} \kappa T & \sigma S T & \sigma_S S_S T \\ \sigma S T & \sigma & \sigma_S \\ \sigma_S S_S T & \sigma_S & \sigma \end{pmatrix} \begin{pmatrix} \nabla T / T \\ \nabla V \\ \frac{1}{e} \nabla(\Delta\mu) \end{pmatrix}, \quad (1.4)$$

where $S = \frac{\sigma^\uparrow S^\uparrow + \sigma^\downarrow S^\downarrow}{\sigma^\uparrow + \sigma^\downarrow}$ is the Seebeck coefficient and $S_S = \frac{\sigma^\uparrow S^\uparrow - \sigma^\downarrow S^\downarrow}{\sigma^\uparrow - \sigma^\downarrow}$ the spin polarization Seebeck coefficient, whereas the term $\Delta\mu$ indicates the spin accumulation, namely the difference in the chemical potential between the spin-up and spin-down charge carriers. In addition to the Seebeck and Peltier effects, this model defines two other spin-dependent phenomena: the *spin-dependent Seebeck effect*, i.e. the generation of a spin current due to temperature gradient, and its reversal *spin-dependent Peltier effect*, the generation of heat current by spin accumulation. An illustration of the two effects is shown in Figure 1.2. Experimental observations have been reported for the first time in ref. [14] and ref. [15].

1.1.2 The spin Seebeck effect

The discovery of the *spin Seebeck effect* in 2008 by Uchida *et al.* [6] represented the most striking contribution to the growing field of spin caloritronics. It consists in the generation, over macroscopic distances, of a spin current \mathbf{j}_S in a ferromagnetic material, in metals as well as in insulators, subjected to a temperature gradient ∇T . The spin current is injected from the ferromagnet into an attached normal metal (NM) with strong spin-orbit coupling (usually platinum) and it is detected by measuring the transverse voltage generated via the inverse spin

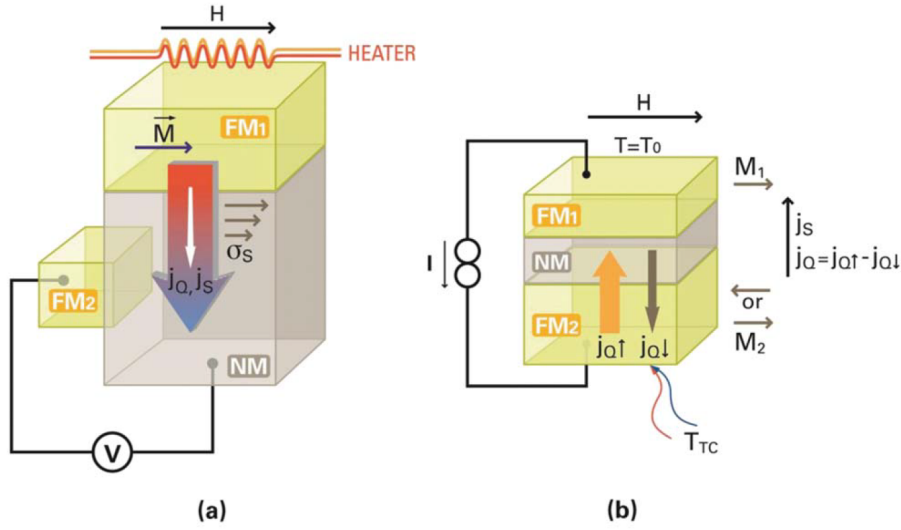


Figure 1.2: Schematic illustration of the spin-dependent thermoelectric phenomena. (a) Spin-dependent Seebeck effect: heat current \mathbf{j}_Q passes from the ferromagnet (FM₁) to a normal metal (NM) and the difference in the Seebeck coefficients generates a spin current \mathbf{j}_S parallel to \mathbf{j}_Q . The spin current is detected by measuring the voltage between the second ferromagnet and the NM. (b) Peltier effect: a charge current passes through the device and the heat flow can be modulated depending on the magnetization direction of the ferromagnets. Image taken from [8].

Hall effect (ISHE) [16, 17]. The electric field generated in the NM is defined by the relation

$$\mathbf{E}_{ISHE} \propto \mathbf{j}_S \times \sigma_{spin} \quad (1.5)$$

where σ_{spin} is the spin polarization vector parallel to the magnetization of the ferromagnet.

This effect is different from the spin-dependent phenomena described in the previous section as the contribution of conduction electrons is negligible. The SSE has been experimentally observed mainly in the two basic configurations illustrated in Figure 1.3, and in several materials ranging from ferromagnetic metal such as permalloy [6], semiconductors [18], magnetic insulator such as yttrium iron garnet (YIG) [19], Heusler alloys [20], and even in non-magnetic materials [21]. Recently, Schmid [22] *et al.* found an upper limit for the transverse SSE which is several orders of magnitude smaller than previously reported.

From a macroscopic point of view, the SSE can be explained with the three-current model described in Section 1.1.1. If we consider a metallic sample subjected to a temperature gradient ∇T and the boundary conditions $\mathbf{j} = 0$ for the charge current and $\Delta\mu = 0$ for bulk spin accumulation, Equation (1.4) yields $\mathbf{j}_S = -\sigma(S_S - S)\nabla T$. Since this relation has no dependence on the spin diffusion length, it predicts the presence of a thermally generated spin current over large scales. However this model is valid only if conduction electrons are involved.

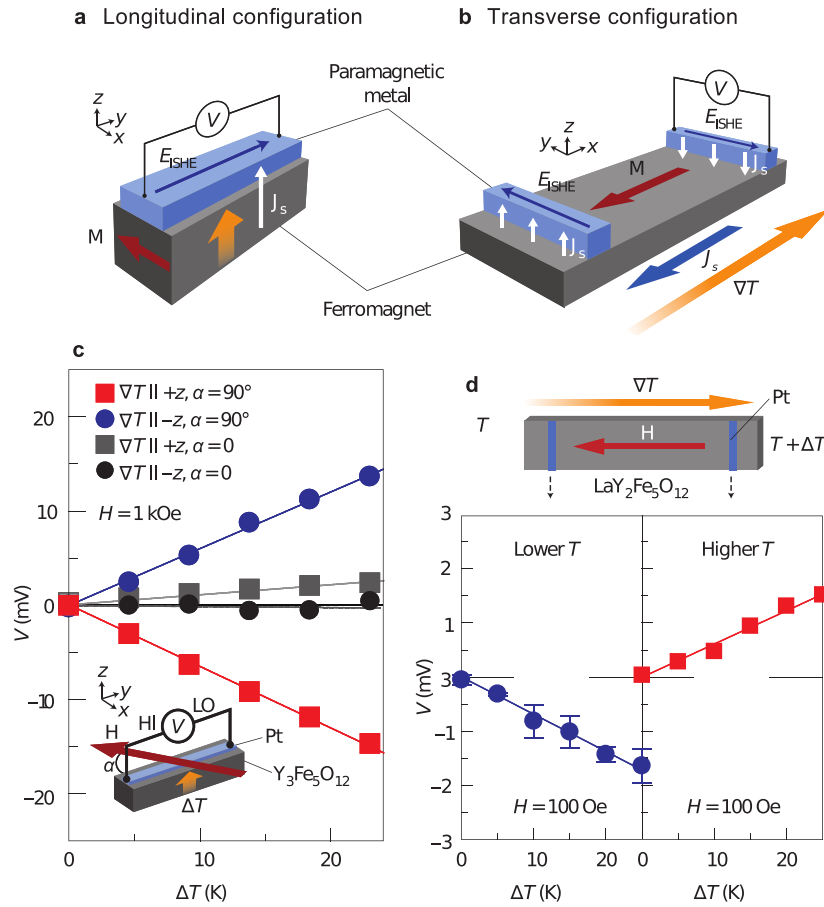


Figure 1.3: Schematic illustration of the spin Seebeck effect. (a) Longitudinal and (b) Transversal SSE configurations. The spin current J_S is injected into a normal metal with high spin-orbit coupling and detected by measuring the transverse voltage generated via the inverse spin-Hall effect. (c) and (d) report typical SSE data of YIG/Pt measured in (a) and (b) configuration, respectively. Image taken from [4].

Today, a theory explaining the SSE at the microscopic level for metal and insulators is still lacking. The widely accepted explanation, is based on the crucial role played by the magnon thermal conductivity and magnon-phonon drag mechanism. The SSE depends critically on the degree to which magnons are brought out of thermal equilibrium when a temperature gradient is applied [23]. In a very simple picture it can be explained in terms of the excitation of the localized spins in the ferromagnet by means of the heat current flowing through it. Recently, Tikhonov *et al.* [24] explained the SSE as a consequence for the fact that, phonons that store the thermal energy (thermal phonons) and the phonons that transfer it (interacting phonons) to magnons, are located in different parts of the phonon spectrum.

The understanding of this phenomenon is very complex and the limited number of existing experiments makes its interpretation very difficult. The theory behind its origin is still highly controversially discussed and a complete explanation is missing. An in-depth description of

the existing theoretical models goes beyond the scope of this chapter. An extensive review on this topic can be found in references [23] and [8].

1.1.3 Effect of heat current on magnon dynamics

In the following section we provide a brief overview of the main experimental developments related to one of the central topics of this thesis: the spin-waves dynamics under the influence of a temperature gradient.

The observation of the spin Seebeck effect in magnetic insulator [19], where a flow of charge is forbidden, suggested the idea that the spin waves play an important role in the generation of the thermally induced ISHE voltage. Motivated by this idea, the dynamics of magnon wavepackets under the influence of a temperature gradient has been the subject of several studies that we report briefly below.

Padrón-Hernández *et al.* [25], investigating the propagation of wavepackets along a YIG films, found that spin waves are amplified when the temperature gradient is applied perpendicular to the YIG slab. The authors interpreted this result in term of a thermally driven spin-transfer torque (see Section 5.1.3) created by spin currents generated through the spin-Seebeck effect. The amplification is attributed to the action of the torque that influences the magnetization opposing the relaxation.

Lu *et al.* in ref. [27] reported on the effects of heat current on the ferromagnetic resonance (FMR) in a trilayered structure consisting of a YIG film grown on gadolinium gallium garnet (GGG) substrate and covered with a nanolayer of platinum. They found that a temperature gradient across the trilayer can modulate the ferromagnetic resonance in the YIG film. In particular, they were able to increase or decrease the relaxation depending on the direction of the thermal gradient with respect to the magnetization. As in ref. [25], they attributed this result to the heat-driven torque exerted on the magnetic moment of the YIG film.

The experimental studies mentioned above were both conducted in the SSE longitudinal configuration (Figure 1.3a). FMR studies on a YIG slab in the transversal SSE geometry (Figure 1.3b), i.e. with an in-plane temperature gradient parallel to the external magnetic field, were instead performed by da Silva and collaborators [28]. The authors observed that when a thermal gradient is applied to the sample, the ISHE voltage across the transversal Pt strips increases in presence of a uniform excitation, whereas it decreases in presence of higher order modes. The amplification of the uniform mode is interpreted as a superimposition of two effect acting simultaneously: the SSE and the spin-pumping effect. The latter consists of the injection of a spin current into a normal metal by the magnetization precession of an adjacent ferromagnet [29].

The above mentioned result has been confirmed in a successive work conducted by the same group [30], where the authors demonstrated that the excitation of the local spin-wave modes at the Pt/YIG interface depends strongly on the direction of the temperature gradient.

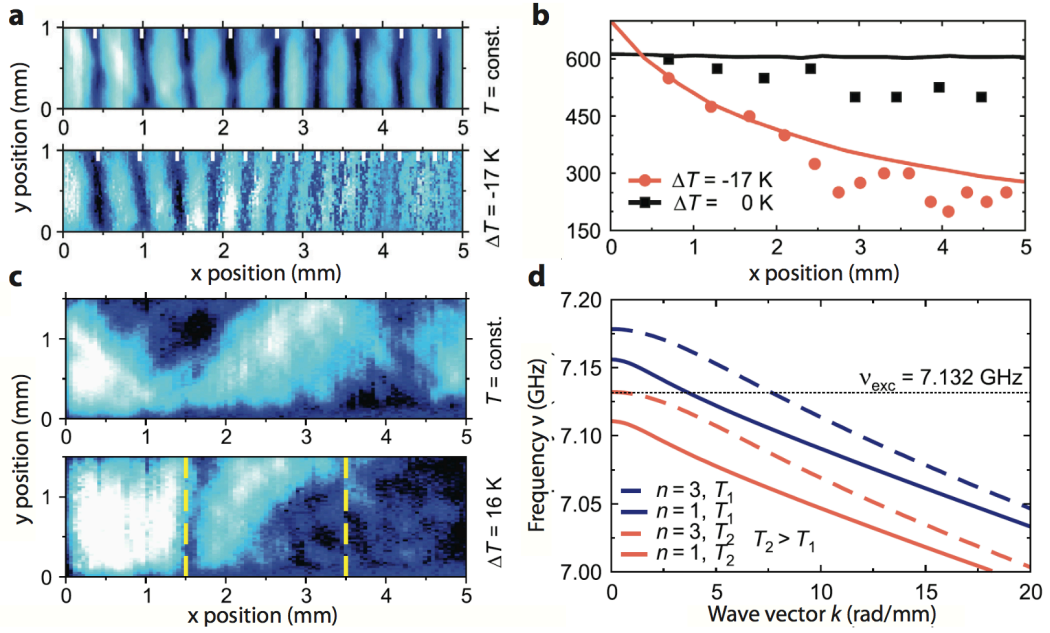


Figure 1.4: Brillouin light scattering measurements of propagating dipolar spin waves in presence of a temperature gradient. (a) Comparison of phase-resolved BLS interference measurements of a YIG waveguide with (bottom) and without (top) temperature gradient revealing a reduction in the wavelength. (b) Comparison between experimental (symbols) and calculated (lines) wavelength values for uniform temperature (black) and an applied thermal gradient (red). (c) BLS measurements of the spin-wave reflection at uniform temperature (top) and in presence of a thermal gradient along the direction of the spin-wave propagation (bottom). The spin waves are excited at the position $x = 0$ mm and propagate along the x direction. (d) Spin-wave dispersion relations calculated for a position near the antenna (blue) and at a distance of 3.5 mm from it (red). Figures taken and adapted from [26].

The possibility to control thermally the relaxation of the spin-waves in GGG/YIG/Pt heterostructures has been confirmed by other groups both for a perpendicular [31] and an in-plane [32] application of the temperature gradient. As for the previous studies, the effect was attributed to a spin-transfer torque caused by a thermally induced spin current.

An interesting work on the influence of a thermal gradient on the propagation of dipolar spin waves has been proposed by Obry *et al.* [26]. Differently from the previous cases, this study was carried out on a YIG sample with no Pt strips on top. By using a phase-resolved Brillouin light scattering technique (BLS), the authors compared the propagation of the spin wave at constant temperature and in presence of an in-plane thermal gradient. This comparison is reported in Figure 1.4. A reduction of the spin wave wavelength is observed for waves propagating from the hot to the cold region, whereas a reflection is observed when propagating from cold to hot. This result has been explained as a consequence of the shift in frequency of the dispersion relation, caused by dependence on temperature of the saturation magnetization.

Ferromagnetic studies of YIG slab subjected to an in-plane temperature gradient have been

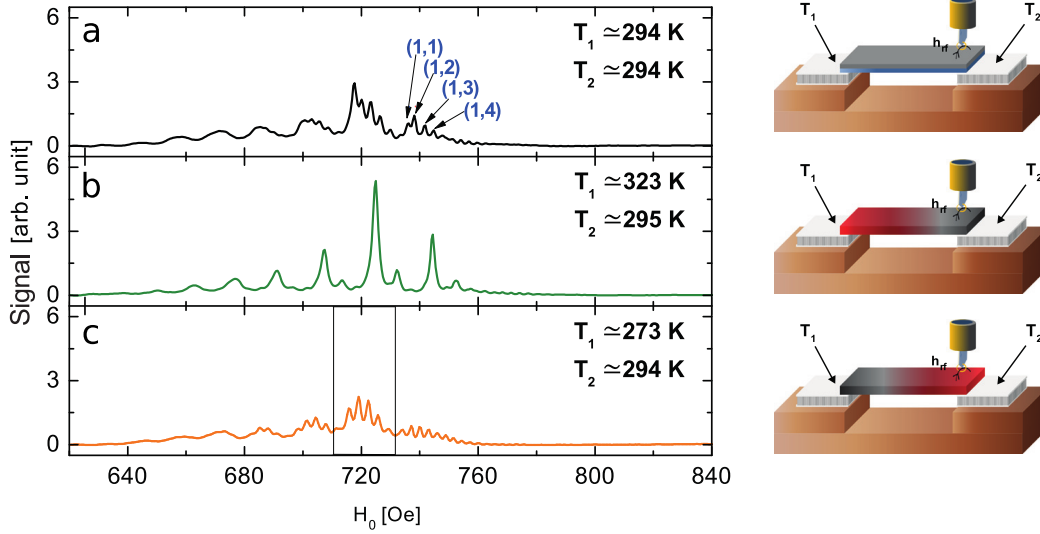


Figure 1.5: Local FMR spectra of a single crystal YIG sample subjected to a temperature gradient $\nabla T \parallel \mathbf{H}$. FMR Spectra of a 2 mm x 10 mm x 25 μm YIG slab at room temperature (a) and in presence of a thermal gradient recorded at the cold (a) and hot end (c). Image taken and adapted from [33].

conducted also by Papa [34, 33] in our group. In this work, the magnetization dynamics of the sample is probed locally by means of a resonating antenna. As for [26] the spin dynamics was conducted by using any Pt/YIG interface effect. In presence of a thermal gradient, the FMR measurements recorded at the cold end of the sample showed a simplification of the spectrum consisting of a suppression of standing wave modes along the direction of the gradient and the enhancement of the remaining peaks. As shown in Figure 1.5, this effect was not observed at the hot end where all the fine structure of the spectrum were still evident.

A further work on heat-driven modulation of spin-waves relaxation has been conducted by Cunha *et al.* and reported in ref. [35]. As shown in Figure 1.6, the experiment was performed on a bare YIG film and on a YIG/Pt structure both with an orthogonal temperature gradient applied as in the standard longitudinal SSE configuration. The authors showed that ∇T affects the relaxation of the propagating waves only on the sample with platinum layer deposited on top. Since the same effect was not observed in the bare YIG, they demonstrated that the effect is caused by the spin injection and the spin pumping effects occurring only at YIG/Pt interface [36, 30].

In Chapter 3 of this thesis we report an experimental work similar to the one described previously. Here, we investigate the propagation of magnetization waves in presence of an in-plane temperature gradient and we found evidence for a novel thermomagnetic effect.

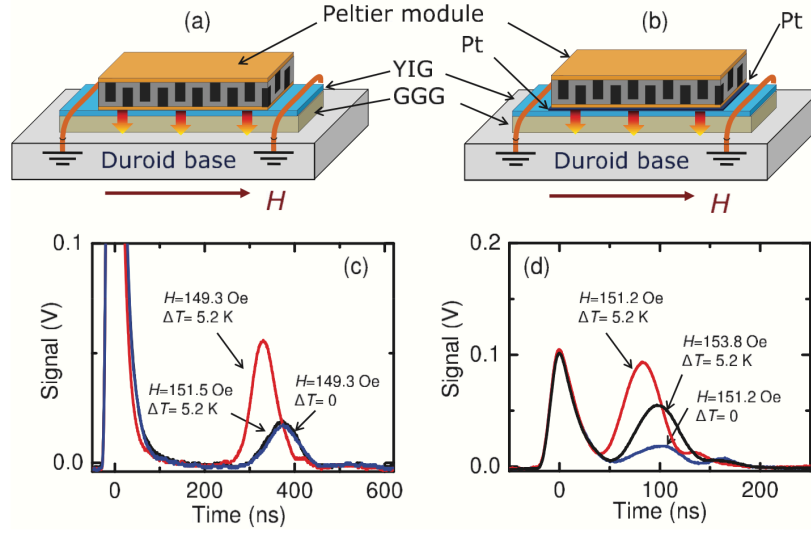


Figure 1.6: Time resolved measurements of a YIG slab and a YIG/Pt structure subjected to a temperature gradient. (a)(b) Illustration showing the sample geometry with a Peltier module used to produce a temperature gradient $\nabla T \perp H$ across the bare YIG (8 μm) film and the YIG (8 μm)/Pt (6 nm) structure. (c) and (d) oscilloscope traces showing the spin-wave pulses measured with a temperature difference $\Delta T = 5.2$ K across the YIG/GGG and the Pt/YIG/GGG structure. Image taken from [35].

1.1.4 Yttrium Iron Garnet and magnon spintronics

The quasi-totality of the experimental works presented in the previous section were carried out on yttrium iron garnet (YIG) samples. The reason for that is related to the magnetic properties of this material that make it the most favourable to conduct studies on the spin waves dynamics.

The YIG is a ferrimagnetic insulator with stoichiometric formula $\text{Y}_3\text{Fe}_2(\text{FeO}_4)_3$ or $\text{Y}_3\text{Fe}_5\text{O}_{12}$ presenting a very complex crystal structure. Its unit cell, with lattice constant $a = 12.376 \text{ \AA}$, accommodates 160 atoms, with 20 Fe^{3+} magnetic ions allocated over in two antiferromagnetic octahedral and tetrahedral sub-lattices. The net magnetic moment per unit cell is $40\mu_B$ and the magnetic dipoles density $n = \frac{20}{a^3} \approx 10^{28} \text{ m}^{-3}$ [37].

YIG is commonly synthesized by liquid phase epitaxy on gadolinium gallium garnet (GGG) because of the very good matching between the two lattice constants. Films grown with this method have a $\langle 111 \rangle$ crystallographic orientation and present a saturation magnetization typically of $4\pi M_s = 1750$ G.

The big success of this material is related to its exceptionally low magnetic damping constant ($\alpha_{\text{YIG}} \approx 10^{-4}$), much smaller than permalloy [38], that allows the propagation of spin waves over centimeter distances [39]. Since its discovery, the YIG has been extensively used in analog devices for the processing of microwave signal such as filters, oscillators or Y-circulators. Today most of them have been displaced by the semiconductor technology.

In recent years YIG is acquiring again popularity in a new emerging field known as *magnonics* or *magnon spintronics*. This new field of research seeks to explore the possibility to use magnons to transport spin information over macroscopic distances without displacement of charges and therefore without producing Joule heating. This advantage would overcome an important limitation of the current CMOS technologies. Since a discussion of this field is beyond the aim of this thesis, we refer to references [40, 41, 42, 43] for more information on this topic.

1.2 Theory of spin waves and ferromagnetic resonance

The ferromagnetic resonance (FMR), is an experimental technique consisting in the resonant absorption of electromagnetic radiations in ferromagnetic materials. It represents a very powerful measurement tool in microwave spectroscopy as it is widely used to probe magnetization and spin waves dynamics.

In this section we provide a brief introduction with the basic theoretical concepts behind the FMR. A more detailed treatment can be found in textbooks such as references [44, 45, 46].

1.2.1 Spin precession and equation of motion

From the theory of electromagnetism we know that a magnetic moment $\boldsymbol{\tau}$ in a homogeneous magnetic field \mathbf{H} experiences a torque

$$\boldsymbol{\tau} = -\mu_0 \boldsymbol{\mu} \times \mathbf{H}. \quad (1.6)$$

where μ_0 is the magnetic permeability in the free space. It defines the the precession around the magnetic field at the Larmor frequency

$$\omega_L = \mu_0 \gamma H \quad (1.7)$$

where $\gamma = g \frac{e}{2m}$ is the gyromagnetic ratio with g being the Landé factor, e the electron charge and m the mass of the electron¹.

In the macroscopic approximation the magnetization vector is defined as $\mathbf{M} = \sum_i^N \frac{\boldsymbol{\mu}_i}{V_m}$ and it represents the total number of magnetic moments per unit volume. Considering the totality of the interacting spins, Equation (1.6) becomes

$$\frac{d\mathbf{M}}{dt} = -\mu_0 \gamma \mathbf{M} \times \mathbf{H}_{\text{eff}}. \quad (1.8)$$

This equation is known as Landau-Lifshitz equation [47] and describes the time evolution of the magnetization. \mathbf{H}_{eff} is the internal effective field that takes into account all the additional contributions to \mathbf{H} such as shape and magnetocrystalline anisotropy or dipolar interactions.

¹For a free electron $g = 2.0023$ and $\gamma = 1.7609 \times 10^{-7} \text{ s}^{-1}\text{Oe}^{-1}$.

1.2. Theory of spin waves and ferromagnetic resonance

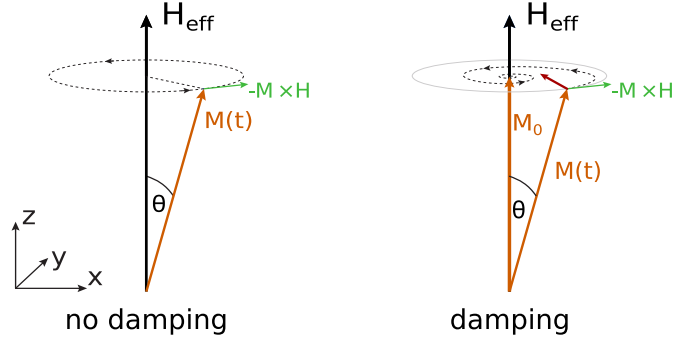


Figure 1.7: Illustration of the magnetization precession in a static magnetic field. At equilibrium the magnetization \mathbf{M} is aligned with the field, i.e. $M_z = M_0$. The magnetization precession is caused by the torque $\mathbf{M} \times \mathbf{H}_{\text{eff}}$, while the damping term $\alpha \frac{\mathbf{M}}{|\mathbf{M}|} \times \frac{d\mathbf{M}}{dt}$, represented by the red arrow, acts to bring the magnetization to the equilibrium position.

As illustrated in Figure 1.7, in absence of losses the magnetization \mathbf{M} precesses around \mathbf{H}_{eff} at the Larmor frequency $\omega_L = \mu_0 \gamma H_{\text{eff}}$ and with a cone angle θ , whereas in presence of damping \mathbf{M} spirals down until it becomes aligned with the field.

The macrospin dynamics of \mathbf{M} with magnetization relaxation is described by the well known Landau-Lifshitz-Gilbert (LLG) equation [48]

$$\frac{d\mathbf{M}}{dt} = -\mu_0 \gamma \mathbf{M} \times \mathbf{H}_{\text{eff}} + \alpha \frac{\mathbf{M}}{|\mathbf{M}|} \times \frac{d\mathbf{M}}{dt} \quad (1.9)$$

where the second term accounts the energy loss due to the damping torque. The Gilbert parameter α determines the magnitude of the damping, i.e. how fast the magnetization relaxes back to equilibrium position, and it can assume different values depending on the material.

Microscopically, the origin of the damping is really complex as there are many processes causing it, such as inelastic conduction electron scattering, phonon scattering or magnon scattering. In general, these processes lead to two kind of damping: a transverse damping that describes the magnetization components M_x and M_y perpendicular to \mathbf{H}_{eff} , and a longitudinal damping that refers to the component M_z parallel to \mathbf{H}_{eff} . In a saturated ferromagnet it is a good approximation to assume that $M_z \simeq M_s$, with M_s being the saturation magnetization, and that its magnitude remains constant during the precession. Hence, we can neglect the longitudinal damping.

1.2.2 Uniform excitation

After describing the damped precessional motion, we consider now the steady state precession of the magnetization induced by the excitation of an homogeneous microwave field. Using

Chapter 1. Introduction

the geometry of Figure 1.7 we add a high frequency oscillating field of the form $\mathbf{h}_{\text{rf}} = h_x e^{i\omega t}$, applied along the x direction. We can write the magnetization and the effective field vectors as

$$\mathbf{M} = \{m_x e^{i\omega t}, m_y e^{i\omega t}, M_0\} \quad \text{and} \quad \mathbf{H} = \{h_x e^{i\omega t}, 0, H_0\}. \quad (1.10)$$

Since the $m_{x,y} \ll M_0$, we can neglect the change of the magnetization in the z direction thus Equation (1.8) can be written as

$$i\omega m_x = \mu_0 \gamma H_0 m_y \quad \text{and} \quad i\omega m_y = \mu_0 \gamma (M_0 h_x - m_x H_0) \quad (1.11)$$

Without considering the dissipation term, the transverse susceptibility is given by

$$\chi_{xx} = \frac{m_x}{h_x} = \frac{\omega_0 \omega_M}{\omega_0^2 - \omega^2}, \quad (1.12)$$

with

$$\omega_0 = \mu_0 \gamma H_0 \quad \text{and} \quad \omega_M = \mu_0 \gamma M_0. \quad (1.13)$$

If $\omega = \omega_0$ the system enters in resonance condition and the precession amplitude diverges. Introducing the loss term to account for dissipation (i.e. $\alpha > 0$), the resonance is broadened and the susceptibility becomes

$$\chi_{xx} = \frac{\omega_M (\omega_0 + i\alpha\omega)}{(\omega_0 - i\alpha\omega)^2 - \omega^2}. \quad (1.14)$$

Here we described a very simple case finding the expression of the susceptibility for an oscillating magnetic field acting in one direction only. More in general, the response of the magnetization $\mathbf{m}(t)$ to a high-frequency field \mathbf{h}_{rf} , can be written in the form $\mathbf{m}(t) = \hat{\chi} \mathbf{h}_{\text{rf}}$, where $\hat{\chi}$ is a tensor known as *Polder susceptibility tensor*.

The frequency dependence of the real (χ') and imaginary part (χ'') of the susceptibility χ_{xx} , is shown in Figure 1.8. The former gives the response of m_x in phase with the excitation, while the latter represents the dissipation term and it is characterized by a Lorentzian lineshape. At the resonance ($\omega = \omega_0$) χ'' is at the maximum point while χ' crosses the zero and changes sign. This is an indication that \mathbf{m} and \mathbf{h}_{rf} are out of phase by $\pi/2$. The power absorbed by a magnetic sample subjected to a microwave power is proportional to the imaginary part. In a standard FMR experiment, carried out by sweeping the excitation frequency at a constant magnetic field or vice-versa fixing the frequency and sweeping the field, χ'' is the quantity being measured.

The linewidth (FWHM) of the FMR Lorentzian peak provide important information on damping. It is given by

$$\Delta H = \Delta H_i + \Delta H_G, \quad (1.15)$$

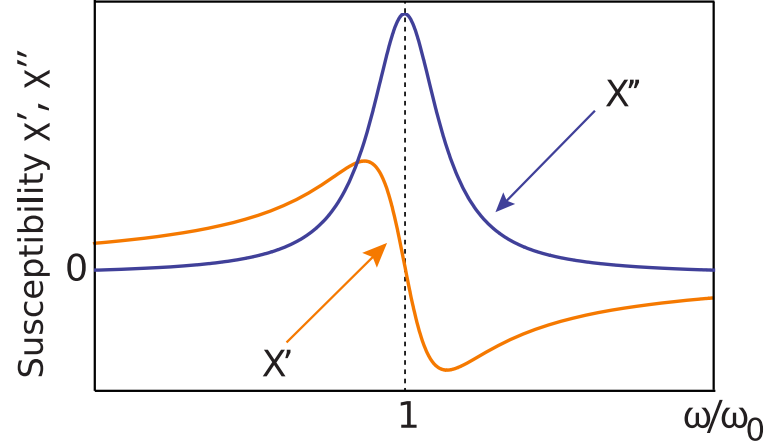


Figure 1.8: Real and imaginary parts of the magnetic susceptibility χ .

where ΔH_i is related to the inhomogeneous broadening caused by sample defects or other magnetic field inhomogeneities, whereas ΔH_G denotes the broadening due to the Gilbert's intrinsic damping and it is defined as

$$\Delta H_G = \frac{2\omega}{\gamma} \alpha. \quad (1.16)$$

The precessional motion of the magnetization is significantly affected by the shape anisotropy and thus by the demagnetizing field, defined as

$$\mathbf{H}_d = -\hat{\mathbf{N}}_d \mathbf{M} = \begin{pmatrix} N_x & 0 & 0 \\ 0 & N_y & 0 \\ 0 & 0 & N_z \end{pmatrix} \mathbf{M}. \quad (1.17)$$

$\hat{\mathbf{N}}_d$ is the demagnetizing tensor, its element depends on the geometry of the sample and their sum is so that

$$N_x + N_y + N_z = 1. \quad (1.18)$$

With $\mathbf{H}_{\text{eff}} = \mathbf{H}_0 + \mathbf{H}_d$, the general equation for the resonance dispersion relation of the uniform precession [49] is expressed by

$$\omega = \mu_0 \gamma \sqrt{(H_0 + (N_x - N_z) M_S)(H_0 + (N_y - N_z) M_S)} \quad (1.19)$$

In a rectangular film, tangentially magnetized in the z direction, with the thickness \ll width and length, $N_y = N_z = 0$ and $N_x = 1$. With these conditions Equation 1.19 yields

$$\omega = \mu_0 \gamma \sqrt{H_0(H_0 - M_S)}. \quad (1.20)$$

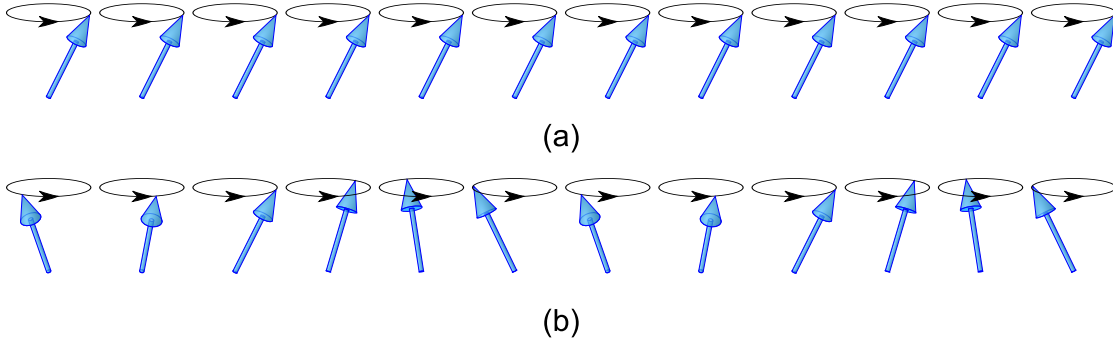


Figure 1.9: Schematic illustration of one dimensional chain of spins. (a) Uniform mode: all the spins precess simultaneously with the same phase. (b) Spin wave state: precession phase varies along the chain.

In the other hand, for a normally magnetized film, lying in the yz plane, $N_z = 1$ and $N_x = N_y = 0$ and Equation 1.19 becomes

$$\omega = \mu_0 \gamma (H_0 - M_S). \quad (1.21)$$

1.2.3 Non-uniform excitation and spin waves

A simultaneous precession of all the spins caused by a FMR excitation corresponds to the uniform mode characterized by infinite wavelength ($\lambda = \infty$) and zero wave vector $\mathbf{k} = 0$. However, in magnetically ordered systems, the spins can precess at a different phase with respect to the others. This leads to a spin wave mode with finite wavelength $\lambda < \infty$ and wave vector $\mathbf{k} \neq 0$. A schematic representation of a chain of spins for both uniform and spin wave mode is reported in Figure 1.9.

In the simple case of a chain of spins subjected to a constant magnetic field \mathbf{H}_0 , if any external excitation is applied, all the magnetic moment are aligned along \mathbf{H}_0 . If one of the two moment at the chain extremity is led out of equilibrium by an inhomogeneous RF excitation, it starts to precess at Larmor frequency around \mathbf{H}_0 . This motion affects the adjacent moment that in turn starts to precess at the same frequency but with different phase. One by one all the spins of the chain start to experience the high-frequency field produced by the closest moment causing an oscillating mode of the whole ensemble and characterized by a spatial variation of the phase. This dephased excitation can be seen as a wave travelling through the spin chain.

Basically there are two type of interactions: the quantum mechanical Heisenberg interaction between adjacent spins, and the dipolar interactions caused by the field produced by the neighbouring spins and by the external magnetic field. The first type is responsible for short range wave excitation having wavelength $\lambda \simeq a$, with a being the lattice constant of the crystal, whereas the second ones are related to long range waves having wavelength $\lambda \gg a$. Long-range excitations of dipolar nature are known as magnetostatic spin wave (MSW) modes. Here, we address only this typology providing a brief overview for the specific case of thin films.

Magnetostatic spin waves

The first theoretical work on magnetic standing waves in spheroids was carried out by Walker [50] in 1957. After that, important studies were conducted by Fletcher and Kittel [51] and in particular by Damon and Heshbach [52, 53, 54].

The MSWs are solution of the Maxwell's equations under magnetostatic approximation. They occur at discrete eigenfrequencies and have characteristic wavelength of the order of the linear dimension of the sample. In this section, we restrict our discussion to a presentation of the classification of the MSWs and their dispersion relation. A complete theoretical treatise can be found in several textbook such as [45] and [46]

There are essentially three distinct classes of magnetostatic spin waves that can be excited in magnetic thin films, and they are determined by the orientation of the spin wave propagation with respect to the applied magnetic field. As illustrated in Figure 1.10, each class of MSW mode is characterized by a different dispersion relation $f(k)$.

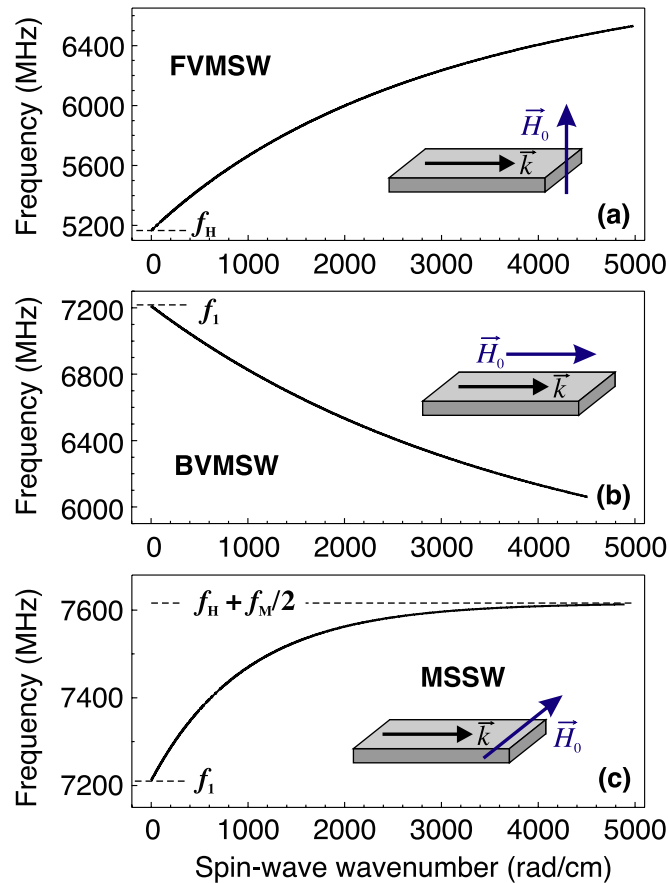


Figure 1.10: Typology of magnetostatic spin wave modes as a function of the direction of the internal effective field H_0 . Dispersion characteristic for (a) forward volume magnetostatic waves, (b) backward volume magnetostatic waves and (c) magnetostatic surface spin waves. The curves are calculated for $H_0 = 1845$ Oe and $M_s = 1750$ G. Image taken from [41].

In a normally magnetised thin film, the existing modes are so-called forward volume magnetostatic spin wave (FVMSW) modes [54]. Their wave vector \mathbf{k} is perpendicular to \mathbf{H}_0 and the dispersion curve, illustrated in Figure 1.10a, is defined in good approximation by the expression [45]

$$f_{FVMSW} = \sqrt{f_H \left(f_H + f_M \left(1 - \frac{1 - \exp(-kd_0)}{kd_0} \right) \right)}, \quad (1.22)$$

where d_0 is the thickness of the film, $f_H = \mu_0 \gamma H_0$ and $f_M = \mu_0 \gamma M_s$, with H_0 and M_s being the effective internal field and the magnetization at saturation respectively. As \mathbf{k} increases, the frequency tends to the value $f_1 = \sqrt{f_H(f_H + f_M)}$, whereas with decreasing \mathbf{k} the frequency tends to f_H . The dispersion curve depends on the thickness of the sample, but it is independent on the wave propagation in the plane of the film.

If the magnetic sample has an in-plane magnetization [53], we have two typologies of MSW modes: the backward volume magnetostatic waves (BVMSW), occurring when the wave propagation is parallel to the magnetization ($\mathbf{k} \parallel \mathbf{H}_0$), and the magnetostatic surface spin waves (MSSW), associated with a propagation perpendicular to the magnetization ($\mathbf{k} \perp \mathbf{H}_0$).

The dispersion curve of the BVMSW modes is reported in Figure 1.10b and it is given by the relation

$$f_{BVMSW} = \sqrt{f_H \left(f_H + f_M \left(\frac{1 - \exp(-kd_0)}{kd_0} \right) \right)}. \quad (1.23)$$

As the FVMSWs, the BVMSWs are volume modes. They present a dispersion relation with negative slope and thus a negative group velocity $v_{gr} = \partial f / \partial k$. This means that an increase in \mathbf{k} leads to a decrease in the resonant frequency.

Unlike the two classes presented before, the magnetostatic surface spin waves (MSSW) are associated to the modes propagating on the surface of the film. Their dispersion relation is illustrated in Figure 1.10c and is given by the expression

$$f_{MSSW} = \sqrt{(f_H + f_M/2)^2 - (f_M/2)^2 \exp(-2kd_0)}. \quad (1.24)$$

As for BVMSW modes, when $\mathbf{k} \rightarrow 0$ the frequency tends to f_1 , namely the FMR mode of an in-plane magnetized thin film, whereas an increasing of the wave vector leads to the values $f_H + f_M/2$.

In general, for a spin waves propagating with wave vector $\mathbf{k} = (k_x, k_y, k_z)$ in a finite slab laying in the yz plane with dimensions l_y and l_z , the components k_y and k_z can have only discrete values. They depend on the sample dimensions as follow

$$k_y = \frac{n_y \pi}{l_y} \quad \text{and} \quad k_z = \frac{n_z \pi}{l_z}, \quad (1.25)$$

where the mode order $n_{y,z}$ can assume only positive integer values.

1.3 Thesis organization

This thesis is divided in two main parts. The first one includes Chapters 2, 3 and 4 and it deals with the effect of a heat current on the spin dynamics in insulating samples at macroscopic scale. In Chapter 2 we present the experimental methods and techniques used to carry out measurements on magnetic insulators. Chapter 3 addresses the magnetic Seebeck effect while in Chapter 4 we present and discuss further experimental data.

In the second part, which includes Chapters 5 and 6, we report our investigation of metallic nanowires when subjected to a temperature gradient. Hence, we move from insulators to conducting materials and from macro to a nanoscale. Chapter 5 functions as an introduction to the second part. Here, we describe the nanowire fabrication and characterization methods, and we present and discuss of the experimental data recorded via laser modulated FMR technique. The observation of the linear response to a heat-driven spin torque is instead reported in Chapter 6.

Finally, Chapter 7 summarizes this thesis with concluding remarks and suggestions for future investigations.

2 Experimental setups and techniques

In the following chapter we presents the experimental techniques employed to carry out investigations on magnetic insulators subjected to a temperature gradient. In Section 2.1 we describe the experimental setup we designed to conduct continuous wave ferromagnetic resonance. Pulsed techniques for time resolved measurements are instead described in Section 2.2. Finally in Section 2.2.1 we illustrate the techniques used to generate and measure the temperature gradient.

2.1 Continuous wave ferromagnetic resonance

The ferromagnetic resonance is an experimental technique consisting in the resonant absorption of electromagnetic radiations in ferromagnetic materials. The general concept behind the FMR is based on the response of the magnetization \mathbf{M} to an external perturbation generated by an oscillating magnetic field \mathbf{h}_{rf} , applied perpendicular to a DC field \mathbf{H}_0 . The magnetization response can be monitored measuring the susceptibility (χ'' , see Section 1.2) by inductive methods or via imaging techniques, such as Kerr imaging [55], Brillouin Light scattering [56, 57] or others near-field scanning probe technique [58].

In our experiment we detect inductively the FMR by using an home-made spectrometer appositely designed. A simplified schematics of the setup is illustrated in Figure 2.1. The microwaves are produced by a R&S SGS100A microwave generator ($f_{\text{out}} = 0.1 - 12$ GHz) with a maximum output power of 16 dBm. The signal generated by the source is passed through a circulator, which protects the microwave source from any reflected power, and then sent to a resonator placed between the pole of a electromagnet. This is used to generate the DC magnetic field and is driven by a Bouhnik power supply. The microwaves that are reflected back by the resonator are redirected by the circulator to a zero bias Schottky detector (model Narda 4503A-03). This provides an output signal proportional to the power of the microwaves, thus it allows a direct measurement of the power absorbed by the specimen. During the measurement the static magnetic field is swept and the sample is exposed to microwave radiation typically at the resonance frequency f_{res} of the resonator. When the applied field

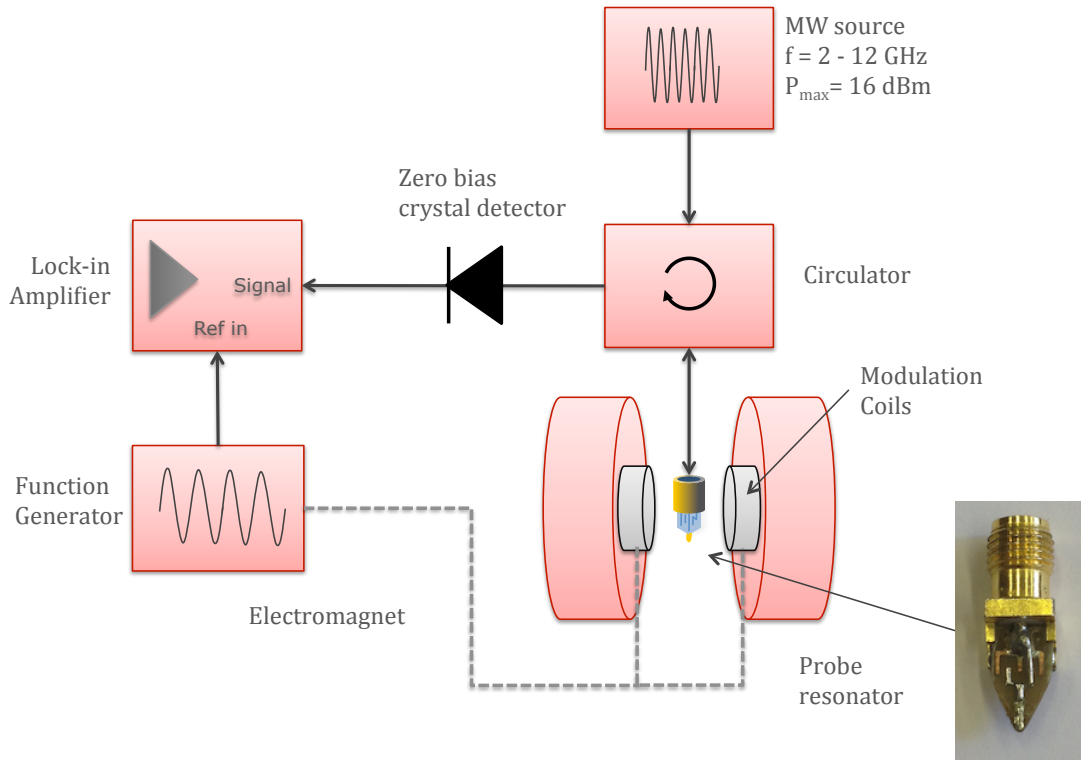


Figure 2.1: Schematics of the experimental setup for lock-in FMR detection with field modulation technique. The probe resonator in the figure can be replaced by a resonant cavity at X-band frequencies

H_0 and f_{res} meet the FMR condition, the microwave power absorbed by the sample increases significantly, with the subsequent decreasing of the power reflected by the resonator. By measuring this power variation we are able to reconstruct the FMR line shape by sweeping H_0 through the resonance condition.

To carry out CW FMR studies we employ two typology of resonance schemes, namely a conventional microwave X-band cavity and a local microwave resonator¹ shown in the photo of Figure 2.1. It consists of a short-circuited microstrip line, coupled to an SMA connector, with a copper coil of about $50 \mu\text{m}$ in diameter at its end. In order to ensure a good signal detection, the resonator needs to be placed as close as possible to the surface of the sample (400 to $600 \mu\text{m}$ away). The main advantage of using this method with respect to a cavity, is that we can locally probe the magnetization dynamics of the sample. This technique has been widely used in references [34, 33] for FMR studies of magnetostatic modes of a YIG slab subjected to a temperature gradient.

To improve significantly the sensitivity of the measurement system, we use a lock-in detection with field modulation technique. The DC magnetic field is modulated by using two coils placed around the poles of the electromagnet and driven with a sinusoidal wave generated

¹Produced by ez SQUID Mess- und Analysegeräte, Sinn, Germany

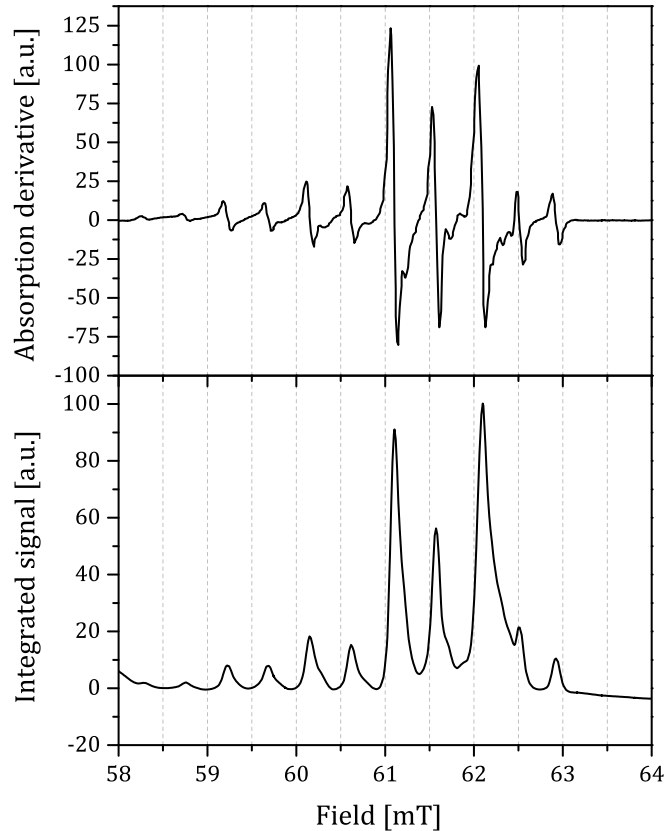


Figure 2.2: FMR spectrum of a single crystal YIG slab measured with field modulation technique. Absorption derivative (top) and integrated signal (bottom) obtained with a field modulation of 0.3 Oe at 156 Hz. We can clearly distinguish several Lorentzian peaks corresponding to the different magnetostatic modes.

by a function generator. Alternatively, this can be done by directly modulating the DC field H_0 through the programming voltage sent to the power supply of the electromagnet. The resulting magnetic field is a sinusoidal wave of amplitude H_m and frequency f_m with DC offset H_0 . The signal obtained with this method is proportional to the derivative of the absorption (Lorentzian peak) with respect to the applied field. Figure 2.2 shows an example of FMR spectrum of YIG single crystal slab recorded with this technique.

A further technique to conduct electrically detected FMR in magnetic nanostructures is presented in Chapter 5.

2.2 Time resolved and pulsed technique

The previous setup can be modified to conduct time resolved measurements. As shown by the schematics of Figure 2.3, pulses of microwaves can be produced by mixing the signal of the RF source with the one generated by a pulse pattern generator (Agilent 81110A). This method

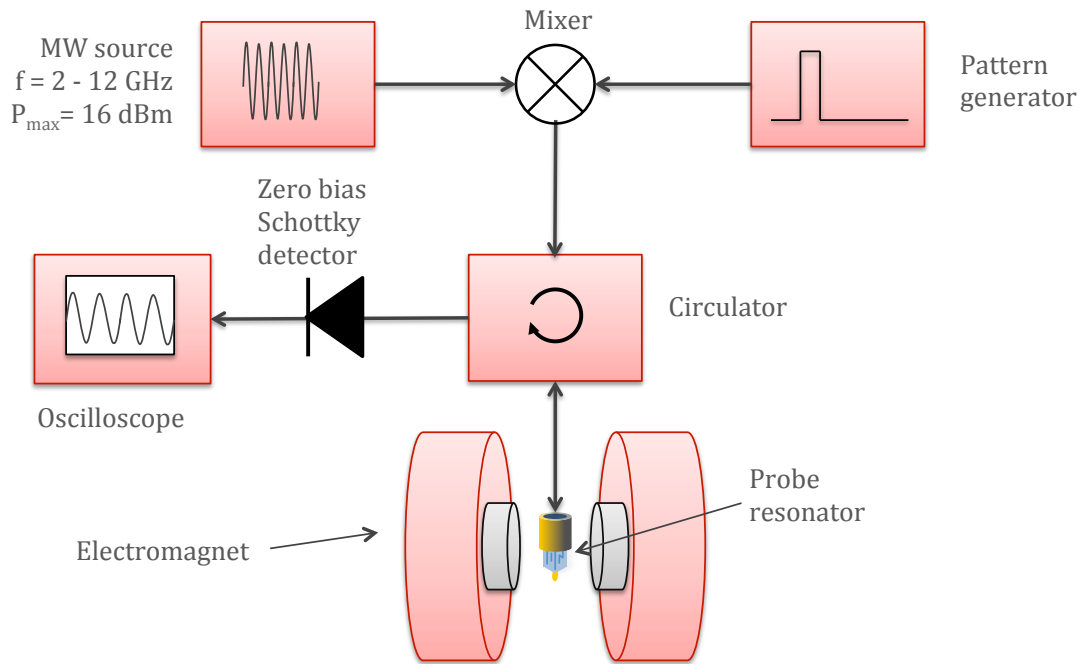


Figure 2.3: Schematics of the experimental setup for time resolved measurements. Microwave pulses are generated by mixing the microwaves with the pulse produced by the pattern generator.

allows us to produce pulses of microwaves at the GHz range with tens of ns in duration. The drawback of using the mixer (Miteq DB0218LW2) is that it does not provide a good insulation (typically 30 dB), that is, it causes the presence of microwave even after the pulse. This problem can be avoided by putting two mixers in series or alternatively replacing the mixer with a fast switch. Nevertheless, in this case the minimum duration of the pulse is limited by the rising and falling times of the switch..

A circulator is used to send the pulsed signal to the resonator and redirect it to a crystal detector. By measuring the output signal with an oscilloscope, we are able to monitor the time evolution of the magnetization relaxation of the sample after the pulse excitation. By sweeping the magnetic field and recording at the same time the oscilloscope traces, we can obtain measurement data similar to graph reported in Figure 2.4. Here, the measured signal is plotted as a function of the time and the applied magnetic field. The advantage of this methods is that we can extract FMR spectrum at a desired time after the pulse. In the left graph of the same figure we compare FMR spectrum obtained with modulation technique with the spectrum of the same sample obtained at 50 ns after the pulse.

This setup has been adapted to carry out transmission measurements by using two probes, one to excite and one to detect. Details on this system are provided in Section 3.2.

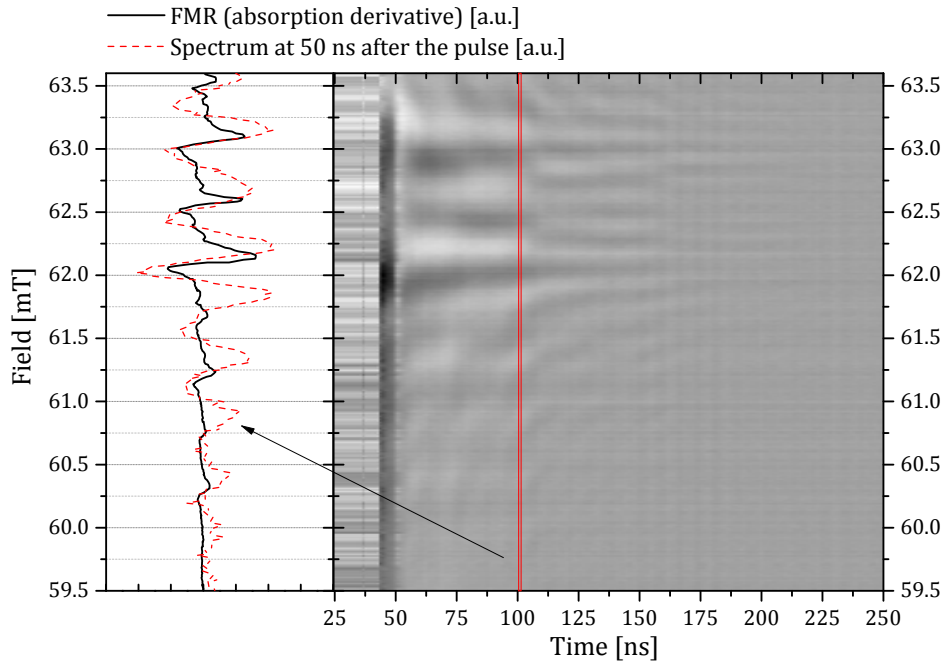


Figure 2.4: Time resolved measurement of a single crystal slab of YIG. Data are obtained by sending microwave pulses of 4 GHz in frequency and 25 ns in duration. In the left graph we compare the spectrum obtained 50 ns after the pulse with the FMR obtained with standard field modulation technique.

2.2.1 Temperature gradient generation and imaging

As the aim of the work is to study the effect of a heat current on the magnetization dynamics, one of the main experimental challenges is the creation of a temperature gradient in the samples under investigation. In this section we limit our description to the case of a magnetic insulators. A methods for creating a strong thermal gradient in magnetic nanostructures is reported in Chapter 5.

The simplest scheme employed to create an in-plane temperature gradient in a YIG slab is illustrated in Figure 2.5a. Here the sample is positioned with its ends touching the top of two Peltier elements (model 693-5135 from RS Components) sitting on a piece of copper for heat dissipation. The thermal contact is ensured by a conventional thermal tape commonly used in electronics. As illustrated in Figure 2.5b, the same concept is used to create a perpendicular to the plane temperature gradient in a disk of YIG squeezed between two Peltier elements. An alternative methods for the generation of a heat current on these samples is to exploit the Joule heating produced by a SMD resistor. Also in this case a thermal tape is used to guarantee a good heat conductivity. Even if this method does not provide a very good heat control compared to the Peltier elements, it represents a good replacement for the cases where these thermoelectric devices cannot work, e.g. at low temperature.

We verify the generation of the temperature gradient with a thermal camera model PCE-TC3.

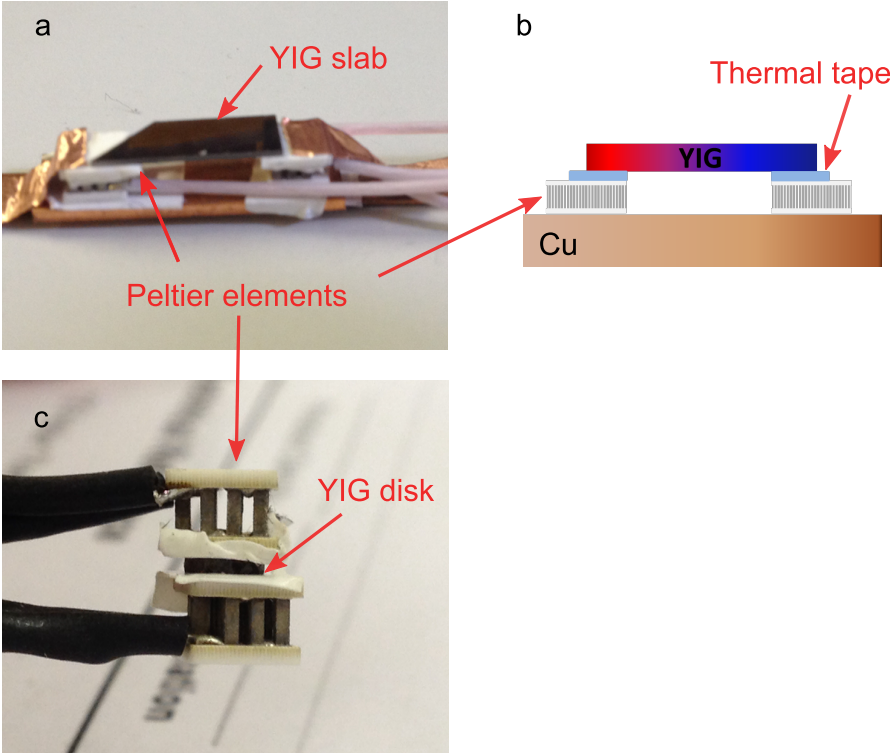


Figure 2.5: Illustrations of the setups for the temperature gradient generation. The thermal gradient can be created in-plane (a)(b) or out of plane (c).

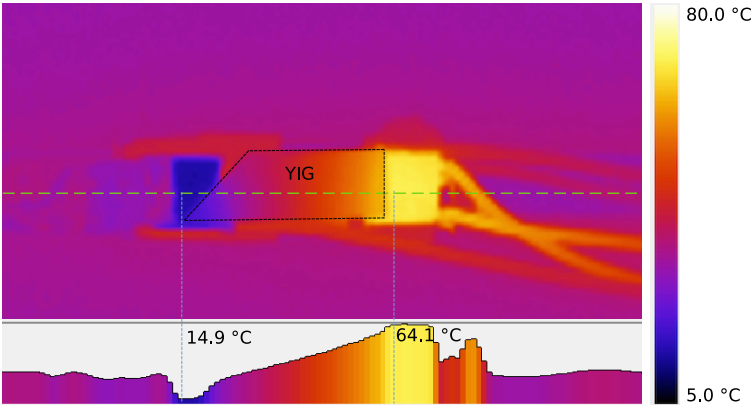


Figure 2.6: Infrared image example of single crystal slab of YIG subjected to a temperature gradient.

2.2. Time resolved and pulsed technique

In Figures 2.6 we report an example of infrared image referring to the setups illustrated in Figure 2.5a.

3 The magnetic Seebeck effect

The irreversible thermodynamics of a continuous medium with magnetic dipoles [59] implies that a thermal gradient across a YIG slab, in the presence of magnetization waves, produces a magnetic induction field that is the magnetic analog of the well known Seebeck effect. This thermally induced magnetic field influences the time evolution of the magnetization, in such a way that we can modulate the magnetization precession by applying a temperature gradient. Studies on the effect of a thermal gradient on the dynamics of the magnetization waves have already been discussed in Section 1.1.3.

In this chapter we present the experimental evidence for a magnetic Seebeck effect by conducting time-resolved transmission measurements in a thin slab of YIG crystal when this is subjected to a temperature gradient [60]. In Section 3.1 we discuss the thermodynamic formalism and the theoretical prediction. In Section 3.2 we give a description of the experimental setup used to conduct studies on the propagation of magnetization waves. Finally, in Section 3.3, we present our measurements along with a discussion on results achieved.

3.1 Thermodynamic formalism for a magnetic insulator subjected to a thermal gradient

The irreversible thermodynamics for a continuous medium with magnetic dipoles has been described by Bréchet and Ansermet in ref. [59]. This formalism defines the relations between currents and force densities and it predicts the coupling between a magnetization force density and a heat current.

In a magnetic insulator like YIG, where there is no charge transport ($\mathbf{J}_e = 0$), no charge accumulation ($\nabla V = 0$) and uniform spatial distribution¹ ($\nabla\mu = 0$), the transport equation of ref. [59] implies a relation between a magnetization force density and a thermal force density, defined

¹ μ is the chemical potential of the material [59].

as

$$\mathbf{M}\nabla\mathbf{B}_{ind} = \lambda nk_B \nabla T, \quad (3.1)$$

where $\lambda > 0$ is a phenomenological dimensionless parameter, k_B the Boltzmann's constant and n the Bohr magneton number (for YIG $n = 1.1 \cdot 10^{28} \text{ m}^{-3}$).

In a bulk system, the magnetization force density can be expressed as a Laplace force [61] in terms of magnetic bound current density $\mathbf{J}_M = \nabla \times \mathbf{M}$ [62]. Hence, we can write

$$\mathbf{M}\nabla\mathbf{B}_{ind} = \mathbf{J}_M \times \mathbf{B}_{ind}. \quad (3.2)$$

By using the appropriate vectorial identities, the Equations (3.1) and (3.2) yield

$$\mathbf{B}_{ind} = \boldsymbol{\varepsilon}_M \times \nabla T, \quad (3.3)$$

where $\boldsymbol{\varepsilon}_M$ is a phenomenological vector defined as

$$\boldsymbol{\varepsilon}_M = -\lambda nk_B (\nabla \times \mathbf{M})^{-1}. \quad (3.4)$$

The Equation (3.3) implies that a temperature gradient ∇T can induce a field \mathbf{B}_{ind} orthogonal to it. This is the magnetic analogue of the Seebeck effect in an insulator [10, 9]. Because of this analogy we refer to it as Magnetic Seebeck effect (MSE). It should be noted that the MSE can occur only when $\nabla \times \mathbf{M} \neq 0$, i.e. when we have an inhomogeneous magnetization. Using the appropriate vectorial identities we can write Equation (3.3) as

$$\mathbf{B}_{ind} = \boldsymbol{\varepsilon}_M \times \nabla T \quad (3.5)$$

$$= -\lambda nk_B (\nabla \times \mathbf{M})^{-1} \times \nabla T \quad (3.6)$$

$$= -\frac{\lambda nk_B}{M_s^2} (\nabla T \cdot \nabla^{-1}) \mathbf{m} \quad (3.7)$$

$$= -\mu_0 \mathbf{k}_T \cdot \nabla^{-1} \mathbf{m} \quad (3.8)$$

where $\nabla^{-1} \cdot \nabla = 1$, μ_0 the magnetic permeability of the vacuum and \mathbf{k}_T the thermal vector proportional to the temperature gradient

$$\mathbf{k}_T = \frac{\lambda nk_B}{\mu_0 M_s^2} \nabla T. \quad (3.9)$$

The consequence of the thermally generated induction field is to influence the time evolution of the magnetization, described by the LLG equation (Section 1.2)

$$\frac{d\mathbf{M}}{dt} = -\gamma \mathbf{M} \times \mathbf{B}_{eff} + \frac{\alpha}{M_s} \mathbf{M} \times \frac{d\mathbf{M}}{dt}. \quad (3.10)$$

3.1. Thermodynamic formalism for a magnetic insulator subjected to a thermal gradient

Here, the field \mathbf{B}_{eff} is given by several contributions

$$\mathbf{B}_{eff} = \mathbf{B}_{ext} + \mathbf{B}_{dem} + \mathbf{B}_{ani} + \mathbf{B}_{ind}, \quad (3.11)$$

where \mathbf{B}_{ext} is the applied magnetic field, \mathbf{B}_{dem} the demagnetizing field, \mathbf{B}_{ani} the anisotropy field, and \mathbf{B}_{ind} the thermal induction field generated by the Magnetic Seebeck effect (Equation (3.3)). We remind that for YIG the Gilbert damping parameter is of the order $\alpha \simeq 10^{-4}$ [63] while the saturation magnetization at room temperature is $\mu_0 M_s = 176$ mT [64].

Since our aim is to investigate the effect of a heat current on the magnetization dynamics, the next step is to determine how the magnetization responds to an external excitation when a temperature gradient is applied. In other words, we have to find the expression for the magnetic susceptibility.

3.1.1 Linear response of the magnetization to a small excitation

We consider now a thin slab of YIG subjected to a small local excitation and to a temperature gradient applied in a direction parallel to its long axis.

The external magnetic field \mathbf{B}_{ext} applied to the sample has two contributions: a constant field $\mathbf{B}_0 = B_0 \hat{\mathbf{z}}$ parallel to the slab, and a small oscillating field $\mathbf{b} = b_x \hat{\mathbf{x}} + b_y \hat{\mathbf{y}}$ orthogonal to \mathbf{B}_0 . As consequence of this, in the linear approximation, the magnetization \mathbf{M} consists of a uniform term given by the magnetization at saturation $\mathbf{M}_s = M_s \hat{\mathbf{z}}$, and the response to the small excitation $\mathbf{m} = m_x \hat{\mathbf{x}} + m_y \hat{\mathbf{y}}$ with $m \ll M$.

Therefore, we can write the linear response of the magnetization according to the LLG equation and we obtain

$$\frac{d\mathbf{m}}{dt} = -\gamma(\mathbf{m} \times \mathbf{B}_0 + \mathbf{M} \times \mathbf{B}_1) + \frac{\alpha}{M_s} \mathbf{M}_s \times \frac{d\mathbf{m}}{dt}, \quad (3.12)$$

where \mathbf{B}_1 is the first-order magnetic induction field that take into account the MSE and defined as

$$\mathbf{B}_1 = \mathbf{b} - \mu_0(\mathbf{k}_T \cdot \nabla^{-1})\mathbf{m}, \quad (3.13)$$

The Equation (3.12) can be written in Cartesian coordinates as follows

$$\begin{aligned} \frac{dm_x}{dt} &= (\omega_0 + \omega_M \mathbf{k}_T \cdot \nabla^{-1})m_y + \alpha \frac{dm_y}{dt} - \omega_M \mu_0^{-1} b_y, \\ \frac{dm_y}{dt} &= -(\omega_0 + \omega_M \mathbf{k}_T \cdot \nabla^{-1})m_x - \alpha \frac{dm_x}{dt} - \omega_M \mu_0^{-1} b_x, \end{aligned} \quad (3.14)$$

with ω_0 and ω_M the angular frequencies given by

$$\omega_0 = \gamma B_0, \quad \text{and} \quad \omega_M = \gamma \mu_0 M_s. \quad (3.15)$$

Chapter 3. The magnetic Seebeck effect

In a stationary state, the excitation field \mathbf{b} oscillates at frequency ω leading the magnetization response \mathbf{m} to oscillate at the same frequency. If we write it in Fourier series (see ref. [60]), the eigenstates of the excitation field $b_{\mathbf{k}}$ and of the linear response of the magnetization $m_{\mathbf{k}}$, are related by

$$m_{\mathbf{k}} = \mu_0^{-1} \chi_{\mathbf{k}} b_{\mathbf{k}} \quad (3.16)$$

The term $\chi_{\mathbf{k}}$ of Equation (3.16) corresponds to the magnetic susceptibility and it can be expressed as

$$\chi_{\mathbf{k}} = -\frac{1}{\Omega - \Omega_0 + i(\alpha\Omega + \mathbf{k}_{\Gamma} \cdot \mathbf{k}^{-1})} \quad (3.17)$$

where Ω and Ω_0 are dimensionless parameters given by

$$\Omega = \frac{\omega}{\omega_M}, \text{ and } \Omega_0 = \frac{\omega_0}{\omega_M}. \quad (3.18)$$

The magnetic susceptibility is affected by the demagnetizing field $\mathbf{B}_{dem} = -\mu_0 m_x \hat{\mathbf{x}}$ that is responsible for breaking the spatial symmetry in the sample and creating an elliptic precession cone. It causes the damping along the x direction to differ from the damping along the y direction and, as a consequence, $\chi_{\mathbf{k}x}$ differs from $\chi_{\mathbf{k}y}$. Therefore, considering the Kittel's formula for the resonance frequency $\sqrt{\omega_0(\omega_0 + \omega_M)}$, we can express the magnetic susceptibility as

$$\chi_{\mathbf{k}x,y} = -\frac{1}{\Omega - \sqrt{\Omega_0(\Omega_0 + 1)} + i r_{x,y}(\alpha\Omega + \mathbf{k}_{\Gamma} \cdot \mathbf{k}^{-1})} \quad (3.19)$$

where the term $r_{x,y} > 0$ is a phenomenological factor that takes into account the symmetry breaking of the system [60].

3.1.2 Theoretical prediction

The Equations (3.19) and (3.9) have an important implication for the propagation of the magnetostatic waves in presence of a temperature gradient, since it modifies the damping term, making it smaller or bigger, depending on the direction of the temperature gradient with respect to the direction of the wave vector.

Let's consider, as in the previous section, a YIG slab subjected to a temperature gradient, with magnetization waves traveling from one end to the opposite one. In a bulk YIG, as shown by Cunha [35], the magnetostatic modes of the magnetization waves are magnetostatic backward volume modes and propagate in the direction $-\mathbf{k}^{-1}$.

Equation (3.19) implies that if the magnetization waves propagate from the cold to the hot side are less attenuated than when they propagate in the opposite direction. This prediction is illustrated in Figure 3.1. The amount of damping is decreased when $\mathbf{k}_{\Gamma} \cdot \mathbf{k}^{-1} < 0$ and increased

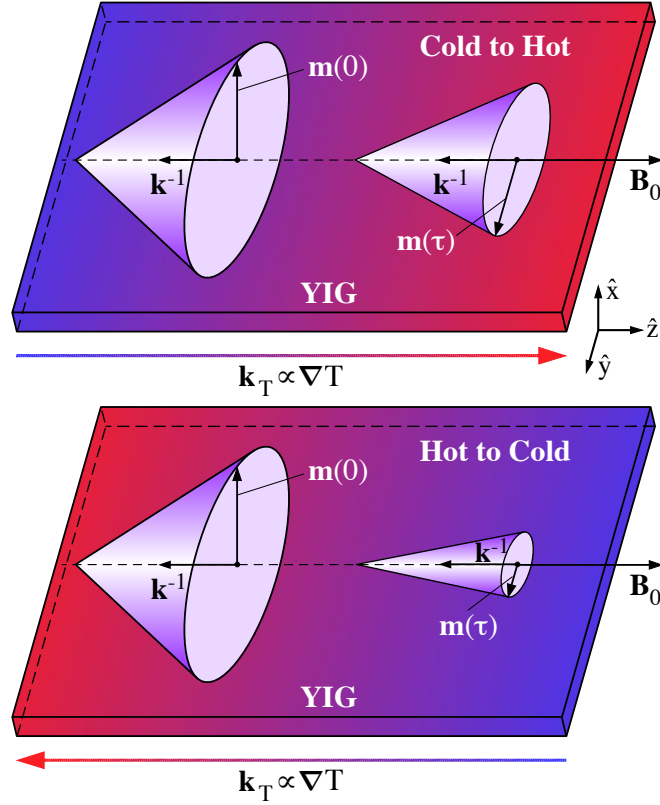


Figure 3.1: Illustration of the theoretical prediction for the magnetic Seebeck effect. Precession cones of the magnetization at the excitation $\mathbf{m}(0)$ and at the detection $\mathbf{m}(\tau)$ for magnetization waves propagating from the cold to the hot side (top) and from hot to cold side (bottom). The opening angle depends on the amount of damping given by the product $\mathbf{k}_T \cdot \mathbf{k}$ i.e. by the relative orientation of the magnetization waves propagation with respect to the temperature gradient. Image taken from [60].

when $\mathbf{k}_T \cdot \mathbf{k}^{-1} > 0$. This means that the precession cone of the magnetization \mathbf{m} , at the opposite side of the magnetization wave excitation, has an opening angle that is larger for magnetization waves propagating in the same direction of the temperature gradient and it is narrower for wave propagating in the opposite one.

3.2 Experimental setup

To verify the theoretical prediction described in the previous section we used the experimental setup illustrated in the schematics of Figure 3.2.

A thin slab of (011) single crystal YIG (from Ferrisphere), 10 mm long, 2 mm wide and 25 μm thick is placed on top of two Peltier elements used to generate a temperature gradient. The two modules sit on a common copper mass for heat dissipation and a specific thermal sticker is placed between them and the sample to ensure a good thermal contact. With this system

we can create a temperature gradient of the order of 20 K/cm and we are able to change its direction by changing the polarity of the two modules. The presence of the temperature gradient in the YIG sample is verified using an IR camera (see Section 2.2.1)

In this experiment two local probes are used to carry out transmission measurements along the YIG slab. The antennae are placed 8 mm apart and 500 μm over the surface of the sample. One probe is used to excite with microwaves pulses of 4.36 GHz in frequency and of 15 ns in duration. The pulses are created by mixing the signal generated by the microwave source with a pulse generator. The second probe is used for the detection and it is connected to an amplifier in series with a zero bias Schottky detector that provides an output signal proportional to the power of the microwaves. A digital oscilloscope is then used to observe the time evolution of the signal and thus to record the measurements presented in next Section. As for the other experimental methods described before, the external magnetic field is applied by means of an electromagnet driven by a power supply and controlled via Labview program.

3.3 Experimental results and discussion

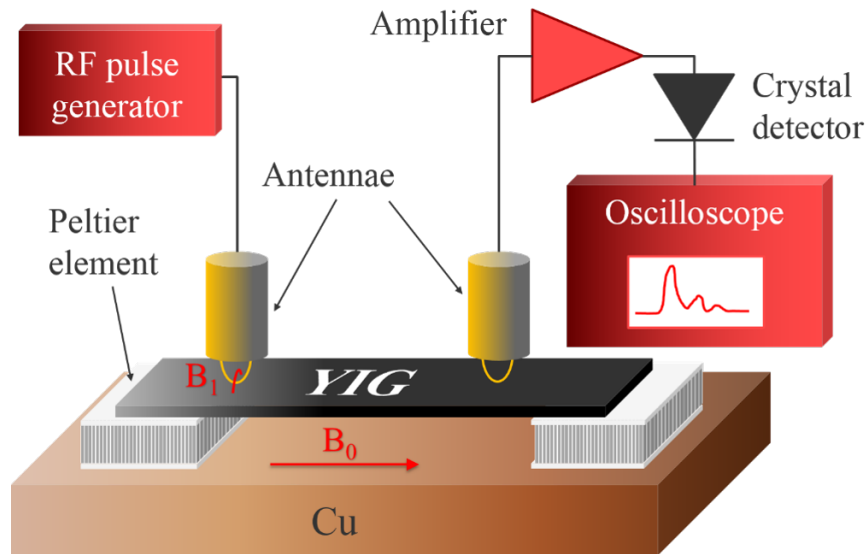
In this section we report and discuss time-resolved transmission measurements obtained with the experimental setup described before.

The transmitted signal for waves propagating from the cold to the hot side and from the hot to the cold side as a function of the applied magnetic field \mathbf{B}_0 is shown in Figure 3.3. We can clearly notice that when the waves propagate in the direction of the thermal gradient, they decay less rapidly than when they go in the opposite direction. This result confirms the theoretical prediction made in Section 3.1.2 and it gives an evidence for the magnetic Seebeck effect. At negative time ($t < 0$), we observe the presence of a small signal caused by the mixer leakage. However, this contribution is smaller than signal detected after the pulse and it accounts only for about the 3%.

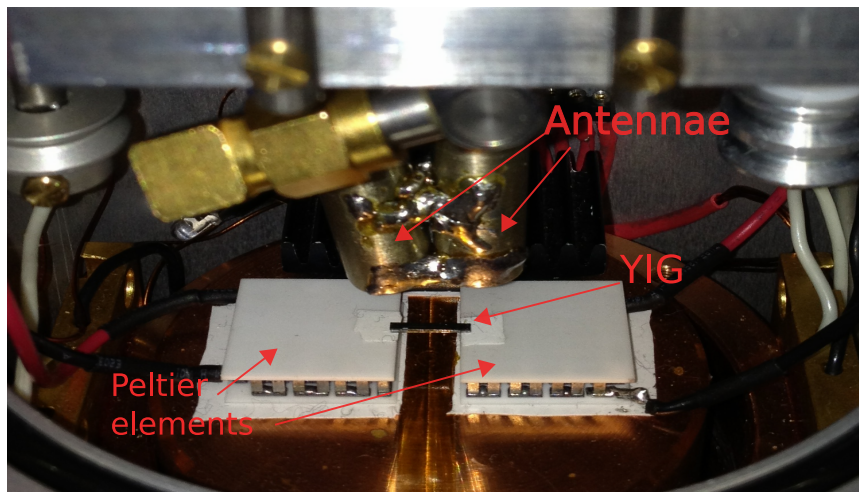
The difference in the signal attenuation is confirmed by Figure 3.4 and Figure 3.5. The first one shows the transmitted signal, in logarithmic scale, averaged over the range of the magnetic field. After the initial pulse of 15 ns, we observe a convolution of k_z modes propagating at different groups velocities and we notice that the attenuation is larger in correspondence to small k_z modes. This is in agreement with our theory as the effect, predicted in Equation (3.19), is proportional to k_z^{-1} . In Figure 3.5 we report the FMR spectrum at 70 ns after the microwave pulse. The spectral linewidth is approximately $\simeq 0.2$ mT. This value is larger than the homogeneous linewidth $\simeq \alpha B_{eff}$ [44] and for this reason we assume they correspond to inhomogeneous broadening.

From Figure 3.4 we can estimate the parameter λ which defines the magnitude of the magnetic Seebeck field \mathbf{B}_{ind} . According to Equation (3.19), the thermal effect adds a contribution to the loss term α of the LLG equation which is equal to

$$\alpha' = \frac{\omega_M}{\omega} \mathbf{k}_T \cdot \mathbf{k}^{-1} \quad (3.20)$$



(a)



(b)

Figure 3.2: Time-resolved transmission measurements setup. Schematic illustration (a) and photo (b) of the experimental setup. Magnetization waves are launched from one side and detected inductively at the other end by means of two local probes. Microwaves pulses are excited at a frequency of 4.36 GHz and have a duration of 15 ns. The YIG slab sits on top of two Peltier elements used to generate a temperature gradient across the sample.

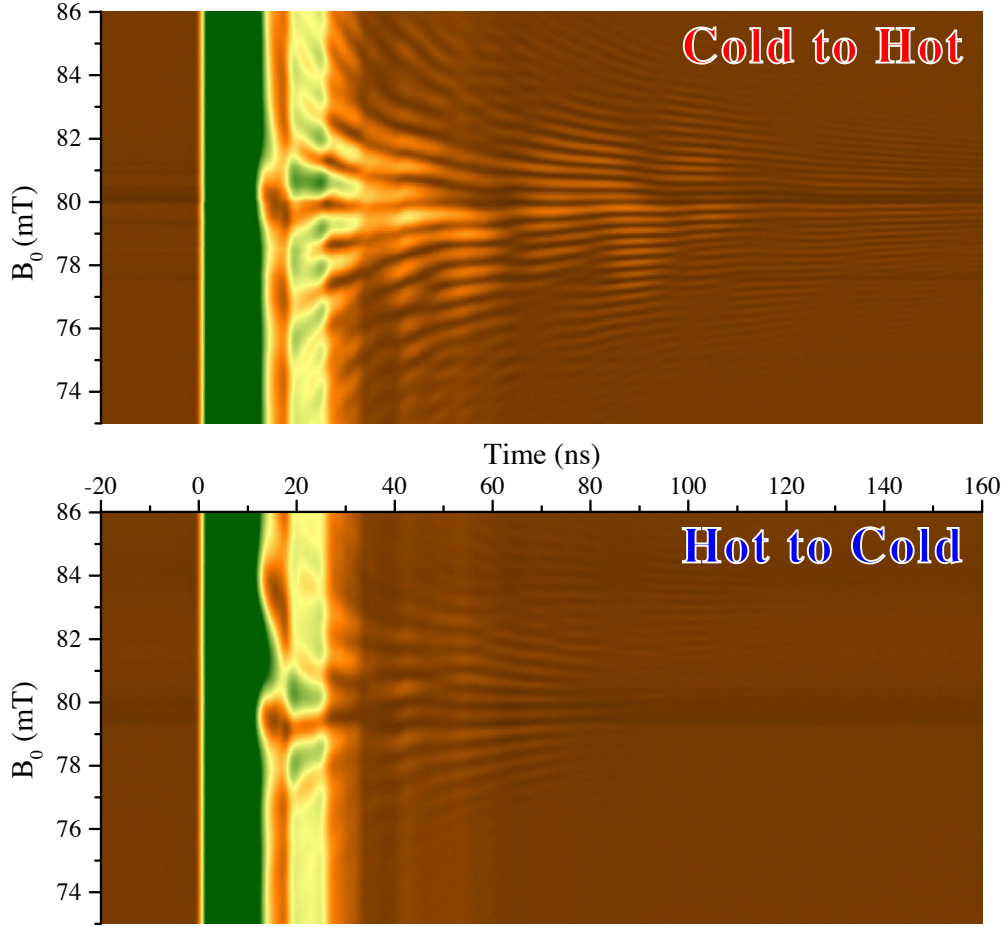


Figure 3.3: Time-resolved transmitted signal for a slab of YIG subjected to a temperature gradient. The signal is transmitted from the cold to hot side (top) and from the hot to the cold side (bottom) for different values of applied magnetic field (y-axis). The lighter area in the top graph shows that waves propagating in direction of the temperature gradient are less attenuated than when they propagate in the opposite direction. Image taken from [60].

where $\omega = \gamma|\mathbf{B}_0|$ is the pulsation at resonance in the applied field \mathbf{B}_0 and $\omega_M = \gamma\mu_0 M_s$.

By defining L as the length of the sample across which a temperature difference ΔT was established, we have $|\mathbf{k}^{-1}| \sim L/\pi$ and $|\nabla T| = \Delta T/L$. If we take the expression of the thermal vector \mathbf{k}_T , given by Equation (3.9)

$$|\mathbf{k}_T| = \frac{\lambda n k_B}{\mu_0 M_s^2} |\nabla T| \quad (3.21)$$

and we replace it in Equation (3.20), we find that the effect of the temperature gradient on the damping, adds the contribution:

$$\alpha' = \frac{\lambda n k_B \Delta T}{\pi M_s B_0} \quad (3.22)$$

3.3. Experimental results and discussion

We estimate that a reversal of the temperature gradient along the sample, implies a change in the damping by a factor of 3. This means that $(\alpha + \alpha')/(\alpha - \alpha') = 3$, which yields $\alpha' = \alpha/2$.

In the experimental system, we have the following conditions:

$$B_0 \sim 0.081 \text{ Tesla} \quad (3.23)$$

$$M_s \sim 1.5 \cdot 10^5 \text{ Am}^{-1} \quad (3.24)$$

$$\Delta T = 20 \text{ K} \quad (k_B = 1.3 \cdot 10^{-23} \text{ JK}^{-1}) \quad (3.25)$$

$$n \sim 1.1 \cdot 10^{28} \text{ m}^{-3} \quad (3.26)$$

From these values and from the relation (3.22) we get $\lambda \sim 0.01\alpha'$ and we find that λ for YIG is of the order of

$$\lambda_{\text{YIG}} \approx 10^{-6}. \quad (3.27)$$

According to the expression for the magnetic susceptibility, if the temperature gradient is big enough so that $\mathbf{k}_T \cdot \mathbf{k}^{-1} > \alpha\Omega$, this results in a negative damping causing the self-oscillation of the magnetization. With this value of λ we find a thermal damping ratio $|\mathbf{k}_T \cdot \mathbf{k}^{-1}|/\alpha\Omega = 0.3$ that is smaller than the self-oscillation threshold.

Report of a very similar experiment was published the same year as our Phys. Rev. Lett. by Cunha *et al.* in ref. [35] on the control of the relaxation of propagating spin waves in YIG films under the application of the temperature gradient. In their case the thermal gradient is applied orthogonally to the YIG film in longitudinal spins Seebeck configuration [65]. These authors show that ∇T affects the relaxation rate of the propagating waves only when a platinum layer is deposited on top of the sample. This is explained by the spin injection and the spin pumping effects at YIG/Pt interface [36, 30]. In absence of platinum, the effect does not occur. This is in line with our theory as in such configuration we have $\mathbf{k}_T \cdot \mathbf{k}^{-1} = 0$ and therefore the amount of damping does not change.

Another important point of discussion is the temperature dependence of the saturation magnetization. As pointed out by Orby *et al.* in ref. [26], it can affect the amplitude of the magnetization waves (see Section 1.1.3). We have to clarify that in our experiment, since we are close to a self-oscillation condition, the effect of the contribution $\mathbf{k}_T \cdot \mathbf{k}^{-1}$ is expected to be larger than the contribution due to the change in temperature of the saturation magnetization. Nevertheless, in contrast with the claim made in ref. [26], we show in Figure 3.3 that magnetization waves can travel in presence of the temperature gradient and can also propagate against it.

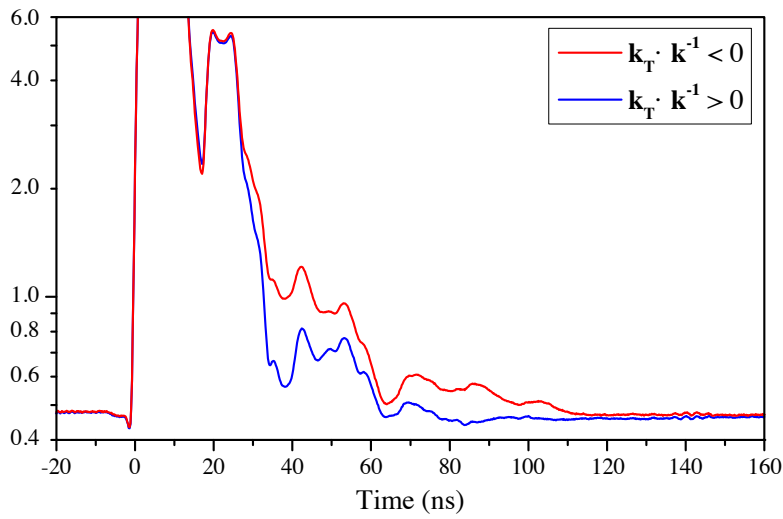


Figure 3.4: Transmitted signal as a function of time, averaged over the applied magnetic field. After the 15 ns duration pulse, we observe a convolution of k_z modes propagating at different group velocities. The signal amplitude is plotted in logarithmic scale and arbitrary units. Image taken from [60].

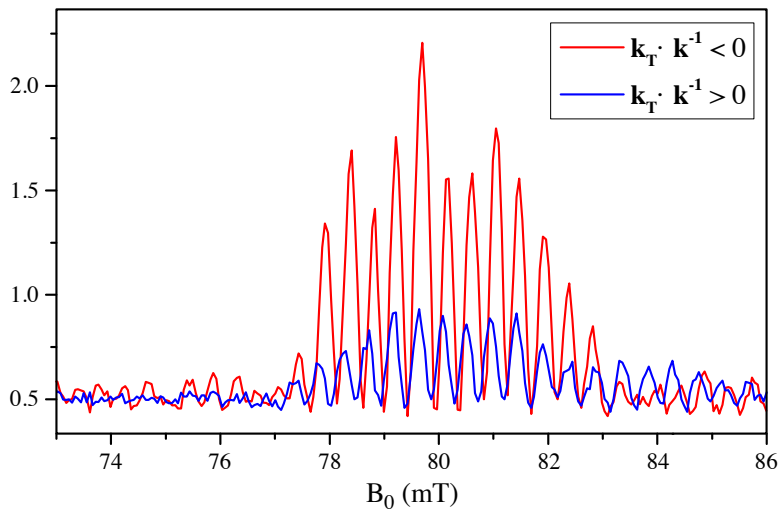


Figure 3.5: FMR spectra of a 15 ns pulsed excitation detected after 70 ns. FMR signal in arbitrary units and after baseline correction. Image taken from [60].

3.4 Conclusion

In this chapter we investigated the effect of a heat current on the dynamics of magnetization waves propagating in a magnetic insulator. Starting from the formalism that describes the irreversible thermodynamics for a continuous medium, we predicted a new effect that can be described as a magnetic field induced by a thermal gradient. We suggest to refer to it as magnetic Seebeck effect by analogy to the well known Seebeck effect (MSE). It should not be confused with the magneto-Seebeck effect [66] as this consists in a change of the Seebeck coefficient depending on the magnetic configuration. By carry out transmission measurements in a thin slab of YIG, we found evidence for this effect by showing how the MSE can modulate the magnetic damping depending on the direction of the propagating magnetostatic modes with respect to the orientation of the temperature gradient.

4 Magnetization dynamics of ferro-magnetic insulators subjected to a temperature gradient

In this chapter we briefly report additional attempts aimed at getting further evidence of the magnetic Seebeck effect presented in the previous chapter. In Section 4.1 we report FMR studies of YIG disks subjected to a temperature gradient, while in Section 4.2 we discuss experiments conducted on YIG slab.

4.1 YIG disks subjected to a temperature gradient

The magnetization dynamics of YIG disks has been extensively studied in the past using both continuous wave [67, 68] and pulsed techniques [69, 70]. As for the case of a YIG slab (Section 1.2.3), the magnetostatic modes in a flat disk are characterized by a complete discrete spectrum of energy levels. The spatial distribution of such modes has been recently observed by Edward *et al.* using a magneto-optical Faraday-microscopy [71]. Numerical simulations on quasi 2D disks [72, 73] showed that disks could exhibit vortex states. According to the theoretical formalism described in Section 3.1, magnetic vortices should be favourable states for the thermally induced magnetic field. Hence, the general idea is to probe this vortex state and determine whether a thermal gradient affects this state.

4.1.1 Resonant cavity experiment

We conducted FMR experiment on 3 mm diameter and 120 μm thick disks of single crystal YIG. The sample was squeezed between two Peltier elements used to generate the temperature gradient and placed inside a resonant cavity. The measurements were performed using the experimental setup described in Section 2.1.

In Figure 4.1 we show a comparison between a spectrum of a normally magnetized YIG disk with the spectrum of the same sample subjected to a temperature gradient, perpendicular to the plane and parallel to the external magnetic field. When the gradient is applied, we observe a compression of the spectrum and a shift to lower field caused by the temperature dependence of the saturation magnetization. Furthermore, we notice the excitation of additional resonance

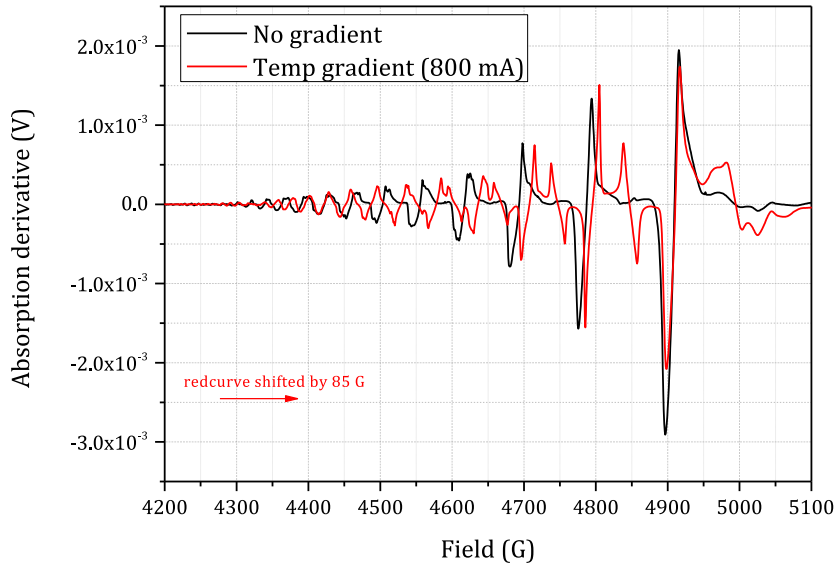


Figure 4.1: FMR spectra of a normally magnetized 120 μm thick disk of YIG as a function of the magnetic field. The measurements are carried out using a X-band resonant cavity at 9.47 GHz with a microwave power of 16 dBm. The value in mA reported in the legend corresponds to the current sent to the Peltier elements.

modes that do not appear in absence of the temperature gradient. Data reported in Figure 4.2, recorded with the same setup on a different sample, show the dependence of these modes on the intensity of the thermal gradient. The presence of the azimuthal in absence of temperature gradient is attributed to a small misalignment of the disk with respect to the applied magnetic field.

The FMR spectrum of anormally magnetized disk exhibits two types of resonance modes, namely *radial* and *azimuthal*, and we identify the modes caused by the thermal gradient with the latter type. The azimuthal modes appear only when the symmetry of the system is broken. It has been shown by Kamenetskii *et al.* [74] that inside a rectangular waveguide the excitation of the azimuthal modes depends on a combination of the electric and magnetic field: the maximum occurs at the point where the RF electric field is at the maximum and the magnetic field is at minimum. Therefore, we need to determine if the occurrence of the extra modes under a temperature gradient is due to the heat current or to the spurious effect due to a change in the electromagnetic field at the location of the sample.

4.1.2 WR-90 resonator

The following experiment convinced us that the extra modes reported in Figure 4.1 and 4.2 are caused by a spurious effect. Here, we replaced the resonant cavity with an home-made resonator designed using a conventional WR-90 rectangular waveguide. One side of the

4.1. YIG disks subjected to a temperature gradient

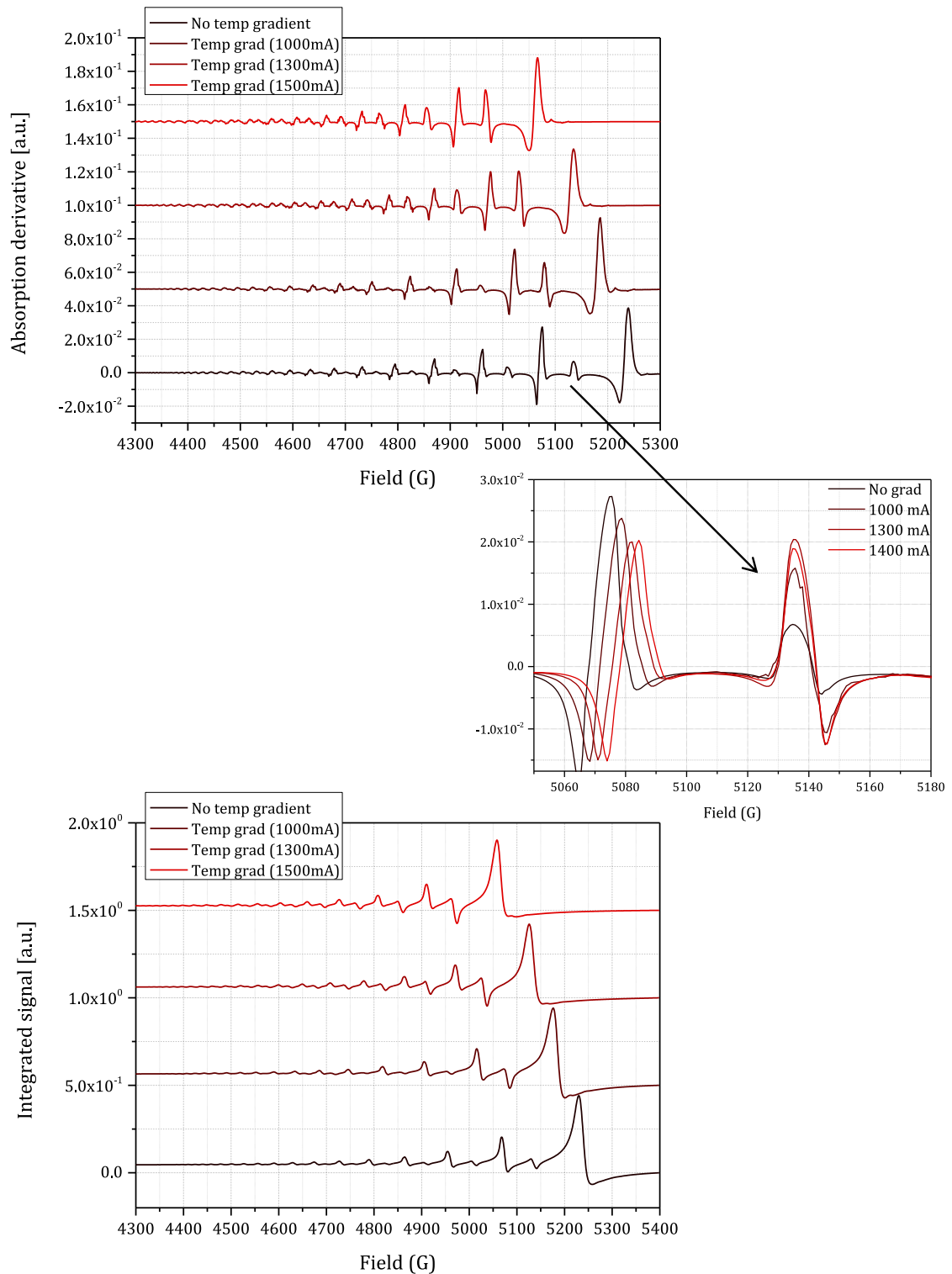
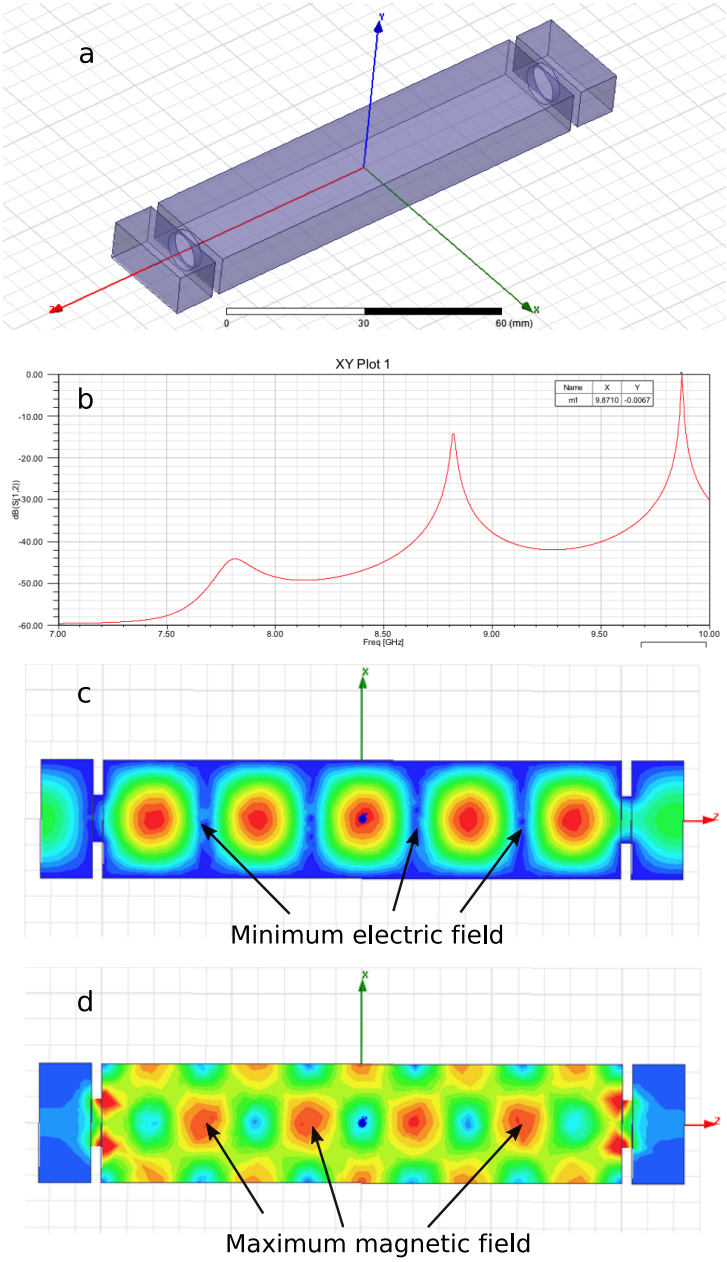


Figure 4.2: FMR spectra of a normally magnetized 130 μm thick disk of YIG as a function of the magnetic field. Absorption derivative (top) and integrated signal (bottom). The measurements are carried out as for Figure 4.1. The curves are shifted for clarity along the vertical scale in the top and bottom graph, and along the horizontal scale in the middle graph.

Chapter 4. Magnetization dynamics of ferromagnetic insulators subjected to a temperature gradient



6

Figure 4.3: Electromagnetic simulations of the WR-90 waveguide resonator. Geometrical design (a), simulations of the transmission coefficient (b), and spatial distribution of the electric (c) and magnetic field (d) inside the resonator.

waveguide was closed with a brass plate, while at the other end we put a copper sheet with a hole in the center for the iris. The simulations reported in Figure 4.3 show the distribution of the magnetic and electric field inside such a resonator for a microwave frequency of 9.871 GHz.

This experiment was conducted on a 3 mm in diameter and 500 μm thick disk of YIG. The sample was placed with its normal to the plane parallel to the z-axis (Figure 4.3a) and at the short end of a rectangular waveguide where we have the minimum of the electric field and the maximum of magnetic field. According to ref. [74] this position should promote the radial modes and hinder the excitation of azimuthal one. In this case the temperature gradient was applied as before, but in such a way to avoid the heating of the sample. We estimated $\Delta T_{max} = 30$ K. To avoid strong coupling between sample and resonator, we decided to conduct our experiment at 7.5 GHz, far from the resonance frequency of the waveguide. FMR spectra obtained with this experiment are reported in Figure 4.4. We noticed that the resulting spectrum was identical to the one measured without the application of the thermal gradient. Since this is in contrast with the results observed previously we cannot conclude that a temperature gradient can induce the excitation of the azimuthal modes.

Nevertheless, it is still not clear the reason why we observed such effect with the usual cavity since it is designed also to minimize the electric field at the location of the sample. A possible explanation could be attributed to the different sample thicknesses. As the disk used for the resonant cavity experiment broke, it was impossible to use the same sample for this measurement. Another reason could be related to strong coupling between resonant cavity and YIG disk. Since the resonance frequency of the sample depends on the saturation magnetization and thus on temperature, the heating up of the disk would influence the coupling between YIG disk and sample and cavity.

4.2 Thermally induced self-oscillation

As discussed in the previous chapter, the magnetic Seebeck effect can increase or decrease the damping depending on the orientation of the magnetostatic wave vector with respect to the temperature gradient. If the negative damping is large enough so that $\mathbf{k}_T \cdot \mathbf{k} > \alpha\Omega$, then the overall damping would be negative and the magnetization would undergo self-oscillation. Following this prediction, part of the research work has been dedicated to the attempt of inducing a magnetization oscillation by applying a constant heat current. We conducted noise measurements on a slab of YIG placed in the same configuration as for the magnetic Seebeck effect (Section 3.2). The signal recorded with a probe resonator was first amplified and then sent to an Agilent spectrum analyzer (working range 9 kHz - 26.5 GHz). We observed a few times what seemed to be an emission from the sample over a very broad frequency range. Nevertheless, we were not able to reproduce these results and for this reason we decided not to report actual experimental data in this thesis.

Chapter 4. Magnetization dynamics of ferromagnetic insulators subjected to a temperature gradient

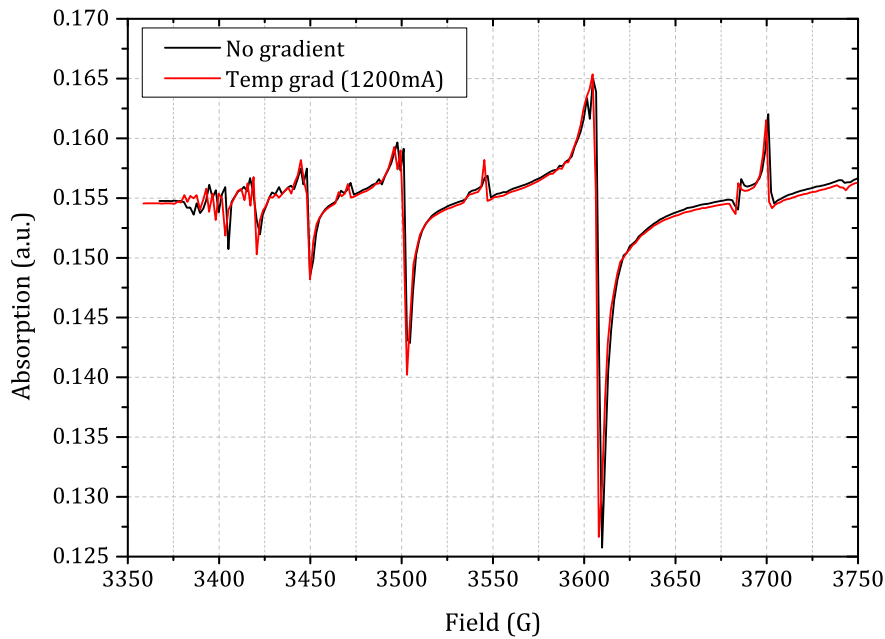


Figure 4.4: FMR spectra of a normally magnetized 500 μm thick disk of YIG as a function of the magnetic field. The measurements are carried out at 7.5 GHz with a microwave power of 16 dBm. The value in mA reported in the legend corresponds to the current sent to the Peltier elements.

4.3 Conclusions

Following the prediction for a self-oscillation induced by pure temperature gradient, we exploited several noise measurement techniques, both at room and low temperature, but until now we did not succeed to observe this effect. Also, we conducted FMR studies on YIG disk using two different resonance schemes. Although we observed the excitation of azimuthal modes in presence of a temperature gradient, we were not able to reproduce this effect when changing the configuration of the sample and the detection scheme.

5 Spin Dynamics in Magnetic Nanostructures

In the previous chapters we focused our attention on magnetic insulators. The work presented in the second part of this thesis is instead aimed at investigating metallic nanostructures when subjected to a heat current. As mentioned in Section 1.1.1, the 3-current model predicts that a heat current can produce a spin current in the volume of a magnetic layer, and consequently, it is expected to produce a spin torque in a spin valve. Hence, we explore what has been called Thermal Spin Torque (see Section 5.1.3) in electrodeposited Co/Cu/Co asymmetric spin valves grown in the middle of copper nanowires.

In this chapter we present ferromagnetic resonance studies of metallic spin valves in presence of a temperature gradient. First in Section 5.1, we provide a basic theoretical background, essential for a complete understanding of the spin dependent phenomena occurring in these nanostructures. Then, in Section 5.2, we illustrate the procedure for sample fabrication, contacting and characterization. Section 5.3 describes the experimental setup and techniques employed. Finally, Section 5.4 concludes the chapter with the presentation and discussion of the experimental results.

5.1 Spin-dependent transport and dynamics

5.1.1 Giant Magneto Resistance

The *giant magnetoresistance* (GMR) effect was discovered in the late 1980s [76, 77] by observing large magnetoresistive variations in magnetic nanostructures containing ferromagnetic films separated by metallic spacers.

A spin valve, in its simplest form, is a system composed by two ferromagnetic (FM) layers separated by a non magnetic spacer (NM). One is typically pinned (reference layer), while the other can switch its magnetization (free layer). When the two magnetic layers have their magnetization in a parallel configuration, the spin-up electrons (spin anti-parallel to the magnetization), passing thorough the trilayer, encounter almost no scattering (low resistance). On the contrary, in the antiparallel state, both spin-up and spin-down electrons are equally

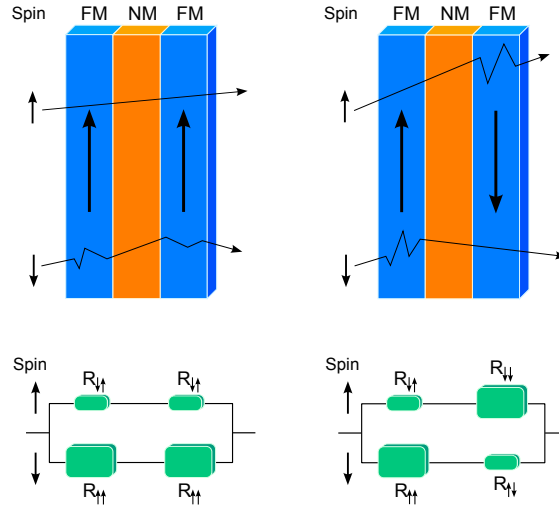


Figure 5.1: Illustration of the Giant Magnetoresistance effect. Top: representation of a spin-valve composed by a non magnetic layer sandwiched between two ferromagnetic layers. Electrons are scattered differently depending on their spin orientation with respect to the configuration of the magnetic layers. Bottom: equivalent circuit diagram of the GMR effect. Figure adapted from [75].

scattered (high resistance). A schematic illustration of this effect is reported in Figure 5.1. In a spin valve system, the GMR ratio is defined as:

$$MR = \frac{R_{AP} - R_P}{R_P} \quad (5.1)$$

with R_{AP} and R_P being the resistances of the antiparallel and parallel state, respectively. We can express the GMR angular dependence as:

$$R = R_P + \Delta R \left(1 - \cos^2 \left(\frac{\theta}{2} \right) \right) \quad (5.2)$$

where θ is the angle between the magnetization of the two FM layers, and $\Delta R = R_{AP} - R_P$ is the difference between the resistances at the antiparallel and parallel state.

A magnetic tunnel junction (MTJ) is a system very similar to a GMR spin valve. In a MTJ the non magnetic spacer is replaced by an insulating layer, typically aluminium oxide or magnesium oxide. This oxide layer is so thin that electrons can tunnel through the barrier when a bias voltage is applied between the two metal electrodes. This phenomenon is called tunneling magnetoresistance (TMR) [78] and it presents a MR ratio much larger than GMR. More details on this topic can be found in ref. [79] and in the references therein.

5.1.2 Spin Transfer Torque

Theoretically predicted in 1996 by Slonczewski [1] and Berger [2], and experimentally observed in 2000 [80], the *spin angular momentum transfer* or *spin-transfer torque* (STT) is a phenomenon that originates from the exchange of the angular momentum between a spin polarized current and the magnetization of a ferromagnetic layer [81, 82, 83, 84]. The STT effect provides a local means of magnetization manipulation and its discovery has represented the milestone for the development of a novel concept of magnetic memory: the STT-MRAM. In a GMR device, like the spin valve described in the previous Section, the current passing through the first ferromagnetic film (pinned layer) becomes spin polarized and mostly maintains this polarization through the nonmagnetic spacer. When it enters and interacts with the second ferromagnet (free layer), part of the angular momentum is transferred from the electron spins to the free layer, exerting a torque \mathbf{T}_{STT} on the magnetization vector \mathbf{M} . To take this phenomenon into account, the expression of the LLG equation for the magnetization of the free layer in the macrospin approximation becomes:

$$\frac{d\mathbf{M}}{dt} = -\gamma\mathbf{M} \times \mathbf{H} + \frac{\alpha}{M_s}\mathbf{M} \times \frac{d\mathbf{M}}{dt} + \frac{d\mathbf{M}_{STT}}{dt} \quad (5.3)$$

where γ is the gyromagnetic ratio, α a phenomenological damping factor and \mathbf{M}_{STT} is the so called Slonczewski term. It determines the effect of spin transfer torque on the magnetization dynamics and is defined as:

$$\frac{d\mathbf{M}_{STT}}{dt} = -\frac{\gamma\hbar}{2eVM_s^2}\mathbf{M} \times (\mathbf{I}_s \times \mathbf{M}) \quad (5.4)$$

where e is the electron charge, V the volume of the ferromagnet, M_s the magnetization at the saturation and I_s the spin-polarized current [85].

More generally, as illustrated in Figure 5.2, the torque exerted by the incident electrons on the free layer, can be decomposed in two directions: one in the plane of the magnetization (red arrow) and the other perpendicular to it (blue arrow). The latter is called field-like torque and since it is very small it is usually neglected in spin valve systems [83].

The STT effect can either act with the damping torque or against it depending on the polarization of the current. In the first case it gives rises to an additional damping and the magnetic moment aligns "faster" with the applied field. In the second case, when the current is polarized in such a way that the spin torque is antiparallel to the magnetic damping, different situations may occur depending on the STT magnitude, i.e. on the intensity of the current density J . If J exceeds the value of the critical current density J_C , the magnetic damping becomes negative

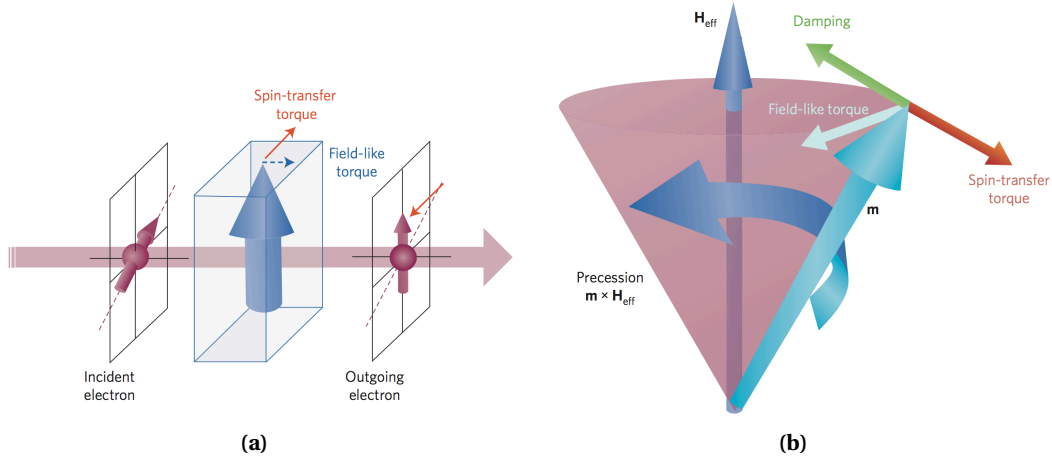


Figure 5.2: Illustration of the spin transfer torque effect. (a) Current-induced torque caused by the interaction between incident electrons and magnetization: the difference in spin polarization causes a torque in the plane of the magnetization and a torque perpendicular to this plane (field-like torque). (b) Illustration of LLG dynamics in presence of the spin torque: the STT (red arrow) acts against the damping bringing the magnetization out of equilibrium. Figures taken and adapted from [85].

and the magnetization of the free layer spirals away from the fixed layer until a steady state is reached. In this case we have a stable precession of the magnetic moment around the applied field. The critical current density is defined as [1, 86, 87]:

$$J_C = \left(\frac{2e}{\hbar}\right) \left(\frac{\alpha}{\eta}\right) M_s t_F (H + H_k + 2\pi M_s) \quad (5.5)$$

where η^1 is the spin-polarization factor, t_F the thickness of the ferromagnetic free layer, H the external applied magnetic field, and H_k is the effective anisotropy field.

A further increase of the current density leads to an increase of the precession angle and when this is higher than a critical value, it causes the complete reverse of the magnetization orientation of the free layer.

As we will see in the next sections the STT effect is a powerful tool to probe and excite ferromagnetic resonance in magnetic nanostructures.

¹ $\eta = (I_{\uparrow} - I_{\downarrow}) / (I_{\uparrow} + I_{\downarrow})$, where I_{\uparrow} and I_{\downarrow} are the majority and minority spin-polarized currents with their polarization axis defined by the polarizing layer

Spin Transfer Torque-driven Ferromagnetic Resonance

As described earlier, the spin transfer torque depends linearly on the applied current density J passing through the magnetic layers. In a simple spin valve, like the one described in section 5.1.1, a change in the current polarity results in a change in the torque direction. Therefore, when an AC current is applied, it generates an oscillating STT torque and if the AC frequency matches the natural frequency of magnetization precession, it drives the free layer magnetic moment into resonance. At the resonance frequency, the STT compensates the damping losses and continuously puts the magnetic moment out of equilibrium, acting in synchronization with the magnetization oscillation.

This methods for exciting the ferromagnetic resonance, in combination with magnetoresistance based electrical detection techniques (e.g. GMR or TMR), can be exploited to study the magnetization dynamics of nanoscaled devices [88]. The spin transfer torque-driven FMR (STT-FMR) has been widely used for FMR studies in a large variety of samples, from magnetic tunnel junctions [89, 90, 91, 92] to metallic nanopillars [93, 94] or electrodeposited nanowires [95, 96]. It allows to probe the FMR in samples with only a million of Bohr magnetons. This is not possible by using standard methods with resonant microwave cavities because of the small dimensions of the samples.

When a microwave current $I(t) = I_{rf} \cos(\omega t)$ is sent to a magnetoresistive system like a spin valve, at a frequency corresponding to the FMR frequency, the oscillating STT induces a precession of the magnetic moment. Because of the continuous reorientation of one layer with respect to the other, the magnetoresistance is time dependent and has the form:

$$R(t) = \Delta R \cos(\omega t + \delta). \quad (5.6)$$

It should be considered that in nanowires, a high current density is reached for very small currents. The currents are so small that the Oersted field they induce has a much smaller effect compared the STT. The voltage $V(t)$ resulting from the product $I(t)R(t)$ contains two equal amplitude components, one at zero frequency V_{DC} and the other at the second harmonic $V_{2\omega}$ [97]. In the simplest form the dc term is given by the equation [98, 88]:

$$V_{DC} = \frac{1}{2} I_{rf} \Delta R \cos \delta \quad (5.7)$$

It occurs only at resonance and when we are in presence of a noncollinear configuration of the two magnetic moments, i.e. when the two layers present a relative angle that is not equal to zero.

This method allows us to detect the FMR in the nanomagnetic device by measuring this voltage across it. STT-FMR experiments on electrodeposited asymmetric spin valves will be presented and discussed in Section 5.4 along with an illustration of the experimental setup in Section 5.3.

5.1.3 Thermal spin-transfer torque

The *thermal spin-transfer torque* or *thermal spin torque* (TST) is a physical phenomenon consisting in the manipulation of the magnetization by the application of a heat flow. This effect is analogous to the STT described in Section 5.1.2, with the main difference that the torque is driven by a heat current rather than a charge current.

The idea that a heat flow can induce a spin current in a magnetic nanostructure was predicted using circuit theory by Hatami *et al.* in 2007 [99]. Theoretical predictions of TST acting on magnetic domain walls [100] and magnetic tunnel junctions [101, 102] were also proposed, as well as the idea, suggested by Slonczewski, to use a magnetic insulator as polarizer to induce a thermal spin torque in a spin valve system [103]. Using a three-current model (heat, spin-up and spin-down), Bréchet and Ansermet pointed out that a standard three-current model [13] predicts the existence of a spin polarization current on large scales, that is proportional to the temperature gradient.

The first evidence for a heat-driven spin torque was observed by this group in ref. [104]. Haiming Yu *et al.* demonstrated how a heat current can shift the switching field of metallic spin valves. Experimental evidence for the generation and injection of a spin current by a heat current was demonstrated by using metallic ferromagnetic nanostructures [14], STM tips [105] or magnetic tunnel junction [106]. More recently, clear evidence for a heat-driven spin torque has been obtained by monitoring the magnetization dynamics after an ultrashort (0.1 ps) pulse used to thermally drive the demagnetization of a ferromagnet [107]. In ref. [14] Slachter *et al.* argued that a thermal spin injection, at the interface between the ferromagnet and the metallic spacer, can be as efficient as a charge-driven spin injection.

Further experimental evidence of this effect is reported in Chapter 6 by observing the linear response of a heat-driven spin torque in electrodeposited Co/Cu/Co spin valves.

5.2 Samples preparation, fabrication and characterization

The samples used for the experiments presented in this chapter consist of asymmetric spin valves grown in the middle of copper nanowires. As illustrated in Figure 5.3, these magnetic nanostructures are composed of a copper layer (non magnetic spacer) sandwiched between two layers of cobalt, one thicker and one thinner, acting as reference and free layer respectively. The samples are grown by a standard electrodeposition process in commercial ion-track-etched polycarbonate membranes. The membrane is 5 μm thick and contains nanopores of 30 nm diameter with a pore density of $6 \times 10^6/\text{cm}^2$. An original method for growing and contacting the nanowires, designed for high frequency measurements, has been developed by the group [96, 108, 109] and it is extensively described in ref. [109].

5.2. Samples preparation, fabrication and characterization

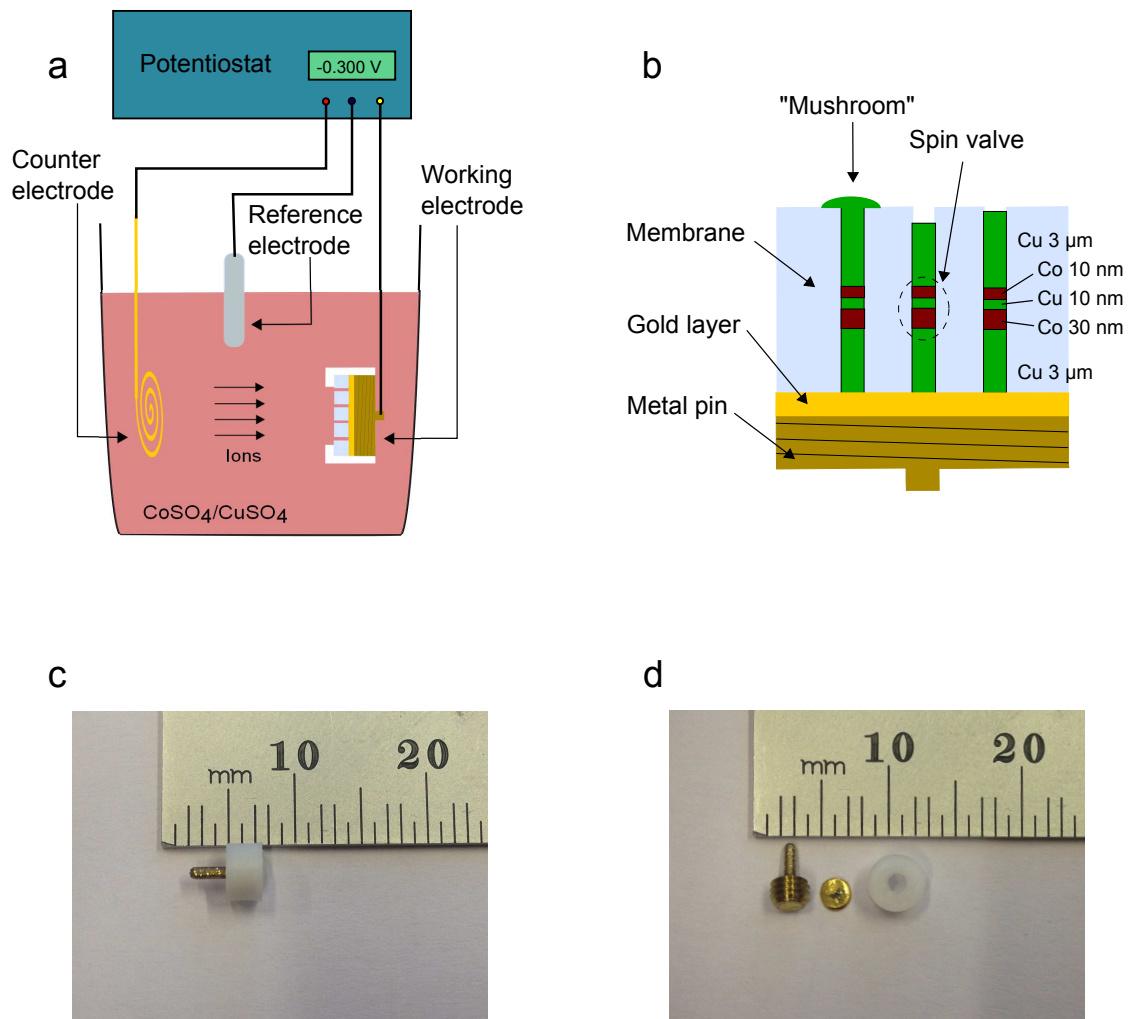


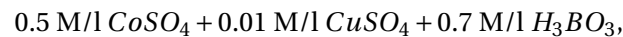
Figure 5.3: Nanowires fabrication process. (a) Schematic of the electrodeposition system: the gold layer, in contact with the metallic pin, is used as working electrode in order to force the ions to fill the porous membrane. (b) Details of the nanowire growth: spin valves are fabricated by alternating the deposition of Co and Cu layers. Once the pores are filled, the formation of metal bumps (mushroom shaped) occurs on top of the membrane and the electrodeposition is stopped. (c)(d) Photos illustrating the sample holder containing the membrane sputtered with gold, the teflon cup and the metal pin.

5.2.1 Electrochemical growth of metallic nanowires

The nanowires fabrication is carried out by means of a conventional electrodeposition technique. This includes an electrolyte that contains the metals to be deposited, and a standard three electrodes system (Figure 5.3) consisting of:

1. Working electrode: the cathode where the metal reduction occurs.
2. Counter electrode: the anode, responsible for the charge flow in the electrolyte.
3. Reference electrode: a saturated Ag/AgCl electrode that keeps the electrolyte at a constant voltage.

The first step is the deposition via sputtering of about 500 nm of gold layer on top of one side of the membrane. This gold plate is then put in contact with a metallic pin and encapsulated by a teflon cup screwed on top. The whole system, designed to fit in a SMA connector, is then immersed in a single bath composed of



and used as working electrode in the electrodeposition setup. The membrane so encapsulated serves as nanowires template and when an electrical potential is applied, the ions are forced to deposit into it.

During the deposition, the electrolyte is stabilized at a temperature of 37.5 °C for the whole duration of the process. Since the electrolyte contains both Co and Cu salts, we can selectively deposit one or the other by applying a voltage of $V_{Cu} = -0.3 \text{ V}$ and $V_{Co} = -0.1 \text{ V}$ respectively. Multilayers and spin valves can be grown using this technique. Nevertheless, it should be taken into account that even if the concentration of Cu is very small compared to the Co one, a 15% of Cu impurities are deposited in the Co layer.

To grow multilayers with a desired thickness it is important to proceed first with a calibration step. This consists in filling completely the polycarbonate membrane with one material at the time so that, by recording the amount of time needed to fill the pores, we can calculate the deposition rates. A typical electrodeposition curve of a Co 30nm / Cu 10nm / Co 10nm asymmetric spin valve embedded in Cu nanowires is reported in Figure 5.4. During the electroplating the deposition current is continuously monitored. A rapid increase indicates that the pores are completely filled and ions start to aggregate on top of the membrane surface, forming "mushrooms" shaped Cu bumps. At this point the electrodeposition is stopped and, after a drying step, the samples are ready for the characterization.

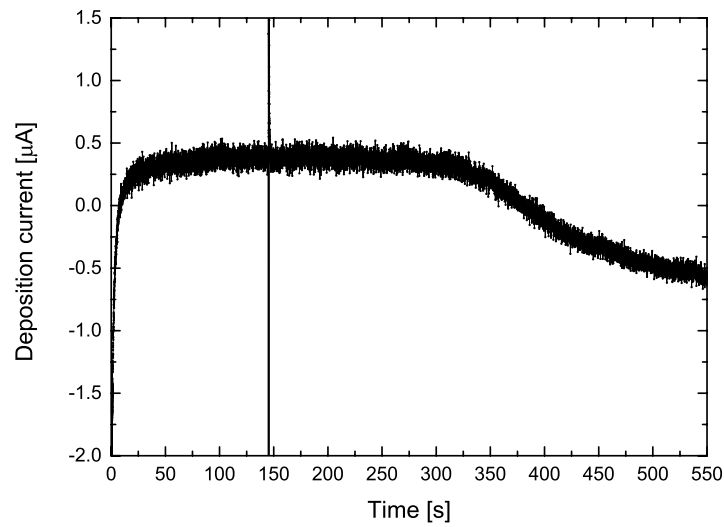


Figure 5.4: Typical deposition curve of a single Co 30nm / Cu 10nm / Co 10nm asymmetric spin valve embedded in Cu nanowire. Spikes appear when the electrical potential is switched from V_{Cu} to V_{Co} indicating the deposition of the Co layers. The rapid increase of the current at the end of the curve indicates that the membrane has been filled and that the metal bumps start to form.

5.2.2 Electrical contact and characterization

Once the fabrication process is completed, the filled membrane is placed into a female SMA connector, as shown in Figure 5.5(a). In this way, the bottom of the nanowires is connected through the gold layer/pin system, and an original method is employed for contacting the top side. The SMA connector, with the sample placed inside, is sealed by a metal cup connected to the SMA ground. This holds a metal screw with a gold wire of 25 μm in diameter soldered at the top. The electrical contact is made by approaching the membrane surface with the screw until the gold wire touches the metal bump of one nanowire. During this procedure, a small AC current is sent to the sample in order to monitor continuously its resistance and verify that the electrical contact is maintained. Since only very few pores are completely filled during the electrodeposition, we are able to electrically contact just one or maximum two nanowires at the time. Another advantage of this method is the possibility of studying other nanowires from the same template by just displacing the gold wire on another area of the membrane. Furthermore, since the metal cap presents an opening on one side (Figure 5.7 b), it is also possible to conduct optical characterizations of the samples (Section 5.4).

Once the electrical contact is established, we can perform GMR measurements to check the quality of the electrical connection and to verify that the magnetic nanostructure is working properly. Figure 5.6 shows the GMR curve of a single Co 30nm / Cu 10nm / Co 10nm asymmetric spin valve embedded in the middle on a Cu nanowire. The curve is recorded using a standard lock-in technique by sending a current of the order of 10 μA . The value of the current is kept small in order to minimize any contribution due to Joule heating. During the

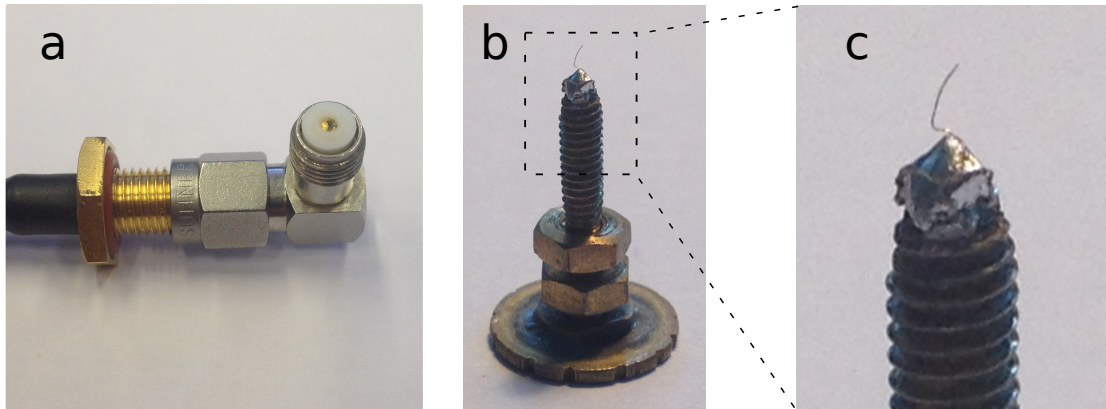


Figure 5.5: Illustration details of the sample contacting method. (a) Sample holder inside a female SMA connector. (b)(c) 25 μm gold wire soldered on top of a screw used to approach and contact the nanowires.

measurements, the magnetic field is applied perpendicular to the nanowire and parallel to the plane of the free layer. It is swept from negative to positive and positive to negative values and it reveals a switching field occurring at about $H_{sw} = 120$ mT with a MR ratio of about 0.27%. This is a good result if we consider that the typical value for a similar sample is about 0.1%. The MR ratio is of particular importance in the detection of the STT-FMR as it determines the sensitivity of the system.

5.3 Experimental setup for current induced STT-FMR

In Section 5.1.2 we discussed the possibility to exploit the STT effect for exciting the FMR in nanomagnetic devices and probe it using magnetoresistive effects.

Here we present the experimental setup based on this concept that we designed to conduct FMR studies of single Co/Cu/Co spin valves fabricated with the electrodeposition technique described in Section 5.2. Thanks to the original design of the sample holder that fits perfectly in a SMA connector, we are able to perform high frequency measurements in the GHz range. The FMR is detected electrically by measuring a dc voltage across the sample when the frequency of the spin-polarized current hits the FMR frequency. Since the free layer contains about 10^6 Bohr magnetons, the FMR could not be detected by regular X-band cavity-based methods. For this reason, the electrical detection is the only method that can be used to study the magnetization dynamics in these samples.

A schematic illustration of the experimental setup is reported in Figure 5.7. The rf current is generated by a Rohde & Schwarz microwave source and is injected into the nanowire. The sample is placed between the poles of an electromagnet used for the application of an external magnetic field. The rf power is typically -10 dBm and the frequency ranges from 2 to 12 GHz. A bias-T is used to select the only DC component of the resulting signal across the nanowire. By measuring the voltage at the DC output we can detect the FMR signal of our sample. Since

5.3. Experimental setup for current induced STT-FMR

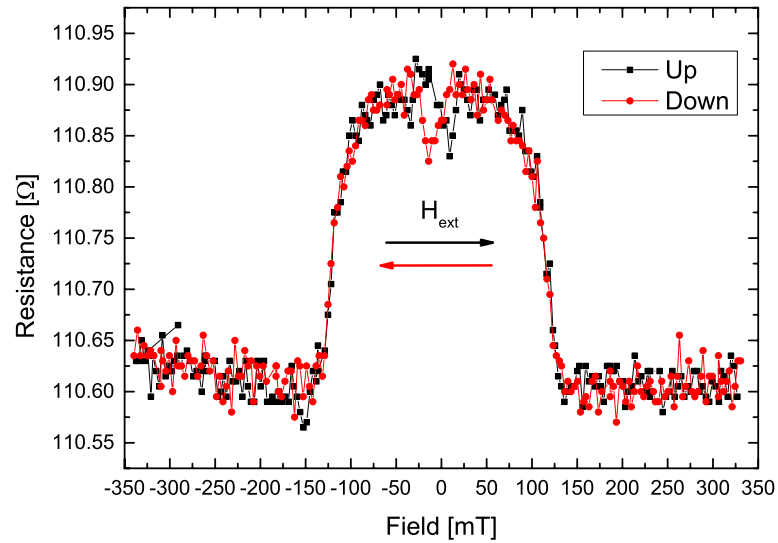


Figure 5.6: Giant magneto resistance of a Cu nanowire containing a Co 30nm / Cu 10nm / Co 10nm asymmetric spin valve. The applied magnetic field is perpendicular to the nanowire and parallel to the plane of the cobalt layers. The measurement is performed by sweeping the field from negative to positive and from positive to negative values.

the FMR depends on the applied magnetic field, a conventional field modulation technique with lock-in amplifier detection is employed to improve the sensitivity of the system. The two modulation coils are driven by a function generator and an AC field, with an amplitude of about 27 Oe peak to peak, is generated by a sinusoidal wave at a frequency of 37 Hz. The measurements are performed by scanning the frequency from 2 to 12 GHz at a constant applied magnetic field. The data are recorded with a Labview software that is also used to drive all the electronic equipment via GPIB interface.

5.3.1 Temperature gradient

In order to create a heat current flowing through the samples, a temperature gradient can be generated either by Joule heating, following the experiment of Yu [104], or by laser heating. In this work we exploit the latter solution as it avoids any contributions from the STT generated by a charge current. Experiments on thermoelectricity showed that temperature differences of a fraction of 1 K can be produced by laser heating between the ends of the nanowires [110]. Therefore, since the length of our nanowires is about 5 μm , we expect to generate a temperature gradient of the order of 10^4 K/cm.

Following this idea we implemented a laser diode (100 mW, wavelength of 640 nm) in the experimental setup. The light generated by the laser is collimated into an optical fiber and then shone on top of the sample. This is possible thanks to the opening on the metal cup sealed on top of the SMA connector, as illustrated in the photo of Figure 5.7. Depending on the laser power, we can create a difference in temperature of few K between the top and the

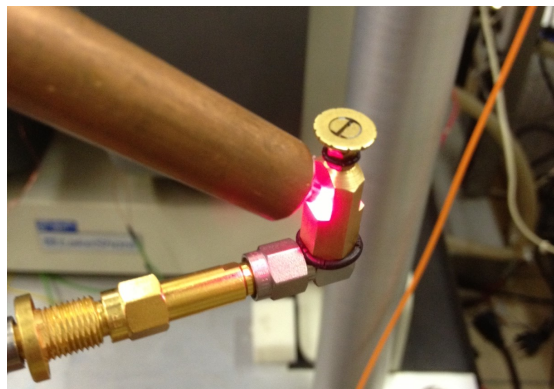
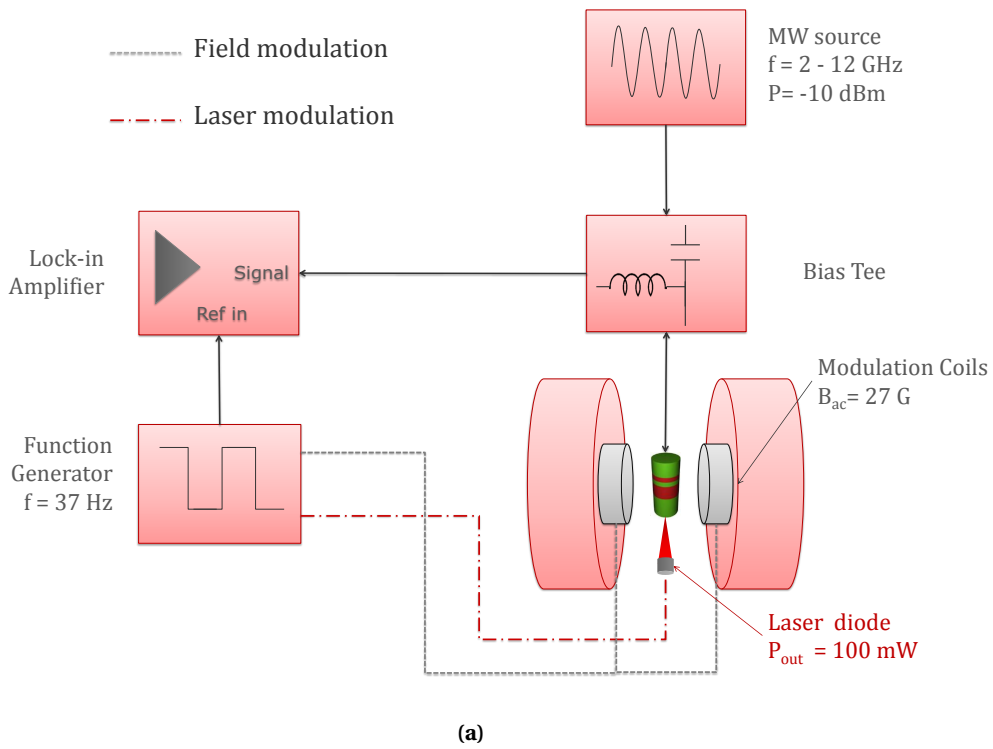


Figure 5.7: STT-FMR experimental setup with field and laser modulation (a) Schematic of the experimental setup implementing a lock-in technique with field and laser modulation. (b) Photo of the sample holder with laser heating.

bottom of the sample.

5.3.2 Laser modulated STT-FMR

A technique known as photothermally modulated ferromagnetic resonance (PM-FMR) has been previously used to investigate magnetostatic spin wave modes in thin films [111, 112, 113] and spheres [114] of YIG, and it has been even employed to investigate the magnetic anisotropy of thin epitaxial film of Fe and Co [115, 116]. This technique relies on a local thermal modulation, by laser heating, of the microwave absorption due to a change in the temperature-dependent magnetic parameters, such as saturation magnetization and anisotropy [117]. Depending on the magnitude of their temperature coefficients, the signal can be either smaller or larger than the conventional FMR signal.

A very similar concept is used in the setup illustrated in Figure 5.7. During this measurement, the modulation coils are switched off and the detection is locked at the frequency of the square wave sent to the laser diode to create light pulses. Thanks to this technique, only the variations due to the laser heating can be detected. Therefore, the obtained signal is proportional to the temperature derivative of the RF susceptibility imaginary part.

As for the field modulation technique, the FMR data are taken by sweeping the microwave frequency and applying a constant magnetic field.

5.4 Experimental results

In Figure 5.8 and Figure 5.9 we report the data acquired with the experimental setup described in Section 5.3. Both of them show the FMR spectra of the same 5 nm Co / 7 nm Cu / 25 nm Co asymmetric spin valve, recorded by means of two different lock-in techniques: field modulation (left graph) and laser modulation (right graph). The voltage across the nanowire is recorded as a function of the microwave frequency for several values of external magnetic field, applied perpendicular to the nanowire and parallel to the magnetic layers. Figure 5.8 shows the FMR spectra recorded for an external magnetic field H_{ext} lower than the GMR switching field H_{SW} , i.e. when the two FM layers are in parallel configuration. The spectra evolution for the antiparallel state ($H_{ext} > H_{SW}$) is instead reported in Figure 5.9. In both cases we can observe a clear field dependence of the resonance peaks. When a jump occurs in the GMR curve, i.e. when the spin valve passes from an antiparallel to a parallel configuration, the shift and thus the slope $\partial f / \partial H$ changes direction. This can be easily observed in the $f(H)$ diagram reported in Figure 5.10 and it is a further indication that we are probing the ferromagnetic resonance of the spin valve.

Our measurements are based on the detection of the oscillating magnetoresistance $R(t)$ that is proportional to the product $\mathbf{M}_H \cdot \mathbf{M}_F$ where \mathbf{M}_H and \mathbf{M}_F are the magnetization of the fixed and free layer respectively. At high field where the two layers are in parallel configuration, a synchronous precession would result in a zero V_{DC} signal. The fact that we are able to observe

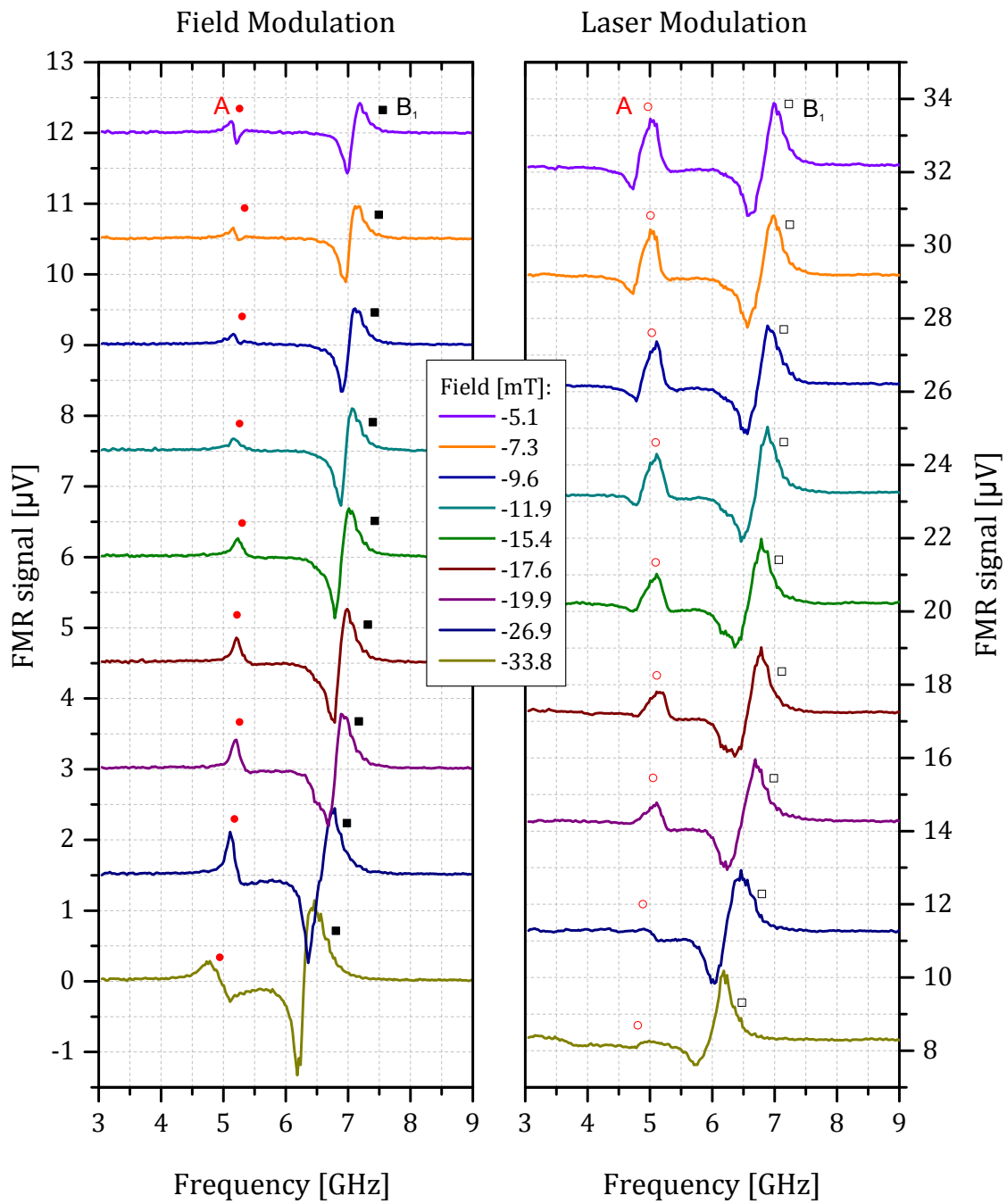


Figure 5.8: STT-FMR spectra of single Co 5 nm / Cu 7 nm / Co 25 nm asymmetric spin valve for $H_{ext} < H_{SW}$. FRM spectra recorded by field (left) and laser (right) modulation techniques. Measurements are carried out when the two magnetic moments are in antiparallel configuration at different values of applied magnetic field. The curves are shifted for clarity along the vertical scale. The symbols in the graph indicate the identified dynamical modes.

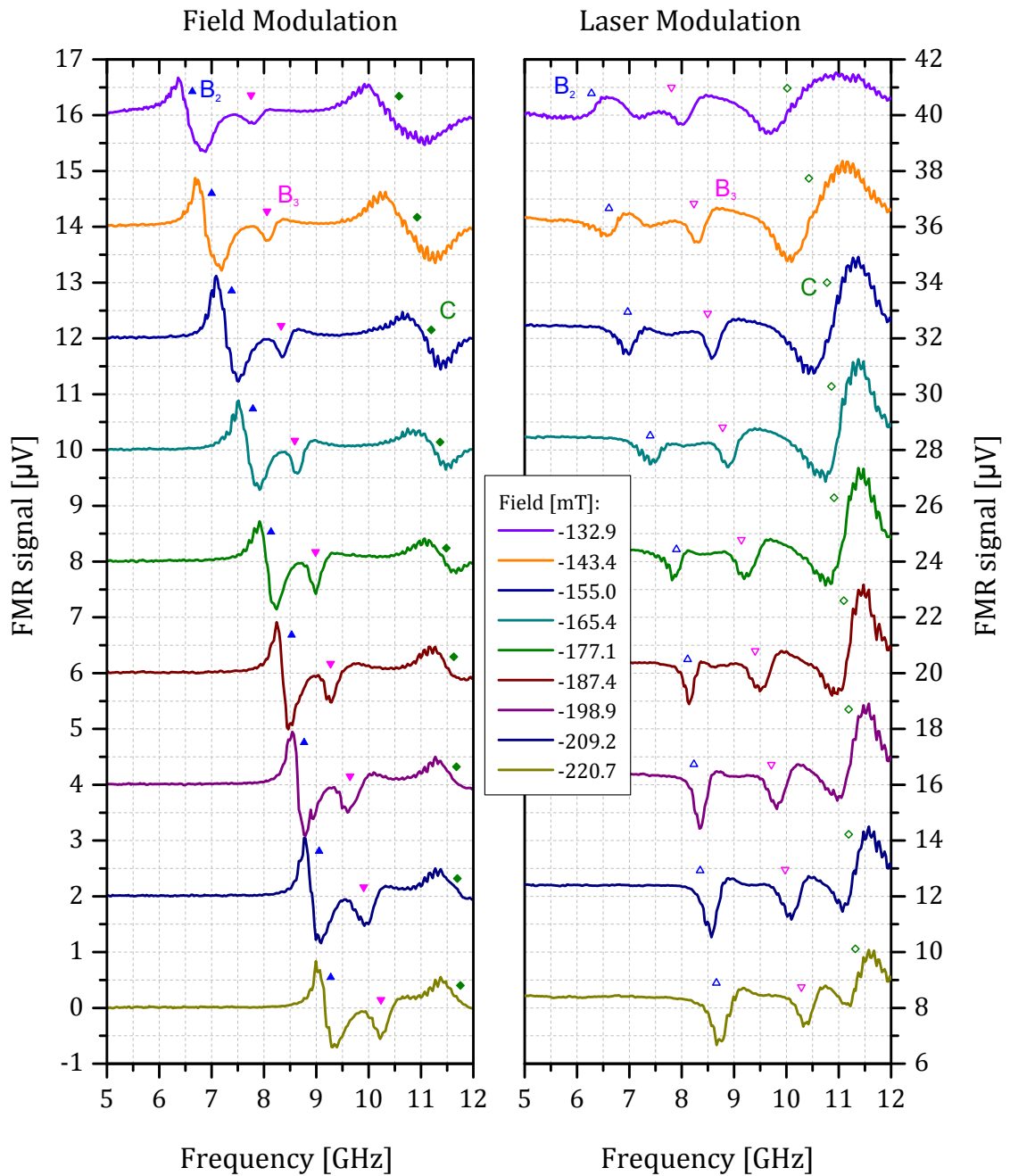


Figure 5.9: STT-FMR spectra of single Co 5 nm / Cu 7 nm / Co 25 nm asymmetric spin valve for $H_{ext} > H_{SW}$. FRM spectra recorded by field (left) and laser (right) modulation techniques. Measurements are carried out when the two magnetic moments are in parallel configuration at different values of applied magnetic field. The curves are shifted for clarity along the vertical scale. The symbols in the graph indicate the identified dynamical modes.

dynamical modes, as shown in Figure 5.9, means that the two magnetic moments are not perfectly aligned and the STT is still efficient. In fact, the closer we are to a perfectly parallel configuration the less detectable the STT signal is.

5.4.1 Peak shape

When the two magnetic moments precess, the resulting $R(t)$ depends on the relative amplitude and phase of the two precessions and determines the shape and the amplitude of the V_{DC} peaks.

The signal obtained with the field modulation technique, in the left graphs of Figures 5.8 and 5.9, is proportional to the variations due to the oscillating magnetic field. In the simplest case, we observe a derivative of the Lorentian function in correspondence of a resonance peak. Nevertheless, as we can see from the reported spectra, in some cases the FMR peaks change their shape and amplitude as a function of the applied field and depending on the dynamical mode excited. A more intense excitation usually corresponds to the uniform precession of the magnetization, while the low amplitude and more distorted peaks reflect a spatial non-uniform excitation.

Studies on FMR lineshape in spin valve devices have been already analyzed and reported in references [89, 97, 93, 90].

5.4.2 Dispersion diagram and interpretation of dynamical modes

In Figure 5.10 we report the dispersion diagram of the FMR spectra illustrated in Figures 5.8 and 5.9. The identification of these modes is not trivial and would require numerical simulations and calculations for a complete understanding. In this work we interpret them by comparing our results with the data of references [93] and [96] presented in Fig 5.11. A complete study on the origin and interpretation of these modes, for very similar magnetic nanostructures, can be found in ref. [108].

We distinguish five different dynamical modes, namely A, B_1 , B_2 , B_3 and C. The first two appear at low values of magnetic field, i.e. when the magnetic layers are in parallel configuration, while the others occur in the antiparallel state. We assume B_1 , B_2 and B_3 to be the dynamical modes of the thin (free) layer of the spin valve, with B_1 being the uniform mode at low field. The modes B_2 and B_3 shift linearly with the same slope and this is a confirmation that they are related to the same magnetic layer. The mode B_3 seems to follow B_1 at higher field. Nevertheless, as shown in the left graph of Fig. 5.8, B_2 has a more intense excitation, that is usually typical of the uniform mode. The change of sign of the peak derivative of B_2 with respect to B_1 (Fig. 5.9) is explained by the change in direction of the free layer, occurring at approximately $\mu_0 H_{SW} \simeq 56$ mT (value for field modulation acquisition).

The resonance mode C shifts with a different slope with respect to B_1 and B_2 and it shows a

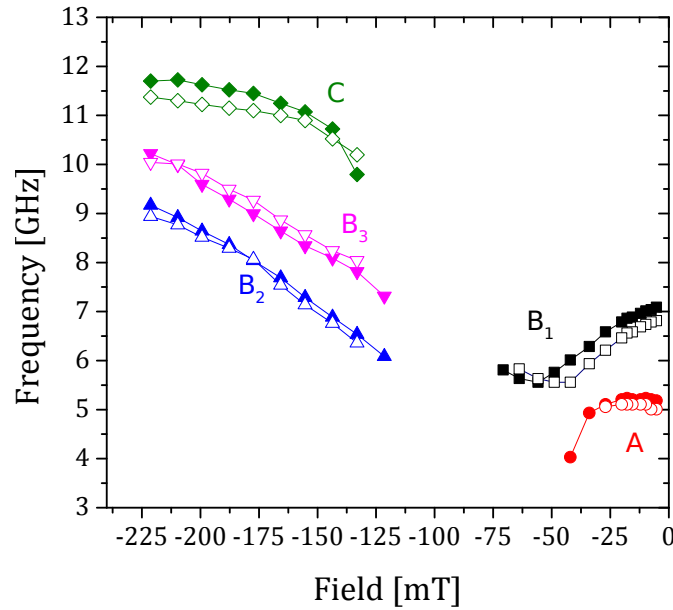


Figure 5.10: Field dependence of the modes in the FMR spectra. Evolution of the dynamical modes reported in Figures 5.8 and 5.9 as a function of the applied magnetic field. Solid symbols correspond to the spectra recorded by field modulation while open symbols refer to the laser modulation technique.

weaker dependence on the magnetic field. It may be identified as the resonant mode of the thick (hard) layer. Comparing the dispersion diagram of Fig. 5.10 with the one reported in Fig. 5.11a, we observe the presence of the same dynamical mode A. In ref. [96] it is identified as a non-uniform mode probably excited by the field produced by the microwave current passing through the nanowire. It has been shown that such microwave induced magnetic field can excite non uniform modes localized to the edge of an elliptical nanomagnet [118].

5.4.3 Effects of laser heating on STT-FMR

In the previous section we analyzed and identified the FMR dynamical modes for an electrodeposited spin valve embedded in a Cu nanowire. Here, we consider and discuss the dynamics of these modes when the spin valve is subjected to a laser heating.

If we shine light on top of the sample (as described in Section 5.3), we have two main consequences: an increase in the overall temperature of the system, and the generation of a temperature gradient along the nanowire. Both of them oscillate at the frequency of the laser diode. Hence any resulting effect is picked up by the lock-in detection at the working frequency of the laser heating. The measured signal is governed by the temperature-dependent magnetic parameters such as saturation magnetization and anisotropy, and by additional contributions due to the effects associated to the temperature gradient, i.e. the thermopower and the heat driven spin-torque, the effect that we are interested to observe.

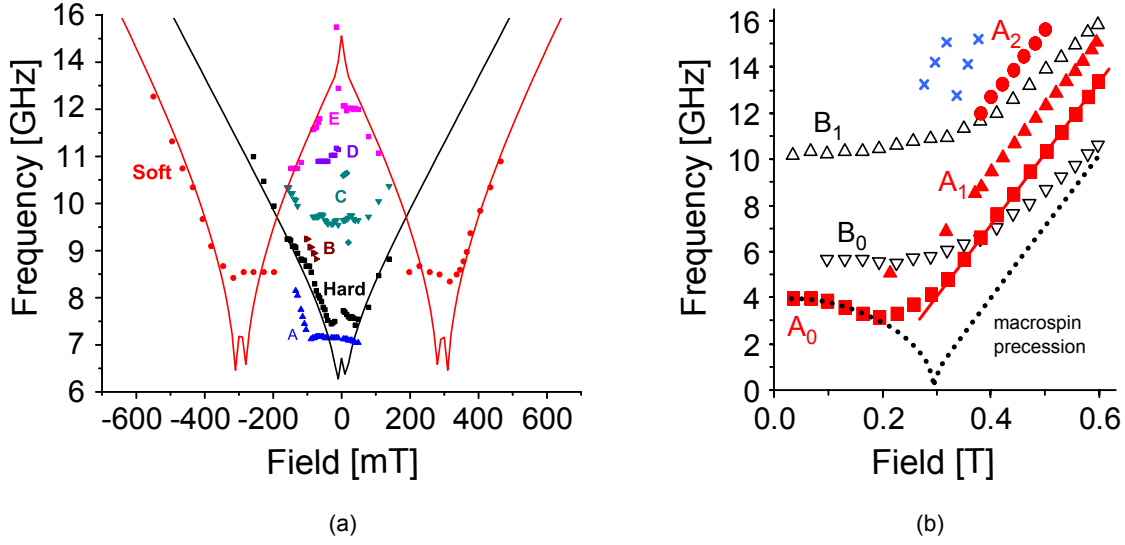


Figure 5.11: Dispersion diagrams of magnetic nanostructures. Field dependence of the FMR modes for (a) electrodeposited Co/Cu/Co spin valve and (b) Py/Cu/PyCu nanopillars. Figures reported and adapted from [93] and [96].

The increase in temperature in the spin valve system, is confirmed by the shift to lower frequency of the dispersion curves for laser modulation in Figure 5.10. This is valid for A, B₁, B₂ and C modes, but not for B₃ whose curve is shifted to higher frequency.

The reason for a frequency shift is explained by the temperature dependence of the saturation magnetization M_s that, for T far from the Curie temperature T_C , is described to a first approximation by the Bloch's law [119]:

$$M_s(T) = M(0) \left[1 - \left(\frac{T}{T_C} \right)^\alpha \right] \quad (5.8)$$

where $M(0)$ is the saturation magnetization at 0 K and $\alpha = 3/2$ for bulk materials. The Bloch $T^{3/2}$ law extended to a nanomagnet has the form [120]:

$$\frac{M(T)}{M(0)} = 1 - \beta T^{3/2} - \beta_1 T \ln T - \beta_2 T, \quad (5.9)$$

where β is the standard Bloch coefficient and β_1 and β_2 are parameters that take into account the size, geometric shape and coupling to surrounding medium.

Hence, according to the Kittel formula, for a constant value of applied magnetic field, an increase in temperature leads to a decrease in magnetization and thus to a shift of the resonance frequency to a lower value. Unlike the other modes, B₃ presents a shift to higher frequency. This is due to the temperature dependence of the demagnetizing field and the

dipolar field exerted by the thick layer on the thin one: a decrease in the dipolar field, for a constant external field, leads to an increase in the resonance frequency. Since this does not occur for B_2 , it suggests that B_3 is the uniform mode of the free layer.

The generation of a temperature gradient is instead demonstrated by the magneto thermoelectric voltage measured across the nanowire. Its value is around $8 \mu\text{V}$ and is given by the baseline of the laser modulated STT-FMR signal. If we compare more in details the baselines of Figures 5.12a and 5.12b we notice a difference of about 330 nV between the parallel and the antiparallel configuration. This is due to the spin-dependence of the Seebeck coefficient [121] and it is a further evidence that we are probing the thermopower. Furthermore, the higher signal-to-noise ratio measured in case of laser modulated FMR, means a higher sensitivity of this technique with respect to the conventional one.

The dynamical modes probed by the laser modulation method in some cases present a different excitation as compared to the conventional method. At low field (Figure 5.12a), when the magnetic layers are in the antiparallel configuration, the uniform mode B_1 exhibits a similar excitation whereas the spatial non uniform mode A appears more excited when the light is shone on the sample. This is in contrast with what stated in ref. [96], i.e. that this mode is generated by the field induced by the microwave current and that therefore should not depend on temperature. In the parallel configuration (Figure 5.12b), mode B_2 shows a higher susceptibility to the external magnetic field than to laser heating. A similar excitation is instead observed for B_3 .

The evidence that the dipolar field decreases with temperature is given by the shift to lower field of the point where the slope of B_1 changes sign, namely the switching field. This shift is estimated to be around 1 mT and it gives the order of magnitude of the field variation sensed by the free layer that oscillates at the frequency of the laser pulses. In other words the laser heating leads to a modulation of the frequency that would result by a field modulation of 1 mT .

This strong dependence of the saturation magnetization and dipolar field on temperature, hinder the identification of the effects due to a thermal spin torque. A more detailed analysis with numerical simulation would be required. An alternative method, presented in Chapter 6, is to study the linear response to a heat driven spin-torque in the quasi static regime.

5.5 Conclusions

Asymmetric Co/Cu/Co spin valves, embedded in Cu nanowires, can be grown by conventional electrodeposition in porous polycarbonate membranes. An original method for growing and contacting these samples, allowed us to carry out high frequency electrical measurement in the GHz range. The spin transfer torque effect, together with a magnetoresistive detection, provides a useful tool to probe and excite electrically the ferromagnetic resonance of magnetic nanostructures. Using this technique, known as STT-FMR, we conducted studies on the magnetization dynamics of these spin valves. In order to investigate the effect of a heat

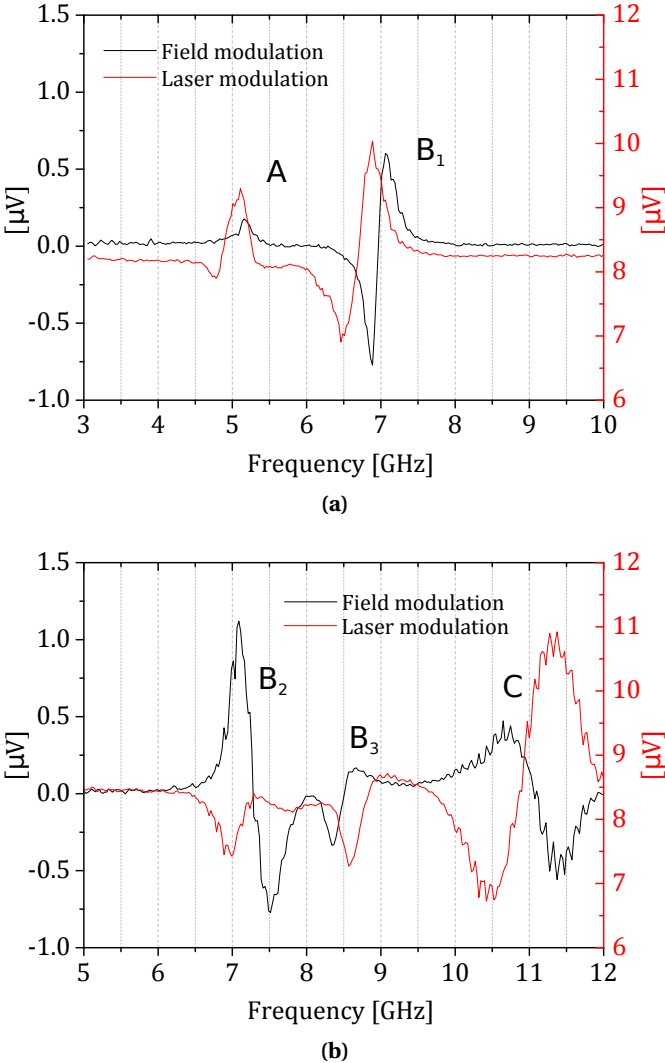


Figure 5.12: Comparison of STT-FMR spectra measured with field and laser modulation techniques. (a) FMR spectrum for field and laser modulation at -12 mT . (b) FMR spectrum for field and laser modulation at -155 mT .

current we employed a laser modulation technique and we compared the results with the data recorded with a conventional field modulated FMR. The strong temperature dependence of the magnetization makes it difficult to isolate the effect of a thermal spin torque induced by the laser heating.

6 Linear Response to a heat-driven Spin Torque

In the experimental work described in Chapter 5, we used a laser modulated FMR technique to investigate the influence of a temperature gradient on the magnetization dynamics of a Co / Cu / Co spin valve. Despite the high sensitivity of this method, the observation of thermal spin torque is hindered by the strong dependence on temperature of the saturation magnetization of the magnetic layers.

Using a different experimental approach, in the present chapter we report the observation of a heat-driven spin torque [122]. Here, we measure electrically the quasi-static magnetic response of a spin valve when subjected to a heat current, generated by two laser diodes heating the electrical contact at one end or the other of the nanowire. In Section 6.1 we give some details on the fabrication process and the measurements setup, while the presentation and discussion of the experimental data are reported in Section 6.2.

6.1 Experimental methods

6.1.1 Sample fabrication

The samples investigated in this experience were grown in nanoporous membranes using the electrodeposition process described in Section 5.2. However, as illustrated in Figure 6.1, the nanowires were fabricated using a small printed circuit board (PCB) as membrane holder, instead of the metallic pin/teflon cup system described in the previous chapter.

For this geometry, both surfaces of the membrane are coated by a gold layer, and electrically connected to the PCB via silver paste. A kapton tape is used both to ensure electrical insulation and to expose only the desired membrane area to the electrolytic bath. As shown in Figure 6.1, the membrane is centered over a hole on the sample holder allowing us to shine light on the bottom side of the sample.

The nanowires are grown from the bottom of the pores, which are covered with a 500 nm thick layer of gold. When one wire reaches the top of the membrane, it forms a contact with the

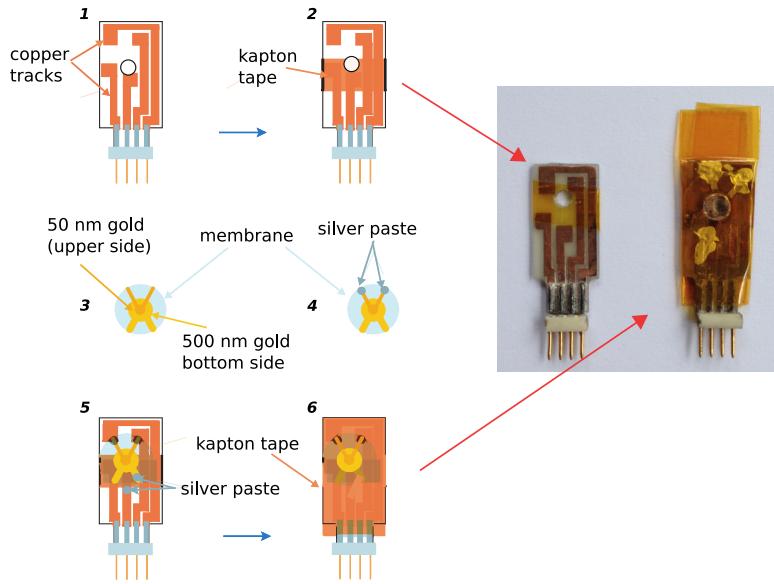


Figure 6.1: Sample preparation procedure for quasi-static electrical measurements. A small printed circuit board is used as a holder for the membrane. It is coated with a gold layer on both sides and electrically connected with silver paste to the PCB. The kapton tape is used to guarantee proper insulation. Image adapted from [123].

top electrode that is generally much thinner than the bottom one. In fact, in order to prevent the obstruction of the pores in the sputtering process, only 50 nm of gold are deposited on top of the membrane. When this top gold layer is contacted by a nanowire, it becomes the working electrode in the electrodeposition process and immediately all pores are blocked by the rapid deposition of Cu everywhere.

The spin valves are 50 nm in diameter, while the thicknesses are 10 nm and 30 nm for the cobalt layers and 10 nm for the copper spacer. As described in Section 6.1 these nominal values are determined after a calibration process by scaling down the time it takes to fill a pore entirely with Co or Cu. The membrane thickness is 5 μm and it defines the length of the nanowire.

6.1.2 Measurement setup

As shown in Figure 6.2, the temperature gradient is generated across the sample by means of the light emitted by two laser diodes (80 mW, wavelength of 640 nm). The light is collimated into an optical fiber and it is brought to either sides of the filled membrane. We estimated a maximum laser power density on the sample surface of 9 W/cm^2 . Compared to the setup described in Chapter 5, with this system we have the possibility to revert the direction of the temperature gradient inside the nanowire.

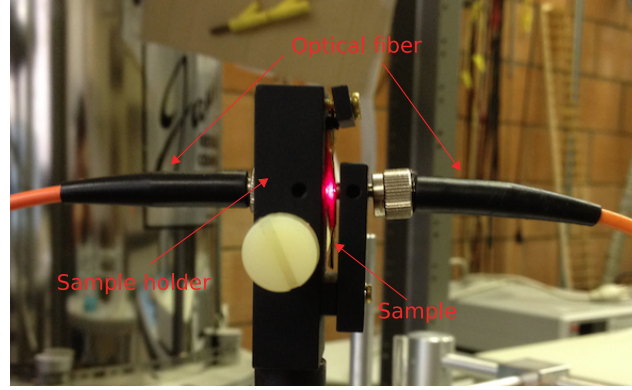


Figure 6.2: Sample holder with double laser heating system. The sample is heated on both sides by the light produced with two laser diodes and collimated into optical fibers, that terminate at one side or the other of the membrane.

Since the bottom side of the sample is made of a thick Au layer, the heat current obtained shining light on this side is lower than when shining light onto the top layer, as this is much thinner, and therefore poorly heat-sunk. Thanks to the thermoelectric measurements of the sample [110], and assuming a reasonable value for the Seebeck coefficient [124], we can estimate the temperature gradient generated inside the nanowires. Thus, we find a temperature difference ΔT of about 5 K and 0.5 K when we shine light on the top and on the bottom of the membrane, respectively. Considering the total length of the nanowire, this leads to the generation of a temperature gradient of the order of 10^4 K/cm when shining light on the thin electrode and 10 times smaller when we heat the thick one.

During the measurement, the laser diodes are turned on and off at a frequency f of 22 Hz, while a continuous current I_{DC} of about $100 \mu\text{A}$ is applied to the nanowire. This current is small enough to prevent any significant increase of temperature due to Joule heating. A lock-in amplifier is used to measure the quantity $\Delta R I_{DC}$, with ΔR oscillating at the frequency f and given by

$$\Delta R = \frac{\partial R}{\partial T} \Delta T + \frac{\partial R}{\partial \mathbf{M}} \Delta \mathbf{M} \quad (6.1)$$

The first term in Equation (6.1) represents the temperature dependence of the resistance $\frac{\partial R}{\partial T}$ and it does not depend on the magnetization [124], whereas the term $\frac{\partial R}{\partial \mathbf{M}}$ corresponds to the magnetoresistance of the spin valve. Taking into account the torque $\boldsymbol{\tau}$ produced by a heat current \mathbf{j}_Q , $\Delta \mathbf{M}$ is expressed as

$$\Delta \mathbf{M} = \frac{\partial \mathbf{M}}{\partial \boldsymbol{\tau}} \frac{\partial \boldsymbol{\tau}}{\partial \mathbf{j}_Q} \mathbf{j}_Q, \quad (6.2)$$

where the first term, $\frac{\partial \mathbf{M}}{\partial \boldsymbol{\tau}}$ corresponds to the susceptibility to a torque of the free layer, namely

the response of the magnetization to a torque, while the second term $\frac{\partial \tau}{\partial j_Q}$, identifies the heat-driven spin torque that we are interested in characterizing.

6.2 Results and discussion

The top graph of Figure 6.3 shows the magnetoresistance of our 30 nm Co / 10 nm Cu / 10 nm Co spin valve. The curve presents a difference in resistance between the parallel and antiparallel states of about 0.15Ω . The measurements were carried out at room temperature by sweeping the magnetic field from negative to positive (black curve) and from positive to negative (red curve) values. The sharp steps we notice at the rising edges of the GMR ramp (at ± 100 mT), correspond to the switching of the free layer (the thinner layer) from parallel to antiparallel configuration. At higher fields, the gradual decrease of the resistance is associated with the fixed layer undergoing a reorientation, along the external magnetic field, of its magnetization until saturation is reached, i.e. when we pass to a parallel configuration. This progressive edge is reversible, i.e. the measurements stay on the same curve when doing minor loops in this region, while the sharp edge is characterized by a hysteresis when doing minor loops.

The two bottom traces of Figure 6.3 represent the lock-in signal as a function of the applied magnetic field, measured across the same spin valve and obtained by switching on and off the light of the lasers. The upper one is measured when the light is shone on the top electrode, while the lower trace is recorded when we heat the bottom side of the membrane. As expected, the temperature oscillation of the spin valve is about 10 times smaller when the light heats up the thick Au contact.

The response of the resistance to a heat current has been expressed by Equation 6.1: the first term is what causes the baseline of our measurements, i.e. the thermoelectric power, while the second term is what gives rise to the peaks occurring at about ± 125 mT, in correspondence of a reversible transition of the GMR. These peaks have been already observed before in [125, 126]. From a comparison of the two traces we notice that when we reverse the direction of the heat current the peaks change sign. This means that if in one case the heat current increases the resistance, when flowing in the other direction it decreases it.

The small steps in ΔR occurring at ± 100 mT, i.e. when the free layer switches its direction, are attributed to the spin-dependence of the thermoelectric power that is known to depend on the magnetic configuration of the top layers [121]. Furthermore, we notice other peaks in the ΔR response occurring at about ± 25 mT which apparently do not correspond to any evident changes in resistance. Like the others, these peaks change in sign when the sense of the heat current is reversed. Nevertheless, a careful examination of the GMR data reveals the presence of small steps barely distinct from the noise near the same value of fields where these peaks occur. The low value of field at which these peaks occur suggests that they are probably produced by the motion of a domain wall in the 30 nm thick cobalt layer.

At this point we quantify the effect we observed by modelling the peaks associated to the switching of the magnetization. A simple model for the magnetoresistance is given by Equation

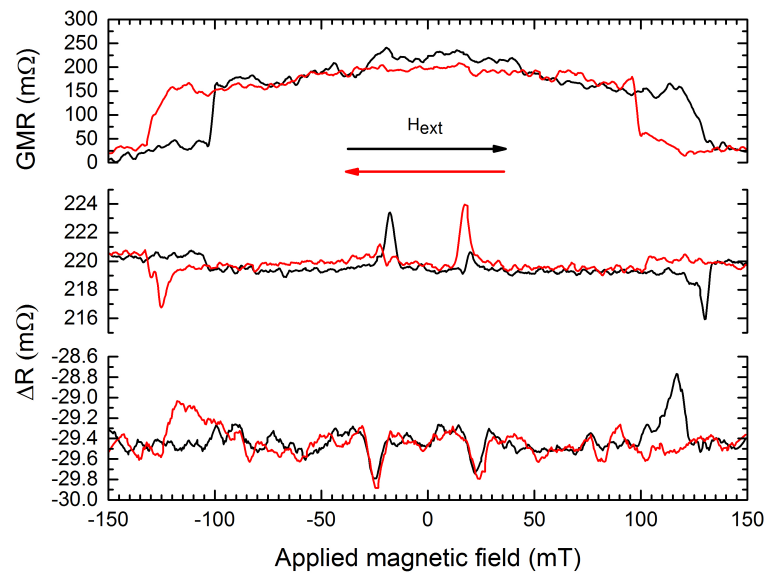


Figure 6.3: GMR and heat induced lockin voltage of a Co/Cu/Co spin valve. Magnetoresistance of a single nanowire containing one spin valve (top). Lock-in detected amplitude oscillation of the resistance when light heats up the thin Au layer (middle), or the thick one (bottom); data treated with a 10-point Savitzky-Golay filter. Colors correspond to the sense of the ramp indicated by the arrows. Image adapted from [122].

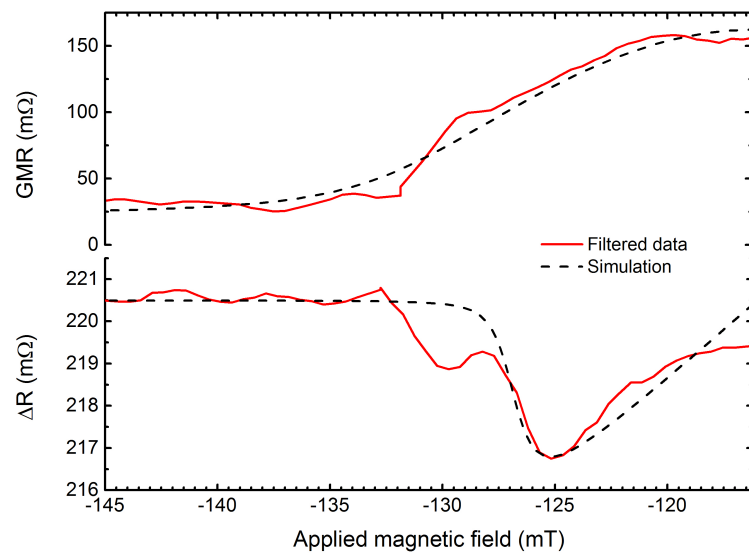


Figure 6.4: Data and simulation of the GMR and heat induced lockin voltage of a Co/Cu/Co spin valve. Simulation (solid lines) for the magnetic field dependence of the GMR and the lock-in detected voltage (dashed lines) for a given spin torque. The parameter is the angle between the magnetic field and the anisotropy axis. The fit uses $H_{||} = 125.2$ mT, and $H_t = 2.15$ mT. Image taken from [122].

(5.2) in Section 5.1.1.

The magnetic field dependence of the magnetization response to a charge-driven spin torque was already observed in ref. [127]. By analogy, we assume a torque proportional to the heat current acting on the the magnetization of the free layer (of thickness d). In order to quantify the effect of a heat-driven spin torque, we consider the Landau-Lifshitz equation for the unit vector $\hat{\mathbf{s}}$ parallel to the magnetization. Using the notation of ref. [128], we write:

$$\frac{d\hat{\mathbf{s}}}{dt} = \hat{\mathbf{s}} \times \left(-|\gamma_g| \mu_0 \left(\mathbf{H}_{\text{eff}} + \frac{b j_Q}{\mu_0 M_s d} \hat{\mathbf{S}} \right) \right) \quad (6.3)$$

The torque $\boldsymbol{\tau}_\perp = b j_Q \hat{\mathbf{s}} \times \hat{\mathbf{S}}$ is field-like (see Section 5.1.2), and its magnitude is equivalent to a field $H_t = -b j_Q / (\mu_0 M_s d)$ in the direction $\hat{\mathbf{S}}$ of the magnetization of the thick layer. The effective field \mathbf{H}_{eff} includes the applied field and a uniaxial anisotropy characterized by the field H_\parallel .

We can express the linear response to the torque (normal to the plane of the layer) $\boldsymbol{\tau}_\perp$ by the angular deviation $\delta\phi$ of the magnetization \mathbf{M} with respect to its equilibrium orientation in a given external applied field. The angle of rotation $\delta\phi = \Delta M / M_s$, is given by :

$$\delta\phi = \frac{H_t \sin \phi_0}{H_\parallel \cos(2\phi_0) + H_{\text{app}} \cos(\Theta - \phi_0)} \quad (6.4)$$

where ϕ_0 gives the orientation at equilibrium of the magnetization with magnitude M_s in the applied magnetic field H_{app} , whereas Θ is the angle between H_{app} and the axis of the anisotropy of magnitude H_\parallel^{an} in the plane of the free layer. The angle ϕ_0 is given by expression that denotes the equilibrium condition:

$$H_\parallel^{\text{an}} \sin \phi_0 \cos \phi_0 - H_{\text{app}} \sin(\Theta - \phi_0) = 0 \quad (6.5)$$

According to Equation (6.2) and Equation (6.5), we calculate the response to a given torque $\boldsymbol{\tau}_\perp$ as a function of the applied magnetic field and we plot it in Figure 6.4 along with the data for the GMR and one of the peaks in ΔR . From the GMR curve, and in particular from the switching field of the magnetization, we get the value for the anisotropy field $H_\parallel = 125.2$ mT and we find that the heat current j_Q associated with the temperature difference of 5 K induces a torque which is equivalent to the one that would be obtained by applying a field $H_t = 2.15$ mT.

We compare now the heat-driven and the charge-driven spin currents that produce torques on the free layer. We proceed as in ref. [104] to evaluate the effect of a heat-driven spin current on magnetization switching, and we use the same approach of ref. [107] for the analysis of the experimental demonstration of heat-driven spin torque dynamics. According to the three-current model presented in Section 1.1.1, the spin current obtained by a charge current or a heat current, scales like $\nabla V / (S \nabla T)$, with S being the effective Seebeck coefficient. Therefore,

the change in resistance ΔR_{charge} and ΔR_{heat} caused by the charge and the heat driven spin currents $j_{s,\text{charge}}$ and $j_{s,\text{heat}}$, is given by:

$$\frac{\Delta R_{\text{charge}}}{\Delta R_{\text{heat}}} = \frac{j_{s,\text{charge}}}{j_{s,\text{heat}}} = \frac{\nabla V}{S\nabla T} \quad (6.6)$$

From the data contained in [127] and considering a value of about $10^{-7} \Omega\text{m}$ for the resistivity of the electrodeposited cobalt, we estimate $\nabla V \approx 10^3 \text{ V/m}$ and ΔR_{charge} of about 30 m Ω . The data reported here show a resistance change ΔR_{heat} of about 3 m Ω . The temperature gradient ∇T is estimated from the temperature difference ΔT and from the heat conductivity of Cu κ_{Cu} , since the nanowire is almost entirely made of copper. Applying Fourier law to the cobalt layer, we find

$$\nabla T = \frac{\kappa_{\text{Cu}}}{\kappa_{\text{Co}}} \frac{\Delta T}{L}, \quad (6.7)$$

where L is the length of the nanowire and κ_{Co} the heat conductivity of cobalt. With the numerical values reported here we found an effective Seebeck coefficient S of about 27 $\mu\text{V/K}$, which is a very reasonable value for electrodeposited cobalt [121].

6.3 Conclusions

In summary, we used single Co / Cu / Co electrodeposited spin valves embedded in Cu nanowires to investigate the effect of a heat current on the magnetization dynamics. We studied the quasi-static response of the magnetization to a heat current generated by two laser diodes, heating either one end or the other of the sample. We observed a variation in the resistance induced by a heat-driven spin torque, represented by peaks occurring in correspondence of the GMR transition. By conducting quantitative analysis we evaluated this effect and we compared it to the spin transfer torque previously observed in the same structures. We found that a temperature difference of the order of 5 K is sufficient to produce a thermal spin torque equivalent to the effect of a field of about 2 mT.

7 Summary and conclusions

In this thesis we investigated the effect of a heat current on the magnetization dynamics in two types of materials and configurations: magnetic insulators and metallic nanostructures.

In the first case we conducted studies on yttrium iron garnet (YIG) samples subjected to a temperature gradient. The formalism newly developed by the group that describes the irreversible thermodynamics predicts a new effect that can be described as a magnetic field induced by a thermal gradient. By analogy to the well known Seebeck effect we suggest to refer to it as magnetic Seebeck effect (MSE).

By conducting transmission measurement in a thin slab of single crystal of YIG in presence of a thermal gradient, we observed that magnetostatic wave propagating from the cold to the hot side were less attenuated than when travelling in the opposite direction. With this experiment we provided evidence for the MSE and we showed that it can modulate the magnetic damping depending on the direction of the propagating magnetostatic modes with respect to the temperature gradient. To investigate further the MSE we conducted FMR studies on normally magnetized YIG disks subjected to a temperature gradient. Although we observed the excitation of azimuthal modes in presence of a temperature gradient, we were not able to reproduce the same effect by using a different resonant system.

In the second part of this thesis we focused our investigation on metallic nanostructures subjected to a heat current, hence we moved from insulators to a conductive materials and from macroscopic to nanoscopic scale. We fabricated Co / Cu / Co asymmetric spin valves placed in the middle of copper nanowires by using a porous template membrane and a conventional electrodeposition process. Thanks to an original design for contacting these samples, we were able to carry out high frequency electrical measurements and we showed that the laser modulation technique can be a very sensitive tool to conduct FMR studies on these samples.

The three-current model (current of entropy, of spin up and spin down electrons) predicts that in a metal a heat current induces a spin current which can influence the magnetization dynamics like a charge-driven spin current would. We reported the observation of a heat-

Chapter 7. Summary and conclusions

driven spin torque by measuring electrically the quasi-static magnetic response of a spin valve when subjected to the heat current, generated by two laser diodes heating the electrical contact at one end or the other of the nanowire. We observed a variation in the resistance induced by this heat-driven torque, represented by peaks in the response versus magnetic field. These peaks occurred at the GMR transitions. By conducting quantitative analysis we evaluated this effect and we compared it to the spin transfer torque previously observed in the same structures. We found that a temperature difference of the order of 5 K is sufficient to produce a thermal spin torque equivalent to the effect of a field of about 2 mT.

In conclusion, we demonstrated experimentally that the application of a heat current can influence the spin dynamics in different ways depending on the nature and the structure of the material. In case of insulator it modifies the damping positively or negatively, depending on the sense of propagation with respect to the direction of the temperature gradient. In metallic spin valves, it produces a spin current that in turn exerts a torque on the magnetization of the free layer.

Bibliography

- [1] Slonczewski, J. Current-driven excitation of magnetic multilayers. *Journal of Magnetism and Magnetic Materials* **159**, L1–L7 (1996).
- [2] Berger, L. Emission of spin waves by a magnetic multilayer traversed by a current. *Physical Review B* **54**, 9353–9358 (1996).
- [3] Bauer, G. E. W., MacDonald, A. H. & Maekawa, S. Spin Caloritronics. *Solid State Communications* **150**, 459–460 (2010).
- [4] Bauer, G. E. W., Saitoh, E. & van Wees, B. J. Spin caloritronics. *Nature Materials* **11**, 391–399 (2012).
- [5] Johnson, M. & Silsbee, R. H. Thermodynamic analysis of interfacial transport and of the thermomagnetolectric system. *Physical Review B* **35**, 4959–4972 (1987).
- [6] Uchida, K. *et al.* Observation of the spin Seebeck effect. *Nature* **455**, 778–781 (2008).
- [7] Uchida, K. *et al.* Long-range spin Seebeck effect and acoustic spin pumping. *Nature materials* **10**, 737–741 (2011).
- [8] Boona, S. R., Myers, R. C. & Heremans, J. P. Spin caloritronics. *Energy & Environmental Science* **7**, 885–910 (2014).
- [9] Harman, T. C. & Honig, J. M. *Thermoelectric and thermomagnetic effects and applications* (McGraw-Hill, 1967).
- [10] Ashcroft, N. W. & Mermin, N. D. *Solid State Physics*, vol. 2 (Saunders, Philadelphia, 1976).
- [11] Mott, S. N. F. & Jones, H. *The theory of the properties of metals and alloys* (Dover Publications, 1958).
- [12] Onsager, L. Reciprocal Relations in Irreversible Processes. II. *Physical Review* **38**, 2265–2279 (1931).
- [13] Brechet, S. D. & Ansermet, J.-P. Heat-driven spin currents on large scales. *physica status solidi (RRL) - Rapid Research Letters* **5**, 423–425 (2011).
- [14] Slachter, A., Bakker, F. L., Adam, J.-P. & van Wees, B. J. Thermally driven spin injection from a ferromagnet into a non-magnetic metal. *Nat Phys* **6**, 879–882 (2010).
- [15] Flipse, J., Bakker, F. L., Slachter, A., Dejene, F. K. & van Wees, B. J. Direct observation of the spin-dependent Peltier effect. *Nature Nanotechnology* **7**, 166–168 (2012).
- [16] Saitoh, E., Ueda, M., Miyajima, H. & Tatara, G. Conversion of spin current into charge current at room temperature: Inverse spin-Hall effect. *Applied Physics Letters* **88**, 182509 (2006).
- [17] Jungwirth, T., Wunderlich, J. & Olejnik, K. Spin Hall effect devices. *Nature Materials* **11**, 382–390 (2012).

Bibliography

- [18] Jaworski, C. M. *et al.* Observation of the spin-Seebeck effect in a ferromagnetic semiconductor. *Nature materials* **9**, 898–903 (2010).
- [19] Uchida, K. *et al.* Spin Seebeck insulator. *Nature materials* **9**, 894–897 (2010).
- [20] Bosu, S. *et al.* Spin Seebeck effect in thin films of the Heusler compound Co₂MnSi. *Physical Review B* **83**, 224401 (2011).
- [21] Jaworski, C. M., Myers, R. C., Johnston-Halperin, E. & Heremans, J. P. Giant spin Seebeck effect in a non-magnetic material. *Nature* **487**, 210–213 (2012).
- [22] Schmid, M. *et al.* Transverse spin seebeck effect versus anomalous and planar nernst effects in permalloy thin films. *Physical Review Letters* **111**, 187201 (2013).
- [23] Adachi, H., Uchida, K.-i., Saitoh, E. & Maekawa, S. Theory of the spin Seebeck effect. *Reports on Progress in Physics* **76**, 036501 (2013).
- [24] Tikhonov, K. S., Sinova, J. & Finkel'stein, A. M. Spectral non-uniform temperature and non-local heat transfer in the spin Seebeck effect. *Nature communications* **4**, 1945 (2013).
- [25] Padrón-Hernández, E., Azevedo, a. & Rezende, S. M. Amplification of spin waves by thermal spin-transfer torque. *Physical Review Letters* **107**, 197203 (2011).
- [26] Obry, B., Vasyuchka, V. I., Chumak, A. V., Serga, A. A. & Hillebrands, B. Spin-wave propagation and transformation in a thermal gradient. *Applied Physics Letters* **101**, 192406 (2012).
- [27] Lu, L., Sun, Y., Jantz, M. & Wu, M. Control of Ferromagnetic Relaxation in Magnetic Thin Films through Thermally Induced Interfacial Spin Transfer. *Physical Review Letters* **108**, 257202 (2012).
- [28] Da Silva, G. L., Vilela-Leo, L. H., Rezende, S. M. & Azevedo, a. Spin current injection by spin Seebeck and spin pumping effects in yttrium iron garnet/Pt structures. *Journal of Applied Physics* **111**, 07C513 (2012).
- [29] Tserkovnyak, Y., Brataas, A., Bauer, G. & Halperin, B. Nonlocal magnetization dynamics in ferromagnetic heterostructures. *Reviews of Modern Physics* **77**, 1375–1421 (2005).
- [30] Da Silva, G. L. *et al.* Enhancement of spin wave excitation by spin currents due to thermal gradient and spin pumping in yttrium iron garnet/Pt. *Applied Physics Letters* **102**, 012401 (2013).
- [31] Jungfleisch, M. B. *et al.* Heat-induced damping modification in yttrium iron garnet/platinum hetero-structures. *Applied Physics Letters* **102**, 062417 (2013).
- [32] Kajiwara, Y. *et al.* Spin-relaxation modulation and spin-pumping control by transverse spin-wave spin current in Y₃Fe₅O₁₂. *Applied Physics Letters* **103**, 052404 (2013).
- [33] Papa, E. *Magnetization Dynamics of Insulators Subject to a Heat Current*. Ph.D. thesis, EPFL (2013).
- [34] Papa, E., Barnes, S. E. & Ansermet, J.-P. Local Excitation of Magnetostatic Modes in YIG. *IEEE Transactions on Magnetics* **49**, 1055–1059 (2013).
- [35] Cunha, R. O., Padrón-Hernández, E., Azevedo, A. & Rezende, S. M. Controlling the relaxation of propagating spin waves in yttrium iron garnet/Pt bilayers with thermal gradients. *Physical Review B* **87**, 184401 (2013).
- [36] Ando, K. *et al.* Electric Manipulation of Spin Relaxation Using the Spin Hall Effect. *Physical Review Letters* **101**, 036601 (2008).
- [37] Geller, S. & Gilleo, M. A. Structure and ferrimagnetism of yttrium and rare-earth-iron garnets. *Acta Crystallographica* **10**, 239 (1957).

- [38] Liu, Z., Giesen, F., Zhu, X., Sydora, R. D. & Freeman, M. R. Spin Wave Dynamics and the Determination of Intrinsic Damping in Locally Excited Permalloy Thin Films. *Physical Review Letters* **98**, 087201 (2007).
- [39] Cherepanov, V., Kolokolov, I. & L'vov, V. The saga of YIG: Spectra, thermodynamics, interaction and relaxation of magnons in a complex magnet. *Physics Reports* **229**, 81–144 (1993).
- [40] Kruglyak, V. V., Demokritov, S. O. & Grundler, D. Magnonics. *Journal of Physics D: Applied Physics* **43**, 264001 (2010).
- [41] Serga, a. a., Chumak, a. V. & Hillebrands, B. YIG magnonics. *Journal of Physics D: Applied Physics* **43**, 264002 (2010).
- [42] Lenk, B., Ulrichs, H., Garbs, F. & Münzenberg, M. The building blocks of magnonics. *Physics Reports* **507**, 107–136 (2011).
- [43] Kruglyak, V. & Hicken, R. Magnonics: Experiment to prove the concept. *Journal of Magnetism and Magnetic Materials* **306**, 191–194 (2006).
- [44] S.V. Vonsovskii. *Ferromagnetic resonance: the phenomenon of resonant absorption of a high-frequency magnetic field in ferromagnetic substances* (Elsevier Science, 1966).
- [45] Stancil, D. D. & Prabhakar, A. *Spin Waves: Theory and Applications* (Springer, 2008).
- [46] Gurevich, A. & Melkov, G. *Magnetization oscillations and waves* (CRC Press, 1996).
- [47] Landau, L. D. & Lifshitz, E. On the theory of the dispersion of magnetic permeability in ferromagnetic bodies. *Phys. Z. Sowjetunion* **8**, 153–169 (1935).
- [48] Gilbert, T. Classics in Magnetism A Phenomenological Theory of Damping in Ferromagnetic Materials. *IEEE Transactions on Magnetics* **40**, 3443–3449 (2004).
- [49] Kittel, C. On the Theory of Ferromagnetic Resonance Absorption. *Physical Review* **73**, 155–161 (1948).
- [50] Walker, L. R. Magnetostatic Modes in Ferromagnetic Resonance. *Physical Review* **105**, 390–399 (1957).
- [51] Fletcher, P. C. & Kittel, C. Considerations on the Propagation and Generation of Magnetostatic Waves and Spin Waves. *Physical Review* **120**, 2004–2006 (1960).
- [52] Eshbach, J. R. & Damon, R. W. Surface Magnetostatic Modes and Surface Spin Waves. *Physical Review* **118**, 1208–1210 (1960).
- [53] Damon, R. & Eshbach, J. Magnetostatic modes of a ferromagnet slab. *Journal of Physics and Chemistry of Solids* **19**, 308–320 (1961).
- [54] Damon, R. W. & Van De Vaart, H. Propagation of Magnetostatic Spin Waves at Microwave Frequencies in a Normally-Magnetized Disk. *Journal of Applied Physics* **36**, 3453 (1965).
- [55] Tamaru, S. *et al.* Measurement of magnetostatic mode excitation and relaxation in permalloy films using scanning Kerr imaging. *Physical Review B* **70**, 104416 (2004).
- [56] Azevedo, A. & Rezende, S. M. Spatial distribution of magnetostatic modes in a thin YIG slab. *Journal of Magnetism and Magnetic Materials* **104-107**, 1039–1040 (1992).
- [57] Bauer, M. *et al.* Observation of Spatiotemporal Self-Focusing of Spin Waves in Magnetic Films. *Physical Review Letters* **81**, 3769–3772 (1998).
- [58] Lee, S.-C. *et al.* Magnetic permeability imaging of metals with a scanning near-field microwave microscope. *Applied Physics Letters* **77**, 4404 (2000).
- [59] Brechet, S. D., Vetro, F. a., Papa, E., Barnes, S. E. & Ansermet, J.-P. Evidence for a Magnetic Seebeck Effect. *Physical Review Letters* **111**, 87205 (2013).

Bibliography

- [60] Brechet, S. D. & Ansermet, J. P. Thermodynamics of a continuous medium with electric and magnetic dipoles. *The European Physical Journal B* **86**, 318 (2013).
- [61] Reuse, F. *Electrodynamique* (PPUR Presses polytechniques, 2012).
- [62] Griffiths, D. J. *Introduction to Electrodynamics* (Pearson, 2013).
- [63] Kurebayashi, H. *et al.* Controlled enhancement of spin-current emission by three-magnon splitting. *Nature materials* **10**, 660–664 (2011).
- [64] Duncan, J. A., Storey, B. E., Tooke, A. O. & Cracknell, A. P. Magnetostatic modes observed in thin single-crystal films of yttrium iron garnet at Q-band frequencies. *Journal of Physics C: Solid State Physics* **13**, 2079–2095 (1980).
- [65] Uchida, K.-i. *et al.* Observation of longitudinal spin-Seebeck effect in magnetic insulators. *Applied Physics Letters* **97**, 172505 (2010).
- [66] Walter, M. *et al.* Seebeck effect in magnetic tunnel junctions. *Nature materials* **10**, 742–746 (2011).
- [67] Dillon, J. F. Magnetostatic Modes in Disks and Rods. *Journal of Applied Physics* **31**, 1605 (1960).
- [68] Ikuzawa, Y. & Abe, K. Resonant modes of magnetostatic waves in a normally magnetized disk. *Journal of Applied Physics* **48**, 3001–3007 (1977).
- [69] Damon, R. & van de Vaart, H. Dispersion of spin waves and magnetoelastic waves in YIG. *Proceedings of the IEEE* **53**, 348–354 (1965).
- [70] Eshbach, J. R. Spin-wave propagation and the magnetoelastic interaction in yttrium iron garnet. *Journal of Applied Physics* **34**, 1298–1304 (1963).
- [71] Edwards, E. R. J., Buchmeier, M., Demidov, V. E. & Demokritov, S. O. Magnetostatic spin-wave modes of an in-plane magnetized garnet-film disk. *Journal of Applied Physics* **113**, 103901 (2013).
- [72] Sigalov, M., Kamenetskii, E. O. & Shavit, R. Magnetic-dipolar and electromagnetic vortices in quasi-2D ferrite discs. *Journal of Physics: Condensed Matter* **21**, 016003 (2009).
- [73] Kamenetskii, E. O., Sigalov, M. & Shavit, R. Manipulating microwaves with magnetic-dipolar-mode vortices. *Physical Review A* **81**, 053823 (2010).
- [74] Kamenetskii, E., Saha, A. & Awai, I. Interaction of magnetic-dipolar modes with microwave-cavity electromagnetic fields. *Physics Letters A* **332**, 303–309 (2004).
- [75] Alex-enraver. Spin-valve GMR.svg. URL http://upload.wikimedia.org/wikipedia/commons/9/93/Spin-valve_GMR.svg.
- [76] Baibich, M. N. *et al.* Giant magnetoresistance of (001)Fe/(001)Cr magnetic superlattices. *Physical Review Letters* **61**, 2472–2475 (1988).
- [77] Binasch, G., Grünberg, P., Saurenbach, F. & Zinn, W. Enhanced magnetoresistance in layered magnetic structures with antiferromagnetic interlayer exchange. *Physical Review B* **39**, 4828–4830 (1989).
- [78] Julliere, M. Tunneling between ferromagnetic films. *Physics Letters A* **54**, 225–226 (1975).
- [79] Chappert, C., Fert, A. & Van Dau, F. N. The emergence of spin electronics in data storage. *Nature materials* **6**, 813–823 (2007).
- [80] Katine, J., Albert, F., Buhrman, R., Myers, E. & Ralph, D. Current-Driven Magnetization Reversal and Spin-Wave Excitations in Co /Cu /Co Pillars. *Physical Review Letters* **84**, 3149–3152 (2000).
- [81] Slonczewski, J. C. Currents and torques in metallic magnetic multilayers. *Journal of Magnetism and Magnetic Materials* **247**, 324–338 (2002).

- [82] Stiles, M. D. & Zangwill, A. Anatomy of Spin-Transfer Torque. *Phys. Rev. B* **66**, 014407 (2002).
- [83] Brataas, A., Bauer, G. E. W. & Kelly, P. J. Non-collinear magnetoelectronics. *Physics Reports* **427**, 157–255 (2006).
- [84] Barnaś, J., Fert, a., Gmitra, M., Weymann, I. & Dugaev, V. From giant magnetoresistance to current-induced switching by spin transfer. *Physical Review B* **72**, 24426 (2005).
- [85] Brataas, A., Kent, A. D. & Ohno, H. Current-induced torques in magnetic materials. *Nature Materials* **11**, 372–381 (2012).
- [86] Ralph, D. C. & Stiles, M. D. Spin transfer torques. *Journal of Magnetism and Magnetic Materials* **320**, 1190–1216 (2008).
- [87] Sun, J. Z. Spin angular momentum transfer in current-perpendicular nanomagnetic junctions. *IBM Journal of Research and Development* **50**, 81–100 (2006).
- [88] Wang, C., Seinige, H. & Tsoi, M. Ferromagnetic resonance driven by an ac current: A brief review. *Low Temperature Physics* **39**, 247–251 (2013).
- [89] Tulapurkar, A. A. *et al.* Spin-torque diode effect in magnetic tunnel junctions. *Nature* **438**, 339–342 (2005).
- [90] Sankey, J. C. *et al.* Measurement of the spin-transfer-torque vector in magnetic tunnel junctions. *Nature Physics* **4**, 67–71 (2007).
- [91] Wang, C. *et al.* Bias and angular dependence of spin-transfer torque in magnetic tunnel junctions. *Physical Review B* **79**, 224416 (2009).
- [92] Kubota, H. *et al.* Quantitative measurement of voltage dependence of spin-transfer torque in MgO-based magnetic tunnel junctions. *Nature Physics* **4**, 37–41 (2008).
- [93] Sankey, J. C. *et al.* Spin-transfer-driven ferromagnetic resonance of individual nanomagnets. *Physical Review Letters* **96**, 227601 (2006).
- [94] Chen, W., Beaujour, J. M. L., De Loubens, G., Kent, A. D. & Sun, J. Z. Spin-torque driven ferromagnetic resonance of CoNi synthetic layers in spin valves. *Applied Physics Letters* **92**, 012507 (2008).
- [95] Mourachkine, a., Yazyev, O. V., Ducati, C. & Ansermet, J. P. Template nanowires for spintronics applications: Nanomagnet microwave resonators functioning in zero applied magnetic field. *Nano Letters* **8**, 3683–3687 (2008).
- [96] Biziere, N., Murè, E. & Ansermet, J.-P. Microwave spin-torque excitation in a template-synthesized nanomagnet. *Physical Review B* **79**, 012404 (2009).
- [97] Kovalev, A. A., Bauer, G. E. W. & Brataas, A. Current-driven ferromagnetic resonance, mechanical torques, and rotary motion in magnetic nanostructures. *Physical Review B* **75**, 014430 (2007).
- [98] Staudacher, T. & Tsoi, M. Spin-torque-driven ferromagnetic resonance in point contacts. *Journal of Applied Physics* **109**, 07C912 (2011).
- [99] Hatami, M., Bauer, G. E. W., Zhang, Q. & Kelly, P. J. Thermal Spin-Transfer Torque in Magneto-electronic Devices. *Physical Review Letters* **99**, 066603 (2007).
- [100] Yuan, Z., Wang, S. & Xia, K. Thermal spin-transfer torques on magnetic domain walls. *Solid State Communications* **150**, 548–551 (2010).
- [101] Jia, X., Xia, K. & Bauer, G. E. W. Thermal Spin Transfer in Fe-MgO-Fe Tunnel Junctions. *Physical Review Letters* **107**, 176603 (2011).
- [102] Jansen, R., Deac, A., Saito, H. & Yuasa, S. Thermal spin current and magnetothermopower by Seebeck spin tunneling. *Phys. Rev. B* **85**, 94401 (2012).

Bibliography

- [103] Slonczewski, J. C. Initiation of spin-transfer torque by thermal transport from magnons. *Physical Review B* **82**, 054403 (2010).
- [104] Yu, H., Granville, S., Yu, D. P. & Ansermet, J.-P. Evidence for Thermal Spin-Transfer Torque. *Physical Review Letters* **104**, 146601 (2010).
- [105] Krause, S., Herzog, G., Schlenhoff, a., Sonntag, a. & Wiesendanger, R. Joule Heating and Spin-Transfer Torque Investigated on the Atomic Scale Using a Spin-Polarized Scanning Tunneling Microscope. *Physical Review Letters* **107**, 186601 (2011).
- [106] Schellekens, A. J., Kuiper, K. C., de Wit, R. & Koopmans, B. Ultrafast spin-transfer torque driven by femtosecond pulsed-laser excitation. *Nature Communications* **5**, 4333 (2014).
- [107] Choi, G.-M., Min, B.-C., Lee, K.-J. & Cahill, D. G. Spin current generated by thermally driven ultrafast demagnetization. *Nature communications* **5**, 4334 (2014).
- [108] Murè, E. *Current Induced Magnetization Dynamics in Electrodeposited Nanostructures*. Ph.D. thesis, EPFL (2010).
- [109] Murè, E., Bizière, N. & Ansermet, J.-P. Lithography-free study of spin torque. *Journal of Magnetism and Magnetic Materials* **322**, 1443–1445 (2010).
- [110] Gravier, L. *et al.* Thermopower measurement of single isolated metallic nanostructures. *Measurement Science and Technology* **15**, 420–424 (2004).
- [111] Hoffmann, M., von Geisau, O., Nikitov, S. & Pelzl, J. 3D-imaging of magnetostatic modes using photothermally modulated FMR-technique. *Journal of Magnetism and Magnetic Materials* **101**, 140–142 (1991).
- [112] Schreiber, F., Hoffmann, M., Geisau, O. & Pelzl, J. Investigation of the photothermally modulated ferromagnetic resonance signal from magnetostatic modes in yttrium iron garnet films. *Applied Physics A Solids and Surfaces* **57**, 545–551 (1993).
- [113] Kaack, M., Jun, S., Nikitov, S. A. & Pelzl, J. Magnetostatic spin wave modes excitation in yttrium-iron-garnet film under various temperatures. *Journal of Magnetism and Magnetic Materials* **204**, 90–100 (1999).
- [114] von Geisau, O., Rödelsperger, F., Schreiber, F., Benner, H. & Pelzl, J. Photothermally modulated spatially resolved FMR detection of Walker modes in yttrium iron garnet spheres. *Le Journal de Physique IV* **04**, C7–655–C7–658 (1994).
- [115] Meckenstock, R., Schreiber, F., von Geisau, O. & Pelzl, J. Photothermally modulated ferromagnetic resonance investigations of epitaxially grown thin films (abstract). *Journal of Applied Physics* **75**, 6508 (1994).
- [116] Meckenstock, R., von Geisau, O., Pelzl, J. & Wolf, J. A. Conventional and photothermally modulated ferromagnetic resonance investigations of anisotropy fields in an epitaxial Fe(001) film. *Journal of Applied Physics* **77**, 6439–6448 (1995).
- [117] de Julián Fernández, C. Influence of the temperature dependence of anisotropy on the magnetic behavior of nanoparticles. *Physical Review B* **72**, 054438 (2005).
- [118] McMichael, R. D. & Stiles, M. D. Magnetic normal modes of nanoelements. *Journal of Applied Physics* **97**, 10J901 (2005).
- [119] Blundell, S. *Magnetism in Condensed Matter* (OUP Oxford, 2001).
- [120] Cojocar, S., Naddeo, A. & Citro, R. Modification of the Bloch law in ferromagnetic nanostructures. *EPL (Europhysics Letters)* **106**, 17001 (2014).

- [121] Gravier, L., Serrano-Guisan, S., Reuse, F. & Ansermet, J. P. Spin-dependent Peltier effect of perpendicular currents in multilayered nanowires. *Physical Review B - Condensed Matter and Materials Physics* **73**, 52410 (2006).
- [122] Fitoussi, L. *et al.* Linear response to a heat-driven spin torque. *Applied Physics Letters* **106**, 162401 (2015).
- [123] Serrano Guisan, S. *Spin dependent thermoelectric effects in magnetic nanostructures*. Ph.D. thesis, EPFL (2006).
- [124] Gravier, L., Serrano-Guisan, S., Reuse, F. & Ansermet, J.-P. Thermodynamic description of heat and spin transport in magnetic nanostructures. *Physical Review B* **73**, 24419 (2006).
- [125] Serrano-Guisan, S., Gravier, L. & Ansermet, J. P. Evidence of high dissipation in magnetization reversal processes of five Co/Cu bilayers. *Materials Science and Engineering B: Solid-State Materials for Advanced Technology* **126**, 292–295 (2006).
- [126] Yu, H., Granville, S., Yu, D. P. & Ansermet, J.-P. Heat and spin transport in magnetic nanowires. *Solid State Communications* **150**, 485–488 (2010).
- [127] Yu, H., Dubois, J., Granville, S., Yu, D. P. & Ansermet, J.-P. Current susceptibility of magnetization in spin valves. *Journal of Physics D: Applied Physics* **42**, 175004 (2009).
- [128] Balaz, P., Barnas, J. & Ansermet, J.-P. Transverse spin penetration length in metallic spin valves. *Journal of Applied Physics* **113**, 193905 (2013).

List of abbreviations

BLS	Brillouin Light Scattering
BVMSW	Backward Volume Magnetostatic Spin Wave
CW	Continuous Wave
FM	Ferromagnetic/Ferromagnet
FMR	Ferromagnetic resonance
FVMSW	Forward Volume Magnetostatic Spin Wave
GMR	Giant Magnetoresistance
ISHE	Inverse Spin Hall Effect
MSE	Magnetic Seebeck Effect
MSSW	Magnetostatic Surface Spin Wave
NM	Normal Metal
PCB	Printed Circuit Board
PM-FMR	Photothermally Modulated Ferromagnetic Resonance
RF	Radio Frequency
SMD	Surface Mounted Device
SSE	Spin Seebeck Effect
STT	Spin Transfer Torque
TST	Thermal Spin Torque
YIG	Yttrium Iron Garnet

Francesco Antonio Vetrò

PERSONAL INFORMATION *E-mail:* antonio.vetro@gmail.com
Citizenship: Italian
Date of birth 17th June 1986

PROFESSIONAL EXPERIENCE

January 2010 to July 2015

PhD candidate/Teaching assistant - Institute of Condensed Matter Physics, École Polytechnique Fédérale de Lausanne, Lausanne, Switzerland.

March 2010 to August 2010

Research Intern - T. J. Watson IBM Research Center, Yorktown Heights, NY, USA.

Master Thesis Project: *In-plane uniaxial magnetic anisotropy induced by textured underlayer, for Spin Transfer Torque MRAM*

June 2009 to August 2009

Research Intern - FORTH - Foundation for Research & Technology
IELS - Institute of Electronic Structure & Laser , Heraklion, Greece

Research project: *SiC based Zener diode for automotive applications*

EDUCATION

January 2010 to July 2015

PhD studies in Physics

Institute of Condensed Matter Physics, École Polytechnique Fédérale de Lausanne, Lausanne, Switzerland.

September 2008 to September 2010

Master in Micro and Nanotechnologies for Integrated Systems

Politecnico di Torino, INPG, EPFL

Sep 2009 - Jan 2010 École Polytechnique Fédérale de Lausanne, Switzerland

Feb 2009 - Jun 2009 Institut National Polytechnique de Grenoble, France

Sep 2008 - Jan 2009 Politecnico di Torino, Italy

September 2005 to December 2008

Bachelor in Electronic Engineering

Politecnico di Torino, Italy

September 2000 to July 2005

Scientific Certificate Secondary School Diploma

Liceo Scientifico N.Machiavelli, Soriano Calabro, Italy

PUBLICATIONS/PATENT

Brechet, S. D., Vetro, F. A., Papa, E., Barnes, S. E., & Ansermet, J.-P. (2013). Evidence for a Magnetic Seebeck Effect. *Physical Review Letters*, *111*(8), 87205.

Fitoussi, L., Vetro, F. A., Caspers, C., Gravier, L., Yu, H., & Ansermet, J.-P. (2015). Linear response to a heat-driven spin torque. *Applied Physics Letters*, *106*(16), 162401.

Vetro, F. A., & Worledge, D. C. . Magnetic tunnel junction devices having magnetic layers formed on composite, obliquely deposited seed layers. *Patent US20130119495 A1* (2014)

CONFERENCES/WORKSHOPS

APS March meeting 2015, March 2015, San Antonio, TX, USA.
Oral presentation.

Physics of magnetism 2014 (PM'14), June 2014, Poznan, Poland.
Poster presentation.

Joint European Magnetic Symposia (JEMS), Rhodes, Greece, August 2013.
Poster presentation.

2nd SpinCaT PhD workshop, October 2012, Gottingen, Germany.
Poster presentation.

European Magnetic Symposia (JEMS), September 2012, Parma, Italy. *Poster presentation.*

1st SpinCaT PhD workshop, April 2012, Regensburg, Germany.
Poster presentation.